





**INVESTIGATION OF STRESS DISTRIBUTIONS  
BETWEEN A FRICTIONAL RIGID CYLINDER AND  
LAMINATED GLASS FIBER COMPOSITES**

**SÜRTÜNMELİ RİJİT SİLİNDİR İLE LAMİNE CAM ELYAF  
KOMPOZİTLER ARASINDAKİ GERİLİM  
DAĞILIMLARININ İNCELENMESİ**

**KORHAN BABACAN YILMAZ**

**PROF. DR BORA YILDIRIM**

**Supervisor**

Submitted to Graduate School of Science and Engineering of Hacettepe  
University

as a Partial Fulfilment to the Requirements

for the Award of the Degree of Doctor of Philosophy

in Mechanical Engineering

2021







# **ABSTRACT**

## **INVESTIGATION OF STRESS DISTRIBUTIONS BETWEEN A FRICTIONAL RIGID CYLINDER AND LAMINATED GLASS FIBER COMPOSITES**

**Korhan Babacan YILMAZ**

**Doctor of Philosophy, Department of Mechanical Engineering**

**Supervisor: Prof. Dr. Bora Yildirim**

**Co – Supervisor: Assoc. Prof. Dr. Baris Sabuncuoglu**

**April 2021, 116 pages**

Surface and sub – surface stresses, and edges of contact patch between a rigid cylinder and laminated glass fiber composites are evaluated in this thesis. A novel and modern system of analysis based on Cholesky decomposition, Gauss elimination, Hermite orthogonal polynomials, Fourier transforms and singular integral equation (SIE) is developed to obtain analytical results. Numerical results are obtained in order to verify the precision of the analytical method using an effective and self mesh adaptive computational model built on augmented contact formulation (ACF) and finite element method. The effectiveness of the new analytical formulation was shown by a perfect match between these results. The formulations have been introduced for various interaction properties, material parameters, friction related terms, and lamina order in order to monitor the effects on surface and sub – surface stresses, and edges of contact patch. The findings and discussions addressed can be of value to the structural design of laminated glass fiber composites under extreme contact conditions.

**Keywords:** Laminated glass fiber composites, Augmented contact formulation (ACF), Singular integral equation (SIE), Frictional sliding contact, Cholesky decomposition, Tribology

## ÖZET

### SÜRTÜNME Lİ RİJİT SİLİNDİR İLE LAMİNE CAM ELYAF KOMPOZİTLER ARASINDAKİ STRES DAĞILIMLARININ İNCELENMESİ

**Korhan Babacan YILMAZ**

**Doktora, Makina Mühendisliği Bölümü**

**Tez Danışmanı: Prof. Dr. Bora Yıldırım**

**Eş – Danışman: Doç. Dr. Barış Sabuncuoğlu**

**Nisan 2021, 116 sayfa**

Bu tez çalışmasında, rijit bir silindir ile lamine glass fiber kompozitler arasındaki yüzey ve yüzey – altı gerilmeleri ve temas patikasının kenarları değerlendirilmiştir. Analitik sonuçlar elde etmek için Cholesky ayrışımı, Gauss eliminasyonu, Hermite ortogonal polinomları, Fourier dönüşümleri, ve tekil integral denkleminde (TID) dayanan yeni ve modern bir analiz sistemi geliştirilmiştir. Analitik yöntemin hassasiyetini doğrulamak için, artırılmış temas formülasyonu (ATF) ve sonlu elemanlar yöntemi üzerine inşa edilmiş efektif ve kendi kendine ağ uyarlamalı bir hesaplama modeli kullanarak sayısal sonuçlar elde edilmiştir. Yeni analitik formülasyonun etkinliği, bu sonuçlar arasında mükemmel bir eşleşme ile gösterilmiştir. Formülasyonlar, yüzey ve yüzey – altı gerilmeleri ve temas patikasının kenarları üzerindeki etkileri izlemek için çeşitli etkileşim özellikleri, malzeme parametreleri, sürtünmeyle ilgili terimler ve lamina sırası için tanıtılmıştır. Ele alınan bulgular ve tartışmalar, aşırı temas koşulları altında lamine kompozitlerin yapısal tasarımı için değerli olacaktır.

**Anahtar Kelimeler:** Lamine cam elyaf kompozitler, Artırılmış temas formülasyonu (ATF), Tekil integral denklem (TID), Sürtünmeli kayan temas, Cholesky ayrışımı, Triboloji



## **ACKNOWLEDGEMENTS**

I am fortunate to acknowledge the roles of several individuals who have been influential in completing my Ph. D. research. I would like to express my deepest appreciation, firstly to, my co – supervisor Dr. Baris Sabuncuoglu for his serious interest on me at every point of my studies. I was able to complete this work with his motivations, timely recommendations with kindness and dedication.

This work would not have been completed without the assistance and mentorship of Dr. Isa Comez, who contributed to the many discussions. It was a privilege for me to be collaborating with him. His sincerity, commitment, and inspiration have greatly motivated me to carry out this research.

Such acknowledgements would not be achieved without the assistance of Dr. Mehmet Ali Guler, who has supported and advised me throughout my graduate studies. His productive and enduring attitude has given countless intellectual rewards to his mentees.

I would also like to thank my fellow Ph. D. (c) colleagues Gorkem Celik and Tanilay Ozdemir, and Ph. D. Rasit Karakus, for providing a pleasant working environment in the department. Their motivation and encouragement have always motivated me to fulfill my obligations in my academic career.

Lastly, and most of all, my greatest gratitude belongs to Dr. Bora Yildirim, who inspired me to pursue this study and instructed me the art of finite element methodology and numerical contact modelling. In a research atmosphere, that stimulates the original ideas and initiative he developed, I genuinely liked working. The encouragement, creativity and patience of him will always be remembered and respected.

# TABLE OF CONTENTS

ABSTRACT .....	i
ÖZET .....	ii
ACKNOWLEDGEMENTS.....	iii
TABLE OF CONTENTS .....	iv
LIST OF FIGURES .....	vii
LIST OF TABLES .....	x
SYMBOLS AND ABBREVIATIONS.....	xii
1. INTRODUCTION .....	1
1.1. Background.....	1
1.1.1.Contact conditions.....	2
1.1.2.Material types and material models.....	5
1.2. Literature review on contact mechanics regarding analytical methods ....	6
1.3. Aim and scope .....	10
1.4. Problem definition .....	11
2. ANALYTICAL METHOD.....	13
2.1. Calculations for the material parameters for a single composite lamina	13
2.2. Calculation of transformed rotated stiffness constants for a single composite lamina .....	15
2.3. Derivation of displacement equations and stress – displacement relations for a single composite lamina.....	17
2.4. Derivation of stress components and $k_j$ , $m_j$ , and $n_j$ expressions for a single composite lamina.....	19
2.5. Boundary conditions and singular integral equation (SIE) for a single composite lamina .....	23
2.6. Solution of singular integral equation (SIE) and calculation of contact stress at the surface for a single composite lamina .....	28

2.7. Calculation of in – plane stress at the surface for a single composite lamina .....	31
2.8. Calculation of in – plane stress at sub – surface for a single composite lamina .....	32
2.9. Transition of equations from a single composite lamina to laminated glass fiber composite .....	32
2.9.1. Material parameters.....	32
2.9.2. Transformed rotated stiffness constants.....	33
2.9.3. Displacement equations and stress – displacement relations .....	34
2.9.4. Stress components and $k_j$ , $m_j$ , and $n_j$ expressions.....	35
2.9.5. Boundary conditions and singular integral equation (SIE) .....	37
2.9.6 Solution of singular integral equation (SIE) and calculation of contact stress at the surface .....	43
2.9.7 Calculation of in – plane stress at the surface .....	43
2.9.8 Calculation of in – plane stress at the sub – surface .....	43
3. FINITE ELEMENT METHOD .....	45
3.1. Literature review on contact mechanics and computational advances regarding finite element method, layered structures, and laminated composites .....	45
3.2. Advantages of finite element method .....	47
3.3. Modeling of laminated glass fiber composite .....	47
3.3.1. Finite element types.....	47
3.3.2. Augmented contact formulation (ACF).....	50
3.3.3. Preperation of the model, adaptive mesh refinement, and solution details .....	51
3.3.4. Accuracy of adaptive mesh refinement and solution times .....	52
4. RESULTS AND DISCUSSION.....	55
4.1. Effects of interaction properties, material parameters, and friction related terms on surface contact and in – plane stress distributions .....	55
4.2. Effects of lamina order on surface contact and in – plane stress and sub – surface center – line in – plane stress distributions .....	64
4.3. Comparison of sub – surface in – plane stress contours .....	79

5. CONCLUSIONS .....	83
6. REFERENCES .....	85
APPENDIX .....	91
APPENDIX 1 – Curve fit plots for $1/\psi_1(M_1 - \psi_1)$ and $1/\psi_1(M_1 - \psi_2)$ for $[90_3/0_3]_s$ configuration.....	91
APPENDIX 2 – Publications derived from thesis .....	92
APPENDIX 3 – Thesis originality report.....	112
CURRICULUM VITAE .....	113

## LIST OF FIGURES

Fig. 1. 2 – D graphical representation of a simple sliding contact problem .....	2
Fig. 2. 2 – D graphical representation of a simple receding contact problem .....	3
Fig. 3. 2 – D graphical representation of a simple partial slip contact problem...	3
Fig. 4. 2 – D graphical representation of a simple rolling contact problem .....	4
Fig. 5. 2 – D graphical representation of a simple thermo – mechanical contact problem.....	4
Fig. 6. Geometry of a single composite lamina .....	11
Fig. 7. Geometry of a glass fiber laminated composite .....	12
Fig. 8. Element geometries and stress output of <i>PLANE183</i> finite element .....	48
Fig. 9. Element geometries of <i>TARGE169</i> target segment elements.....	49
Fig. 10. Segment element types of <i>TARGE169</i> target segment elements .....	49
Fig. 11. Element geometry of <i>CONTA172</i> contact line element.....	50
Fig. 12. Finite element model and deformed shape of glass fiber laminated composite.....	52
Fig. 13. Iterative scheme.....	52
Fig. 14. Comparison of surface contact and in – plane stress distribution for $R = 100mm$ , $\eta = 0.4$ , $V_f = \%40$ , $h_t = 4.5mm$ , $h = 0.375mm$ , $W = 90mm$ , $m = 12$ , solid lines represent finite element method, dotted lines represent analytical method.....	56
Fig. 15. Comparison of surface contact and in – plane stress distribution for $R = 100mm$ , $P = 100N/mm$ , $V_f = \%40$ , $h_t = 4.5mm$ , $h = 0.375mm$ , $W = 90mm$ , $m = 12$ , solid lines represent finite element method, dotted lines represent analytical method.....	58
Fig. 16. Comparison of surface contact and in – plane stress distribution for $\eta = 0.4$ , $P = 100N/mm$ , $V_f = \%40$ , $h_t = 4.5mm$ , $h = 0.375mm$ , $W = 90mm$ , $m = 12$ , solid lines represent finite element method, dotted lines represent analytical method.....	61
Fig. 17. Comparison of surface contact and in – plane stress distribution for $\eta = 0.4$ , $P = 100N/mm$ , $R = 100mm$ , $h_t = 4.5mm$ , $h = 0.375mm$ , $W = 90mm$ ,	

$m=12$ , solid lines represent finite element method, dotted lines represent analytical method .....	63
Fig. 18. Comparison of surface contact and in – plane stress distribution for $R=100mm$ , $\eta=0.4$ , $V_f = \%40$ , $h_t = 4.5mm$ , $h=0.375mm$ , $W=90mm$ , $m=12$ , solid lines represent finite element method, dotted lines represent analytical method .....	66
Fig. 19. Comparison of surface contact and in – plane stress distribution for $R=100mm$ , $P=100N/mm$ , $V_f = \%40$ , $h_t = 4.5mm$ , $h=0.375mm$ , $W=90mm$ , $m=12$ , solid lines represent finite element method, dotted lines represent analytical method .....	68
Fig. 20. Comparison of surface contact and in – plane stress distribution for $\eta=0.4$ , $P=100N/mm$ , $V_f = \%40$ , $h_t = 4.5mm$ , $h=0.375mm$ , $W=90mm$ , $m=12$ , solid lines represent finite element method, dotted lines represent analytical method .....	69
Fig. 21. Comparison of surface contact and in – plane stress distribution for $\eta=0.4$ , $P=100N/mm$ , $R=100mm$ , $h_t = 4.5mm$ , $h=0.375mm$ , $W=90mm$ , $m=12$ , solid lines represent finite element method, dotted lines represent analytical method .....	71
Fig. 22. Comparison of surface contact and in – plane stress distribution for $R=100mm$ , $\eta=0.4$ , $V_f = \%40$ , $h_t = 4.5mm$ , $h=0.375mm$ , $W=90mm$ , $m=12$ , solid lines represent finite element method, dotted lines represent analytical method .....	72
Fig. 23. Comparison of surface contact and in – plane stress distribution for $R=100mm$ , $P=100N/mm$ , $V_f = \%40$ , $h_t = 4.5mm$ , $h=0.375mm$ , $W=90mm$ , $m=12$ , solid lines represent finite element method, dotted lines represent analytical method .....	74
Fig. 24. Comparison of surface contact and in – plane stress distribution for $\eta=0.4$ , $P=100N/mm$ , $V_f = \%40$ , $h_t = 4.5mm$ , $h=0.375mm$ , $W=90mm$ , $m=12$ , solid lines represent finite element method, dotted lines represent analytical method .....	75

Fig. 25. Comparison of surface contact and in – plane stress distribution for $\eta = 0.4$ , $P = 100N/mm$ , $R = 100mm$ , $h_t = 4.5mm$ , $h = 0.375mm$ , $W = 90mm$ , $m = 12$ , solid lines represent finite element method, dotted lines represent analytical method .....	77
Fig. 26. Comparison of surface contact and in – plane stress distribution for $\eta = 0.4$ , $P = 100N/mm$ , $R = 100mm$ , $V_f = \%40$ , $h_t = 4.5mm$ , $h = 0.375mm$ , $W = 90mm$ , $m = 12$ , solid lines represent finite element method, dotted lines represent analytical method .....	78
Fig. 27. Comparison of sub – surface center – line in – plane stress distributions for $\eta = 0.4$ , $R = 100mm$ , $V_f = \%40$ , $h_t = 4.5mm$ , $h = 0.375mm$ , $W = 90mm$ , $m = 12$ , solid lines represent finite element method, dotted lines represent analytical method .....	79
Fig. 28. Comparison of sub – surface in – plane stress contours for $\eta = 0.4$ , $P = 100N/mm$ , $R = 100mm$ , $V_f = \%40$ , $h_t = 4.5mm$ , $h = 0.375mm$ , $W = 90mm$ , $m = 12$ .....	80
Fig. 29. Comparison of sub – surface in – plane stress contours for $\eta = 0.4$ , $P = 100N/mm$ , $R = 100mm$ , $V_f = \%40$ , $h_t = 4.5mm$ , $h = 0.375mm$ , $W = 90mm$ , $m = 12$ .....	81

## LIST OF TABLES

Table 1. Material parameters for individual glass fiber and epoxy matrix .....	12
Table 2. Accuracy of adaptive mesh refinement – 1 .....	53
Table 3. Accuracy of adaptive mesh refinement – 2 .....	54
Table 4. Accuracy of adaptive mesh refinement – 3 .....	54
Table 5. Edges of contact patch for unidirectional configuration $[0_{12}]$ for varying $P$ .....	57
Table 6. Edges of contact patch for unidirectional configuration $[90_{12}]$ for varying $P$ .....	58
Table 7. Edges of contact patch for unidirectional configuration $[0_{12}]$ for varying $\eta$ .....	59
Table 8. Edges of contact patch for unidirectional configuration $[90_{12}]$ for varying $\eta$ .....	59
Table 9. Edges of contact patch for unidirectional configuration $[0_{12}]$ for varying $R$ .....	62
Table 10. Edges of contact patch for unidirectional configuration $[90_{12}]$ for varying $R$ .....	62
Table 11. Edges of contact patch for unidirectional configuration $[90_{12}]$ for varying $V_f$ .....	63
Table 12. Edges of contact patch for unidirectional configuration $[90_{12}]$ for varying $V_f$ .....	64
Table 13. Edges of contact patch for configuration $[0_3/90_3]_s$ for varying $P$ .....	67
Table 14. Edges of contact patch for configuration $[90_3/0_3]_s$ for varying $P$ .....	67
Table 15. Edges of contact patch for configuration $[0_3/90_3]_s$ for varying $\eta$ .....	68
Table 16. Edges of contact patch for configuration $[90_3/0_3]_s$ for varying $\eta$ .....	69
Table 17. Edges of contact patch for configuration $[0_3/90_3]_s$ for varying $R$ .....	70
Table 18. Edges of contact patch for configuration $[90_3/0_3]_s$ for varying $R$ .....	70



Table 19. Edges of contact patch for configuration $[0_3 / 90_3]_s$ for varying $V_f$ ...	71
Table 20. Edges of contact patch for configuration $[90_3 / 0_3]_s$ for varying $V_f$ ...	72
Table 21. Edges of contact patch for configuration $[0_3 / 90_3]_2$ for varying $P$ .....	73
Table 22. Edges of contact patch for configuration $[90_3 / 0_3]_2$ for varying $P$ .....	73
Table 23. Edges of contact patch for configuration $[0_3 / 90_3]_2$ for varying $\eta$ .....	74
Table 24. Edges of contact patch for configuration $[90_3 / 0_3]_2$ for varying $\eta$ .....	75
Table 25. Edges of contact patch for configuration $[0_3 / 90_3]_2$ for varying $R$ .....	76
Table 26. Edges of contact patch for configuration $[90_3 / 0_3]_2$ for varying $R$ .....	76
Table 27. Edges of contact patch for configuration $[0_3 / 90_3]_2$ for varying $V_f$ ...	77
Table 28. Edges of contact patch for configuration $[90_3 / 0_3]_2$ for varying $V_f$ ...	78

## SYMBOLS AND ABBREVIATIONS

### Symbols

$h_t$	Total thickness
$W$	Total width
$h$	Lamina thickness
$P$	Concentrated normal force
$Q = \eta P$	Concentrated horizontal force
$\eta$	Coefficient of friction
$E_f$	Elastic modulus of glass fiber
$V_f$	Volume fraction of glass fiber
$E_m$	Elastic modulus of epoxy matrix
$V_m$	Volume fraction of epoxy matrix
$\mu_f$	Shear modulus of glass fiber
$\nu_f$	Poisson's ratio of glass fiber
$\mu_m$	Shear modulus of epoxy matrix
$\nu_m$	Poisson's ratio of epoxy matrix
$E_{ii}$	Elastic modulus tensor
$\mu_{ij}$	Shear modulus tensor
$\nu_{xy}$	Poisson's ratio tensor
$\sigma_{ij}$	Stress tensor ( $-x$ , $-y$ , and $-z$ global and $-1$ , $-2$ , and $-3$ local directions)
$\varepsilon_{ij}$	Strain tensor ( $-x$ , $-y$ , and $-z$ global and $-1$ , $-2$ , and $-3$ local directions)

$C_{ij}$	Stiffness constants tensor ( $-x$ , $-y$ , and $-z$ global directions)
$\Delta$	Delta
$Q_{ij}$	Rotation matrix tensor
$rt_i$	Counterclockwise rotation cosines and sines tensor
$\theta$	Configuration angle
$\overline{C}_{ij}$	Transformed rotated stiffness constants tensor ( $-1$ , $-2$ , and $-3$ local directions)
$T_1$	Transformation matrix
$T_2$	Transformation matrix
$\xi$	Equation variable
$I$	Imaginary unit
$k_j$	Numerical constants tensor for a single composite lamina
$m_j$	Numerical constants tensor for a single composite lamina
$n_j$	Numerical constants tensor for a single composite lamina
$A_j$	Symbolic constants tensor for a single composite lamina
$p(x)$	Surface contact stress
$q(x)$	Surface in – plane stress
$\delta$	Penetration depth
$f(x)$	Profile function
$R$	Radius
$A_j^p$	Symbolic sub – constants for a single composite lamina
$A_j^q$	Symbolic sub – constants for a single composite lamina

$-a$	Edge of contact patch
$b$	Edge of contact patch
$M_1$	Symbolic or numerical integral sub – constant
$N_1$	Symbolic or numerical integral sub – constant
$\psi_1$	Symbolic or numerical integral sub – constant
$\psi_2$	Symbolic or numerical integral sub – constant
$t$	Normalization term
$x$	Normalization term
$r_i$	Roots of Jacobi polynomial
$s_k$	Roots of Jacobi polynomial
$\chi$	Index of singular integral equation (SIE)
$W_i^N$	Weighting constant
$N$	Iteration limit constant
$M_2$	Symbolic or numerical integral sub – constant
$N_2$	Symbolic or numerical integral sub – constant
$\psi_3$	Symbolic or numerical integral sub – constant
$\psi_4$	Symbolic or numerical integral sub – constant
$\sigma_{m,ij}$	Stress tensor ( $-x$ , $-y$ , and $-z$ global and $-1$ , $-2$ , and $-3$ local directions) for laminated glass fiber composites
$\varepsilon_{m,ij}$	Strain tensor ( $-x$ , $-y$ , and $-z$ global and $-1$ , $-2$ , and $-3$ local directions) for laminated glass fiber composites
$m$	Number of lamina
$C_{m,ij}$	Stiffness constants tensor ( $-x$ , $-y$ , and $-z$ global directions) for laminated glass fiber composites

$Q_{m,ij}$	Rotation matrix tensor for laminated glass fiber composites
$rt_{m,i}$	Counterclockwise rotation cosines and sines tensor for laminated glass fiber composites
$\theta_m$	Configuration angle for laminated glass fiber composites
$\overline{C_{m,ij}}$	Transformed rotated stiffness constants tensor ( $-1$ , $-2$ , and $-3$ local directions) for laminated glass fiber composites
$T_{m,1}$	Transformation matrix for laminated glass fiber composites
$T_{m,2}$	Transformation matrix for laminated glass fiber composites
$k_{m,j}$	Numerical constants tensor for laminated glass fiber composites
$m_{m,j}$	Numerical constants tensor for laminated glass fiber composites
$n_{m,j}$	Numerical constants tensor for laminated glass fiber composites
$A_{m,j}$	Numerical constants tensor for laminated glass fiber composites

### **Abbreviations**

SIE	Singular integral equation
ACF	Augmented contact formulation



# 1. INTRODUCTION

## 1.1. Background

Tribology and understanding the tribological behavior of products are very important in “Material Science” and “Engineering Mechanics” thematic fields, and “Surface, Coating, and Film” subfield. The tribology is the investigation science of interacting surfaces that are in motion with each other. The locution “Tribology” was first appeared in a technical report, where its scope was defined as research and evaluation of friction, lubrication, and wear mechanisms in products and real life engineering applications [1]. In general, tribological community provides benchmarks to industry using various types of conventional and unconventional materials to improve characteristics of interacting surfaces that are in continuous motion. These benchmarks are closely related to “Contact mechanics” thematic field and “Surface, Coating, and Film” subfield. In virtue of technological advances, research on tribology are greatly increased because almost all of the products used in engineering applications required to be design more effectively and accurately to prevent the unnecessary material loss happening from high wear, high surface friction and inadequate lubrication characteristics.

A native contact mechanics problem consists of minimum two perpetual in motion elastic or one elastic and one rigid surface (means very stiff compared to other surface). As mentioned before, general purpose of these type of problems is to provide highly qualified and efficient benchmarks to be used in mechanical, thermal and/or dynamic design stages of engineering applications involving both conventional and unconventional materials. Among the literature, first study that investigated the mechanical behavior of these type of surfaces was carried out by considering a contact problem between two smooth curved elastic surfaces in which the contact was assumed to be frictionless [2]. After this study, many comprehensive studies were built and presented to the open literature. Reader can refer to spacious survey presented by [3] for further information on contact mechanics problems.

### 1.1.1. Contact conditions

In engineering applications for the transfer of loads, moments or displacements between products in assemblies, several types of contact conditions may be used with regard to the field of usage. The most common ones used in industrial applications are explained briefly below.

The sliding contact is a very specific type of contact condition and is very important in appropriately determining wear, fatigue, and friction components in engineering applications as it allows tangential displacement to contact patch without a relative motion along the normal direction. In general, sliding contacts can be used to model the sliding movement of the surfaces in assemblies under Coulomb's law of static friction. A 2 – D graphical representation of a simple sliding contact problem is presented in Fig. 1, where a rigid cylindrical punch transmits both normal and tangential loads to the finite thick elastic layer.

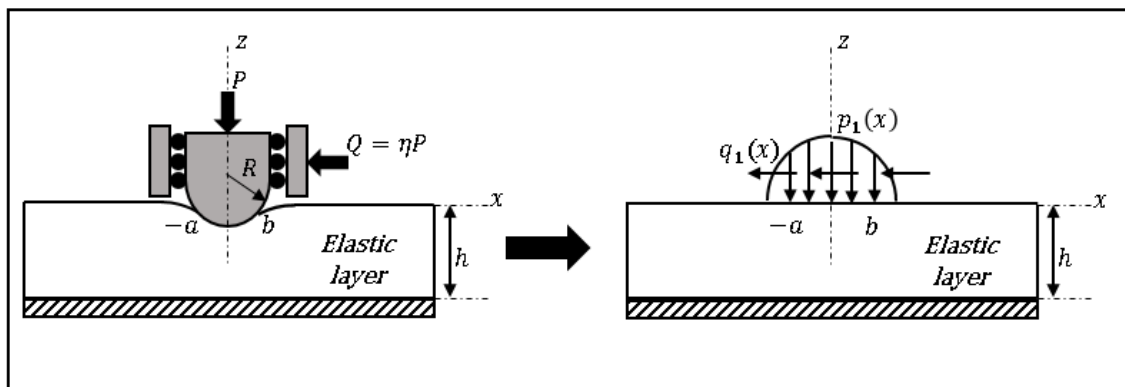


Fig. 1. 2 – D graphical representation of a simple sliding contact problem

The receding contact is an extension of sliding contact condition and its application is considerably more difficult as contact patch between the elastic layers' shrinks or expands when the load is applied or decreased, respectively. Therefore, proper investigation of wear and fatigue components not only at the surface but also at the interface is crucial in determining the contact performance. In Fig. 2, a 2 – D graphical representation of a simple receding contact problem is presented by considering a rigid cylindrical punch and two finite thick elastic layers.

In partial slip contact condition, the contact stress generates a tangential displacement at the interface because of the dissimilarity at the lower and upper contact interfaces; slip or partial slip may generally take place and this result in



two distinct contact boundaries on same surface. Monitoring these slip regions is essential in successfully determining the wear components. Yet, these regions can be prevented by applying a little bit more friction at the contact patches. The slip zones are presented in Fig. 3 between  $-a, -b$  and  $a, b$ .

Rolling contact is one of the most important contact types used in engineering applications. In this type of contact, the rolling motion of one body over another body can cause fatigue and surface wear due to the repetitive stresses at the contact region happening from stick and slip zones [4] (see Fig. 4). These type of contact could be seen in anti – friction bearings, train wheel assemblies and crankshaft housings for engines.

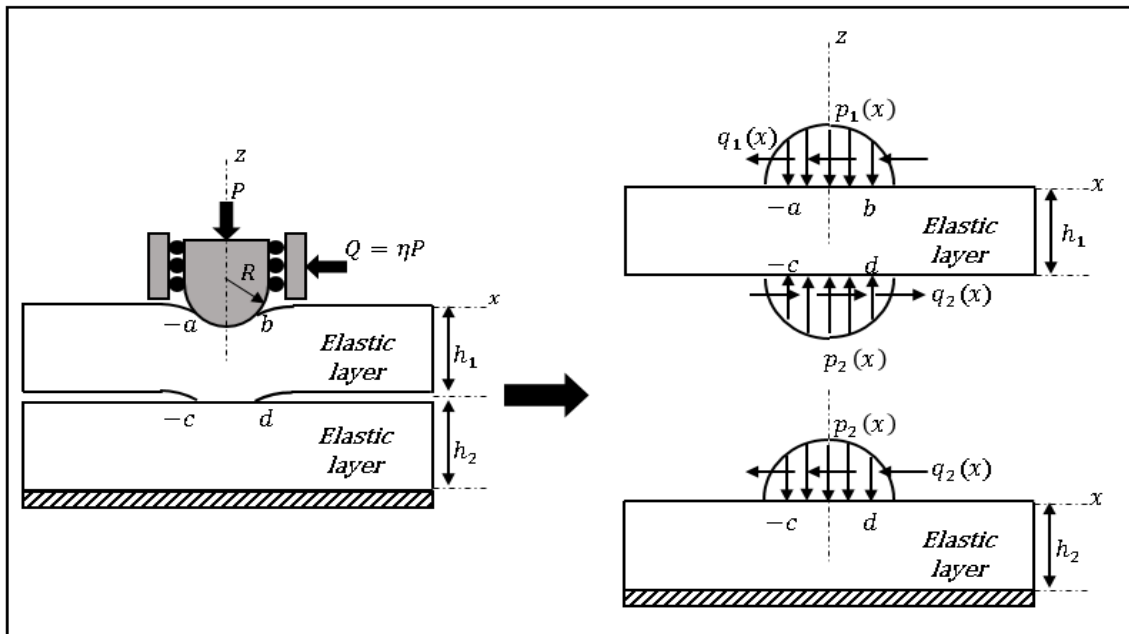


Fig. 2. 2 – D graphical representation of a simple receding contact problem

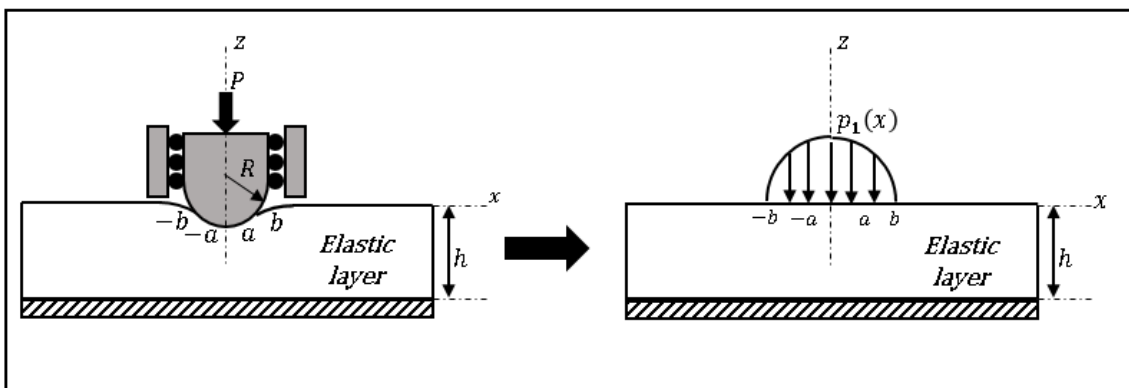


Fig. 3. 2 – D graphical representation of a simple partial slip contact problem

In general, the deformation and temperature fields play the most important role in thermo – mechanical contact problems. Since the constitutive relations are dependent on temperature, these fields are coupled. In this type of contact, frictional forces or deformation mechanisms usually generate heat. Application of thermo – mechanical contact problems has a wide range including shrink fit problems, temperature loading and frictional heating, metal forming processes, and cooling of electronic and mechanical devices [5]. A very simple model for a thermo – mechanical contact problem is depicted in Fig. 5 with a constant heat transfer coefficient between the surfaces.

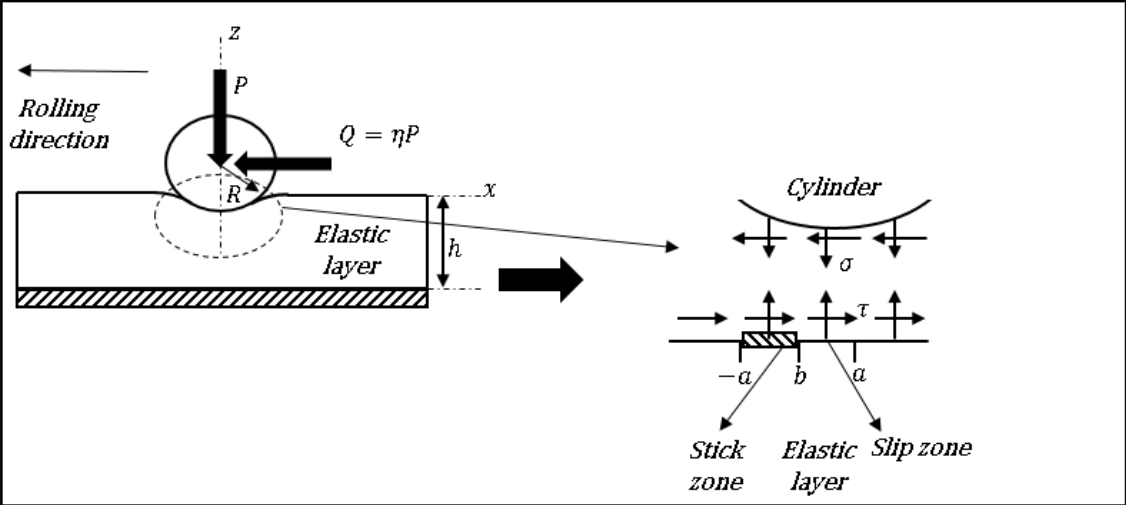


Fig. 4. 2 – D graphical representation of a simple rolling contact problem

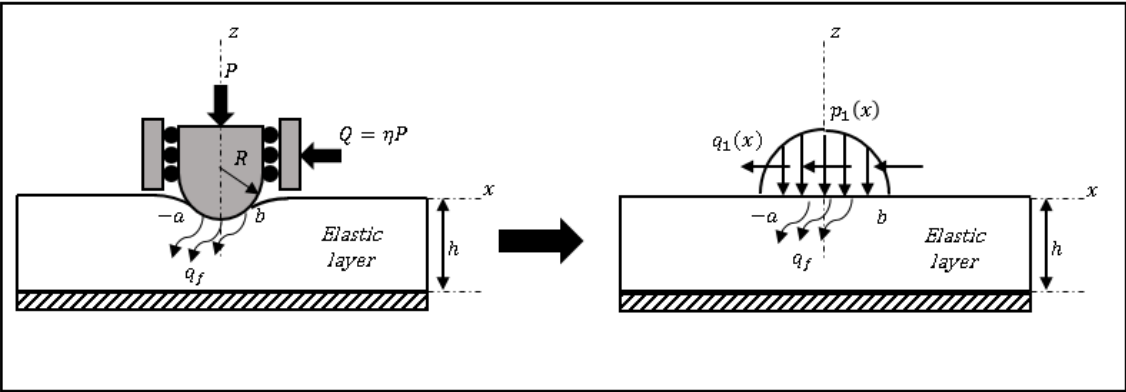


Fig. 5. 2 – D graphical representation of a simple thermo – mechanical contact problem

### 1.1.2. Material types and material models

There are different types of materials used in contact mechanics applications regarding their physical and mechanical properties. These materials can either be manufactured or be found in nature in homogeneous/unhomogeneous and/or isotropic/anisotropic (conventional/unconventional) forms. A material with a uniform composition throughout its body can be considered as homogeneous, where certain types of plastics, ceramics, glass, and metals are the common examples for homogeneous materials. Conversely, unhomogeneous materials have a non – uniform physical properties along their bodies. In engineering applications, they can be manufactured using step – by – step or continuous gradation methods [6 – 8]. Turbine blade coatings, bullet – proof vests, armored planes, bonded laminates, dental implants, and thermal – barrier coatings, wear resistant surfaces, and concrete can be common examples for these type of materials [9 – 14].

In material isotropy, mechanical and thermal properties show similarity in all three principal directions. Due to this resemblance, applied tensile loading only causes elongation in that principal direction and two other principal directions produce zero shear strain. If one of the principal directions is normal to the plane of isotropy (for instance,  $-x$  global direction is normal to  $-yz$  plane), then the material can be called as transversely isotropic. Transversely isotropic materials are a type of anisotropic materials, where the unidirectional composites are the most common example. Furthermore, if a material has three distinct but mutually perpendicular planes of symmetry, then it exhibits an orthotropic behavior. Due to this discrepancy between the planes, the thermal and mechanical properties differ in all three principal directions, where wood and continuous fibers with single lamina orientation can be the examples for orthotropic materials. Moreover, if a material has single plane of symmetry, then it can be named as monoclinic material. Rotated fibers and multilayered composites are most common examples for monoclinic materials.

## **1.2. Literature review on contact mechanics regarding analytical methods**

The solution of contact mechanics problems regarding isotropic materials were well established in literature. Assuming a classical uncoupled tangential contact problem between two elastic and linear spheres under constant normal loading, positions of stick and slip regions on contact patch were illustrated. It was shown that stick region appears at inner domain while slip region emerges at the edges of the contact patch [15]. Some comprehensive contact problems about two dimensional stress systems, infinite elastic solids, basic equations of 2 – D theory of elasticity and solution of stress functions were presented in [16 – 17]. An indentation problem for an elastic half – plane and an axisymmetric punch was studied under frictional contact conditions. It was found that, progressive increase of normal force affected maximum indentation and dimensionless normal displacement on contact patch [18].

Solution of contact problems involving material anisotropy and transversely isotropy is quite difficult than the ones with isotropic materials. In these solutions, extra – added linked and unlinked stiffness constants bring complexity to solution of mathematical equations. Using tangential and normal loading conditions, stress fields generated by sliding contact on transversely isotropic spheres were investigated [19]. It was concluded that Hankel transforms were quite capable in evaluation of integrals for surface stresses. Closed – form solutions for surface tractions and stresses were presented using sliding friction for transverse isotropy; shown that Green's functions could be used to solve contact problems and field equations [20]. Later, a three dimensional sliding contact problem between a layered half – plane and a spherical indenter was considered and stress fields related to failure and cracks were presented [21]. It was shown that, material type and membrane thickness greatly affected the structural behavior of coated surface and stiffness. Different types of interfacial contacts were investigated by loading a transversely isotropic layer with a rigid spherical indenter. Presented results from approximate solutions brought a good agreement with the previous results from literature [22]. Important benchmarks and infinitesimal deformation simulations were conducted by loading an anisotropic elastic layer with various types of rigid indenter profiles [23]. Stress and deformation behavior of cellular materials were studied using two – scale

rough contact modeling. It was found that, anisotropic topology of material was fairly prominent on tribological behavior [24]. Effect of material anisotropy on the pressure distribution and contact patch was investigated using semi – analytical methods and elementary solutions [25]. It was shown that, symmetry axes on contact patch and stiffness along normal loading direction influenced pressure distribution on contact patch. Then, Knoop, Berkovich and Vickers indenters were used to load an anisotropic elastic surface to investigate the surface stresses and surface elasticity. It was shown that, displacement fields were closely related to anisotropic behavior of material and indenter profile [26]. Exact analytical solutions for the contact behavior of scintillator materials used in high – energy physics and medical applications were presented in terms of complex and real eigenvalues [27]. It was concluded that, optimizing punch profile and increasing elastic coefficient ratio reduced strength of stress singularities. Afterwards, contact mechanics and friction behavior of transversely isotropic solids were investigated using Persson’s theory. Findings showed that, anisotropy should be considered in analytical equations [28]. A new analytical model on adhesive contact of anisotropic materials were validated using Kendall – Roberts – Johnson theory and van der Waals force method. It was found that, surface mechanical property and elastic modulus in tangential direction affected maximum adhesion force on contact patch [29]. A novel iterative algorithm based on Lenard – Jones potential was developed to solve displacement and sub – surface stress fields for elastic solids [30]. Then, previous study was extended by considering multi – layered elastic solids [31]. Subsequently, an experimental and numerical study were conducted to assess the contact and friction behavior of transversely isotropic viscoelastics, where different types of specimens were utilized [32]. Combined effects of anisotropy and interface behavior on the indentation moduli were investigated using dual variable and position methods. Findings showed that, deformation mechanisms and changes in indentation moduli in thin – interlayer models were quite remarkable [33]. Exact and numerical solutions for a three – dimensional contact problem between two transversely isotropic bodies were presented within the framework of nonlinear boundary integration method [34].

Solution of contact mechanics problems with material orthotropy, monoclinic materials and laminated composites are also very difficult because of extra – added linked and unlinked stiffness constants, and lamina orientation angles. Analogy between the frictionless contact response of metal and polymer based composites was investigated using Fourier and Hilbert transforms [35]. It was shown that, stiffness constants in longitudinal and transverse directions influenced the deformation response of composite layers and concluded that, surface behavior of layered composite half – planes was mainly related to the amount of local bending around contact patch. Later, a high resemblance between contact and fracture mechanics was perceived. Based on this, a contact mechanics problem between two different types of indenter profiles and an orthotropic half – plane was considered. It was concluded that, indenter problems could be solved using methodologies belonging to fracture mechanics [36]. Three – dimensional contact analyses of spherical indenters were carried out using graded carbon fiber diffused epoxies. Experimental and numerical results showed that, orientation – graded specimens were more durable than cross – ply ones in loading direction [37]. Some contact examples and benchmarks regarding low transverse properties of composite half planes were presented analytically using Hilbert and Fourier transforms. Compared results showed that, transverse cracks weakened layers' performance under fatigue loads [38]. Afterwards, microhardness tests for polymer composites were carried out in terms of contact mechanics. Findings showed that, centrifugation condition was one of the most important stages in successfully adjusting particle distribution [39]. A general solution procedure for calculating surface stresses and contact patch on orthotropic materials was presented by diversifying geometrical parameters of problem [40]. By eliminating logarithmic singularities using direct asymptotic solutions, a contact problem between an orthotropic strip and a rigid punch was considered and some numerical examples were provided for different values of strip thicknesses [41]. Contact stiffness due to surface roughness of composite braking material samples was investigated using surface contact fracture theory and G – W model. It was found that, contact stiffness was generally greater than bulk stiffness, where the contact compliance happened at light loading scenarios [42]. A new mathematical model based on numerical integration method was generated to solve contact problems involving orthotropic

materials. It was shown that, interfacial contact patch and detailed stress fields could be easily obtained [43]. Rheological properties of polymer – matrix composites and their correlations with surface friction, roughness and material type were investigated in terms of contact mechanics. Brief analytical and experimental investigations showed that, thin composite films and monolayers could be used as lubricant material in modern engineering applications such as in memory storage devices and microelectromechanical systems [44]. Subsequently, closed – form solutions for an orthotropic medium loaded by different types of rigid indenters were presented using Krenk’s notation and singular integral equations. Presented numerical results showed that, effective Poisson’s ratio and stiffness ratio parameters had negligible effects on stresses and powers of stress singularities [45]. A new theoretical model to solve frictional sliding contact mechanics problems of monoclinic materials was proposed using Fourier transforms and Cauchy based integral equations. Results were given to show the influences of geometrical and material parameters, where underlying physics of the problem was discussed [46]. Frictional contact behavior of a rigid punch on a monoclinic half – plane with varying shear modulus in an arbitrary direction was investigated [47]. It was found that, proper evaluation of orientation angle, gradation parameter, and surface friction was very important in designing strong wear resistant surfaces. Mode I and II surface crack problems for orthotropic materials were investigated using analytical methods. It was concluded that, changes in material orthotropy and surface friction were greatly influenced mixed – mode stress intensity factors [48]. After that, a sliding contact problem for a coating / substrate system was considered by choosing an orthotropic coating material [49]. It was concluded that, soft coatings brought better surface performances in terms of surface wear and stress intensities. Using Gauss – Jacobi integration method and Fourier transforms, a highly parametric study on the contact behavior of an orthotropic layer was presented [50]. Findings showed that, soft surfaces could bear stresses more dispersedly than hard surfaces, which could increase surface performance in terms of wear and lubrication. Later, a dual approach solution for an orthotropic coating / isotropic substrate system was presented in terms of analytical and numerical solution methods, where the effects of material orthotropy, surface friction, and geometrical parameters were investigated [51]. It was monitored that, surface

cracks tended to be happen more on hard – coated surfaces than the soft – coated ones. Other comprehensive studies on material orthotropy, monoclinic and composite materials could be found in [52 – 54].

### **1.3. Aim and scope**

Explained in previous sections, the easiest way to transfer loads, moments, and displacements between parts used in engineering applications is to apply contact. In the proper nature of micro crack and wear resistant materials and surfaces, understanding the tribological behavior of these parts is a key. Several detailed research related to isotropic materials, material anisotropy, transversely isotropy, and orthotropy have been performed. An in depth analysis showed that, few studies on literature relating to monoclinic materials and laminated composites were performed because additional added related and unrelated constans of stiffness and variance in lamina orientation introduced difficulty to mathematical equations' solutions. In these studies, owing to the aforementioned complications, only the frictionless and / or frictional contact behavior of a single layer composite or a composite coated surface was investigated. To fill this gap, a contact mechanics problem between a frictional rigid cylinder and laminated glass fiber composites with different orientations is considered in this study. The purpose of this research, following the explanations, is to present a novel solution framework based on analytical and finite element methods that can be used to predict the frictional sliding contact behavior of laminated glass fiber composites. With regard to the target, it is possible to detail the scope of this study as

- Developing a novel analytical method based on Cholesky decomposition, Gauss elimination, Hermite orthogonal polynomials, Fourier transforms and singular integral equation (SIE)
- Developing a highly effective computational model based on augmented contact formulation (ACF) and finite element method
- Presenting the usage of quailified parametric work to test the accuracy and efficacy of the analytical and finite element methods
- Employing benchmarks to be used in industry



#### 1.4. Problem definition

It would be best to begin by describing the geometry of a single composite lamina before proceeding with the problem definition of laminated glass fiber composites as analytical method presented in Section (2) started with the formulations belonging to a single composite lamina. Presented in Fig. 6., a single composite lamina composed of embedded glass fiber, has a thickness  $h_l$  and width  $W$ , is considered prior to built up analytical method. It is pressed by a rigid cylinder has a radius of  $R$  using both concentrated normal  $P$  and horizontal forces  $Q = \eta P$  under plane strain and frictional contact conditions regarding Coulomb's static law of friction. The bottom surface is assumed to be fully bonded to a rigid substrate to prevent rotations and translations.

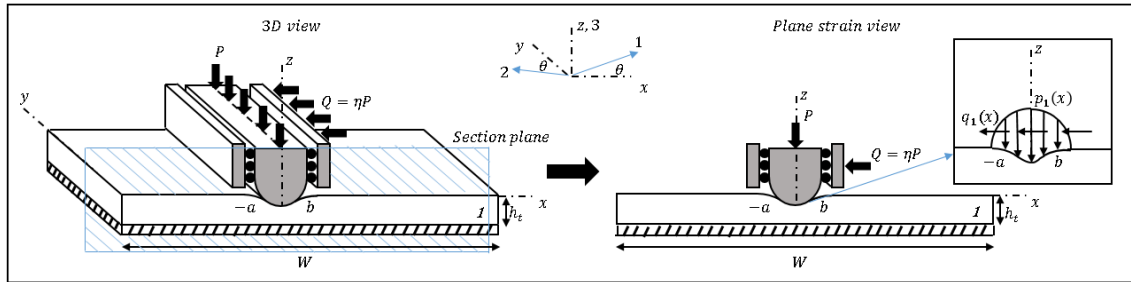


Fig. 6. Geometry of a single composite lamina

Furthermore, laminated glass fiber composite considered in this study composed of  $m$  number of laminae and consists glass fibers embedded in an epoxy matrix with 0 and 90 degree rotations. To limit layer transition and to easily seek the effect of lamina order on results,  $[0_{12}]$  and  $[90_{12}]$  configurations and  $[0_3/90_3]_s$ ,  $[90_3/0_3]_s$ ,  $[0_3/90_3]_2$ , and  $[90_3/0_3]_2$  configurations are chosen. The problem geometry is presented in Fig. 7, where each laminated glass fiber composite assumed to has a total thickness  $h_l$  and total width  $W$  of 4.5mm and 90mm, respectively. Identical to a single composite lamina, a rigid cylinder, with a radius of  $R$  is used to load the laminated glass fiber composite. It is subjected to a concentrated normal force  $P$  and a horizontal force  $Q = \eta P$  under plane strain conditions. For the surface friction, Coulomb's static law of friction is used, where the coefficient of friction denoted using  $\eta$ . The bottom surface of the laminated

glass fiber composite is assumed to be fully bonded to a rigid substrate, where all rotations and translations are fixed on  $-x$ ,  $-y$ , and  $-z$  global and  $-1$ ,  $-2$ , and  $-3$  local directions. Note that, for the configurations considered  $m=12$ , where each lamina has a thickness  $h$  of  $0.375\text{mm}$ .

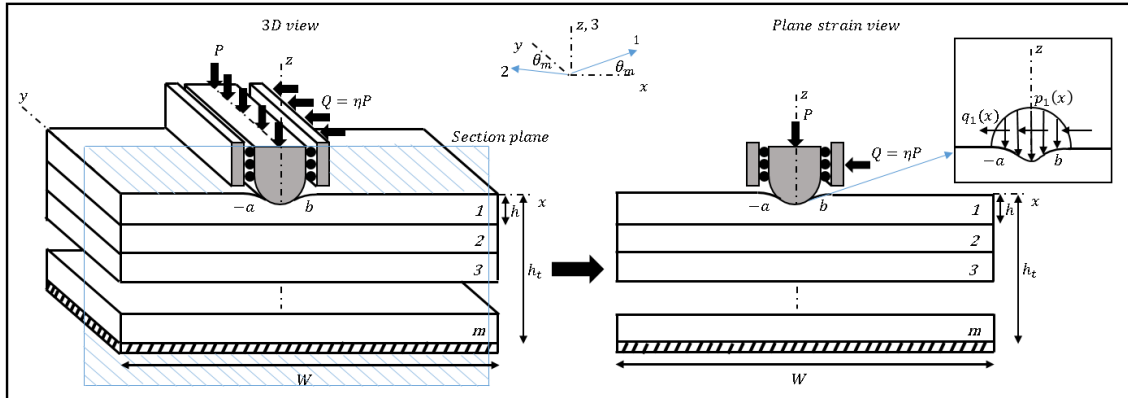


Fig. 7. Geometry of a laminated glass fiber composite

Furthermore, in Table 1, individual glass fiber and epoxy matrix material parameters are presented.

Table 1. Material parameters for individual glass fiber and epoxy matrix

Parameter Name	Value	Parameter Name	Value
$E_f$ (GPa)	72.1	$E_m$ (GPa)	2.56
	40		60
$V_f$ (%)	50	$V_m$ (%)	50
	60		40
$\mu_f$ (GPa)	29.1	$\mu_m$ (GPa)	0.9
$\nu_f$	0.22	$\nu_m$	0.35

## 2. ANALYTICAL METHOD

### 2.1. Calculations for the material parameters for a single composite lamina

Calculations for the material parameters start with the evaluation of properties of a single composite lamina. Using the individual glass fiber and epoxy matrix material parameters [55], formulation is implemented to obtain lamina properties as given in following:

$$E_{xx} = E_f V_f + E_m V_m \quad (1a)$$

$$E_{yy} = \frac{E_m}{1 - \left[ \sqrt{V_f} \left( 1 - \frac{E_m}{E_f} \right) \right]} \quad (1b)$$

$$E_{zz} = E_{yy} \quad (1c)$$

$$\mu_{xy} = \frac{\mu_m}{1 - \left[ \sqrt{V_f} \left( 1 - \frac{\mu_m}{\mu_f} \right) \right]} \quad (1d)$$

$$\mu_{yz} = \mu_{xy} \quad (1e)$$

$$\mu_{xz} = \mu_{xy} \quad (1f)$$

$$\nu_{xy} = \nu_f V_f + \nu_m V_m \quad (1g)$$

$$\nu_{xz} = \nu_{xy} \quad (1h)$$

$$\nu_{yx} = \nu_{xy} \frac{E_{yy}}{E_{xx}} \quad (1i)$$

$$\nu_{zx} = \nu_{yx} \quad (1h)$$

$$\nu_{yz} = \nu_{xy} \frac{1 - \nu_{yx}}{1 - \nu_{xy}} \quad (1j)$$

$$\nu_{zy} = \nu_{yz} \quad (1k)$$

where  $E_f$ ,  $V_f$ ,  $E_m$ , and  $V_m$  are the elastic moduli and volume fractions;  $\mu_f$ ,  $\nu_f$ ,  $\mu_m$ , and  $\nu_m$  represent shear moduli and Poisson's ratios of glass fiber and epoxy

matrix, respectively. It is known that, some common engineering materials and two – ply reinforced composites exhibit material orthotropy, where the material has orthogonal planes of symmetry and material property is independent along symmetry planes. The constitutive relation for material orthotropy can be written as

$$\begin{bmatrix} \sigma_{xx} \\ \sigma_{yy} \\ \sigma_{zz} \\ \sigma_{yz} \\ \sigma_{xz} \\ \sigma_{xy} \end{bmatrix} = \begin{bmatrix} C_{11} & C_{12} & C_{13} & 0 & 0 & 0 \\ C_{21} & C_{22} & C_{23} & 0 & 0 & 0 \\ C_{31} & C_{32} & C_{33} & 0 & 0 & 0 \\ 0 & 0 & 0 & C_{44} & 0 & 0 \\ 0 & 0 & 0 & 0 & C_{55} & 0 \\ 0 & 0 & 0 & 0 & 0 & C_{66} \end{bmatrix} \begin{bmatrix} \varepsilon_{xx} \\ \varepsilon_{yy} \\ \varepsilon_{zz} \\ \gamma_{yz} \\ \gamma_{xz} \\ \gamma_{xy} \end{bmatrix} \quad (2)$$

where  $C_{ij}$  ( $i=1,2,\dots,6, j=1,2,\dots,6$ ) represents the global stiffness constants along  $-x$ ,  $-y$ , and  $-z$  global directions and they can be obtained in terms of lamina properties given in Eq. (1) as follows:

$$C_{11} = \frac{1 - \nu_{yz}\nu_{zy}}{E_{yy}E_{zz}\Delta}, \quad C_{12} = \frac{\nu_{yx} + \nu_{zx}\nu_{yz}}{E_{yy}E_{zz}\Delta}, \quad C_{13} = \frac{\nu_{zx} + \nu_{yx}\nu_{zy}}{E_{yy}E_{zz}\Delta} \quad (3a)$$

$$C_{22} = \frac{1 - \nu_{zx}\nu_{xz}}{E_{zz}E_{xx}\Delta}, \quad C_{23} = \frac{\nu_{zy} + \nu_{zx}\nu_{xy}}{E_{zz}E_{xx}\Delta}, \quad C_{33} = \frac{1 - \nu_{xy}\nu_{yx}}{E_{xx}E_{yy}\Delta} \quad (3b)$$

$$C_{44} = \mu_{yz}, \quad C_{55} = \mu_{xz}, \quad C_{66} = \mu_{xy} \quad (3c)$$

where

$$\Delta = \frac{1 - \nu_{xy}\nu_{yx} - \nu_{yz}\nu_{zy} - \nu_{zx}\nu_{xz} - 2\nu_{xy}\nu_{yz}\nu_{zx}}{E_{xx}E_{yy}E_{zz}} \quad (4)$$

Note that, the global stiffness matrix  $[C_{ij}]$  ( $i=1,2,\dots,6, j=1,2,\dots,6$ ) given in Eq. (2) is symmetric by nature. Therefore,  $C_{12} = C_{21}$ ,  $C_{13} = C_{31}$ , and  $C_{23} = C_{32}$ .

## 2.2. Calculation of transformed rotated stiffness constants for a single composite lamina

Before providing calculation of transformed rotated stiffness constants  $\overline{C}_{ij}$ , it is needed to relate global stresses ( $\sigma_{xx}$ ,  $\sigma_{yy}$ ,  $\sigma_{zz}$ ,  $\sigma_{yz}$ ,  $\sigma_{xz}$ , and  $\sigma_{xy}$ ) and global strains ( $\varepsilon_{xx}$ ,  $\varepsilon_{yy}$ ,  $\varepsilon_{zz}$ ,  $\gamma_{yz}$ ,  $\gamma_{xz}$ , and  $\gamma_{xy}$ ) with local stresses ( $\sigma_{11}$ ,  $\sigma_{22}$ ,  $\sigma_{33}$ ,  $\sigma_{23}$ ,  $\sigma_{13}$ , and  $\sigma_{12}$ ) and local strains ( $\varepsilon_{11}$ ,  $\varepsilon_{22}$ ,  $\varepsilon_{33}$ ,  $\gamma_{23}$ ,  $\gamma_{13}$ , and  $\gamma_{12}$ ), respectively. To perform that, the following rotation matrix is introduced:

$$Q_{ij} = \cos(\alpha'_i, \alpha_j) \quad (5a)$$

$$Q_{ij} = \begin{bmatrix} rt_1 & rt_4 & rt_7 \\ rt_2 & rt_5 & rt_8 \\ rt_3 & rt_6 & rt_9 \end{bmatrix} \quad (5b)$$

where  $rt_i$  ( $i=1, 2, \dots, 9$ ) represents counterclockwise rotation cosines and sines between global and local directions, respectively. Using Eq. (5) and some trigonometrical manipulations, the global stresses ( $\sigma_{xx}$ ,  $\sigma_{yy}$ ,  $\sigma_{zz}$ ,  $\sigma_{yz}$ ,  $\sigma_{xz}$ , and  $\sigma_{xy}$ ) can be related with local stresses ( $\sigma_{11}$ ,  $\sigma_{22}$ ,  $\sigma_{33}$ ,  $\sigma_{23}$ ,  $\sigma_{13}$ , and  $\sigma_{12}$ ) as

$$[\sigma_{123}] = [T_1] [\sigma_{xyz}] \quad (6a)$$

$$[T_1] = \begin{bmatrix} \cos^2\theta & \sin^2\theta & 0 & 0 & 0 & 2\sin\theta\cos\theta \\ \sin^2\theta & \cos^2\theta & 0 & 0 & 0 & -2\sin\theta\cos\theta \\ 0 & 0 & 1 & 0 & 0 & 0 \\ 0 & 0 & 0 & \cos\theta & -\sin\theta & 0 \\ 0 & 0 & 0 & \sin\theta & \cos\theta & 0 \\ -\cos\theta\sin\theta & \cos\theta\sin\theta & 0 & 0 & 0 & \cos^2\theta\sin^2\theta \end{bmatrix} \quad (6b)$$

Identically, global strains ( $\varepsilon_{xx}$ ,  $\varepsilon_{yy}$ ,  $\varepsilon_{zz}$ ,  $\gamma_{yz}$ ,  $\gamma_{xz}$ , and  $\gamma_{xy}$ ) can be related with local strains ( $\varepsilon_{11}$ ,  $\varepsilon_{22}$ ,  $\varepsilon_{33}$ ,  $\gamma_{23}$ ,  $\gamma_{13}$ , and  $\gamma_{12}$ ) as

$$[\varepsilon_{123}] = [T_2] [\varepsilon_{xyz}] \quad (7a)$$

$$[T_2] = \begin{bmatrix} \cos^2\theta & \sin^2\theta & 0 & 0 & 0 & \sin\theta\cos\theta \\ \sin^2\theta & \cos^2\theta & 0 & 0 & 0 & -\sin\theta\cos\theta \\ 0 & 0 & 1 & 0 & 0 & 0 \\ 0 & 0 & 0 & \cos\theta & -\sin\theta & 0 \\ 0 & 0 & 0 & \sin\theta & \cos\theta & 0 \\ -2\cos\theta\sin\theta & 2\cos\theta\sin\theta & 0 & 0 & 0 & \cos^2\theta\sin^2\theta \end{bmatrix} \quad (7b)$$

Using following notations, transformed rotated stiffness constants  $\overline{C}_{ij}$  ( $i=1, 2, \dots, 6, j=1, 2, \dots, 6$ ) which forms transformed rotated stiffness matrix  $[\overline{C}_{ij}]$  ( $i=1, 2, \dots, 6, j=1, 2, \dots, 6$ ) can be obtained as

$$[T_1][\sigma_{xyz}] = [C_{ij}][T_2][\varepsilon_{xyz}] \quad (8a)$$

$$[\sigma_{xyz}] = [T_1]^{-1}[C_{ij}][T_2][\varepsilon_{xyz}] \quad (8b)$$

$$[\overline{C}_{ij}] = [T_1]^{-1}[C_{ij}][T_2] \quad (8c)$$

Transformed rotated stiffness matrix  $[\overline{C}_{ij}]$  ( $i=1, 2, \dots, 6, j=1, 2, \dots, 6$ ) given in Eq. (8c) represents material behavior of a single composite lamina having an arbitrary orientation through  $-z$  direction which leads a material symmetry on  $-xy$  plane. Thus, constitutive relation for material orthotropy presented in Eq. (2) transforms to following for a single composite lamina:

$$\begin{bmatrix} \sigma_{xx} \\ \sigma_{yy} \\ \sigma_{zz} \\ \sigma_{yz} \\ \sigma_{xz} \\ \sigma_{xy} \end{bmatrix} = \begin{bmatrix} \overline{C}_{11} & \overline{C}_{12} & \overline{C}_{13} & 0 & 0 & \overline{C}_{16} \\ \overline{C}_{21} & \overline{C}_{22} & \overline{C}_{23} & 0 & 0 & \overline{C}_{26} \\ \overline{C}_{31} & \overline{C}_{32} & \overline{C}_{33} & 0 & 0 & \overline{C}_{36} \\ 0 & 0 & 0 & \overline{C}_{44} & \overline{C}_{45} & 0 \\ 0 & 0 & 0 & \overline{C}_{54} & \overline{C}_{55} & 0 \\ \overline{C}_{61} & \overline{C}_{62} & \overline{C}_{63} & 0 & 0 & \overline{C}_{66} \end{bmatrix} \begin{bmatrix} \varepsilon_{xx} \\ \varepsilon_{yy} \\ \varepsilon_{zz} \\ \gamma_{yz} \\ \gamma_{xz} \\ \gamma_{xy} \end{bmatrix} \quad (9)$$

### 2.3. Derivation of displacement equations and stress – displacement relations for a single composite lamina

Using infinitesimal strain theory, strain – displacement relations can be expressed in component form as

$$\varepsilon_{xx} = \frac{\partial u}{\partial x}, \quad \varepsilon_{yy} = \frac{\partial v}{\partial y}, \quad \varepsilon_{zz} = \frac{\partial w}{\partial z} \quad (10a)$$

$$\varepsilon_{yz} = \frac{1}{2} \left( \frac{\partial v}{\partial z} + \frac{\partial w}{\partial y} \right) = \frac{1}{2} \gamma_{yz} \quad (10b)$$

$$\varepsilon_{xz} = \frac{1}{2} \left( \frac{\partial w}{\partial x} + \frac{\partial u}{\partial z} \right) = \frac{1}{2} \gamma_{xz} \quad (10c)$$

$$\varepsilon_{xy} = \frac{1}{2} \left( \frac{\partial u}{\partial y} + \frac{\partial v}{\partial x} \right) = \frac{1}{2} \gamma_{xy} \quad (10d)$$

Utilizing Eq. (10) and symmetry conditions for transformed rotated stiffness constants ( $\overline{C}_{16} = \overline{C}_{61}$ ,  $\overline{C}_{26} = \overline{C}_{62}$ ,  $\overline{C}_{36} = \overline{C}_{63}$ , and  $\overline{C}_{45} = \overline{C}_{54}$ ), Eq. (9) can be further expressed as

$$\sigma_{xx} = \overline{C}_{11} \frac{\partial u}{\partial x} + \overline{C}_{12} \frac{\partial v}{\partial y} + \overline{C}_{13} \frac{\partial w}{\partial z} + \overline{C}_{16} \left( \frac{\partial u}{\partial y} + \frac{\partial v}{\partial x} \right) \quad (11a)$$

$$\sigma_{yy} = \overline{C}_{12} \frac{\partial u}{\partial x} + \overline{C}_{22} \frac{\partial v}{\partial y} + \overline{C}_{23} \frac{\partial w}{\partial z} + \overline{C}_{26} \left( \frac{\partial u}{\partial y} + \frac{\partial v}{\partial x} \right) \quad (11b)$$

$$\sigma_{zz} = \overline{C}_{13} \frac{\partial u}{\partial x} + \overline{C}_{23} \frac{\partial v}{\partial y} + \overline{C}_{33} \frac{\partial w}{\partial z} + \overline{C}_{36} \left( \frac{\partial u}{\partial y} + \frac{\partial v}{\partial x} \right) \quad (11c)$$

$$\sigma_{yz} = \overline{C}_{44} \left( \frac{\partial v}{\partial z} + \frac{\partial w}{\partial y} \right) + \overline{C}_{45} \left( \frac{\partial w}{\partial x} + \frac{\partial u}{\partial z} \right) \quad (11d)$$

$$\sigma_{xz} = \overline{C}_{45} \left( \frac{\partial v}{\partial z} + \frac{\partial w}{\partial y} \right) + \overline{C}_{55} \left( \frac{\partial w}{\partial x} + \frac{\partial u}{\partial z} \right) \quad (11e)$$

$$\sigma_{xy} = \overline{C}_{16} \frac{\partial u}{\partial x} + \overline{C}_{26} \frac{\partial v}{\partial y} + \overline{C}_{36} \frac{\partial w}{\partial z} + \overline{C}_{66} \left( \frac{\partial u}{\partial y} + \frac{\partial v}{\partial x} \right) \quad (11f)$$

Then, using Eq. (11) along with equilibrium equations in terms of displacement components [56] following relations can be generated:

$$\begin{aligned} \overline{C}_{11} \frac{\partial^2 u}{\partial x^2} + \overline{C}_{12} \frac{\partial^2 v}{\partial x \partial y} + \overline{C}_{13} \frac{\partial^2 w}{\partial x \partial z} + \overline{C}_{16} \left( \frac{\partial^2 u}{\partial x \partial y} + \frac{\partial^2 v}{\partial x^2} + \frac{\partial^2 u}{\partial y \partial x} \right) + \overline{C}_{26} \frac{\partial^2 v}{\partial y^2} + \overline{C}_{36} \frac{\partial^2 w}{\partial y \partial z} \\ + \overline{C}_{45} \left( \frac{\partial^2 v}{\partial z^2} + \frac{\partial^2 w}{\partial z \partial y} \right) + \overline{C}_{55} \left( \frac{\partial^2 w}{\partial z \partial x} + \frac{\partial^2 u}{\partial z^2} \right) + \overline{C}_{66} \left( \frac{\partial^2 u}{\partial y^2} + \frac{\partial^2 v}{\partial y \partial x} \right) + F_x = 0 \end{aligned} \quad (12a)$$

$$\begin{aligned} \overline{C}_{12} \frac{\partial^2 u}{\partial y \partial x} + \overline{C}_{16} \frac{\partial^2 u}{\partial x^2} + \overline{C}_{22} \frac{\partial^2 v}{\partial y^2} + \overline{C}_{23} \frac{\partial^2 w}{\partial y \partial z} + \overline{C}_{26} \left( \frac{\partial^2 v}{\partial x \partial y} + \frac{\partial^2 u}{\partial y^2} + \frac{\partial^2 v}{\partial y \partial x} \right) + \overline{C}_{36} \frac{\partial^2 w}{\partial x \partial z} \\ + \overline{C}_{44} \left( \frac{\partial^2 v}{\partial z^2} + \frac{\partial^2 w}{\partial z \partial y} \right) + \overline{C}_{45} \left( \frac{\partial^2 w}{\partial z \partial x} + \frac{\partial^2 u}{\partial z^2} \right) + \overline{C}_{66} \left( \frac{\partial^2 u}{\partial x \partial y} + \frac{\partial^2 v}{\partial x^2} \right) + F_y = 0 \end{aligned} \quad (12b)$$

$$\begin{aligned} \overline{C}_{13} \frac{\partial^2 u}{\partial x \partial z} + \overline{C}_{23} \frac{\partial^2 v}{\partial z \partial y} + \overline{C}_{33} \frac{\partial^2 w}{\partial z^2} + \overline{C}_{36} \left( \frac{\partial^2 u}{\partial z \partial y} + \frac{\partial^2 v}{\partial z \partial x} \right) + \overline{C}_{44} \left( \frac{\partial^2 v}{\partial y \partial z} + \frac{\partial^2 w}{\partial y^2} \right) \\ + \overline{C}_{45} \left( \frac{\partial^2 v}{\partial x \partial z} + \frac{\partial^2 w}{\partial x \partial y} + \frac{\partial^2 w}{\partial y \partial x} + \frac{\partial^2 u}{\partial y \partial z} \right) + \overline{C}_{55} \left( \frac{\partial^2 w}{\partial x^2} + \frac{\partial^2 u}{\partial x \partial z} \right) + F_z = 0 \end{aligned} \quad (12c)$$

For two dimensional environment under plane strain conditions,  $u = u(x, z)$ ,  $v = v(x, z)$ ,  $w = w(x, z)$ ,  $\partial u / \partial y = 0$ ,  $\partial v / \partial y = 0$ , and  $\partial w / \partial y = 0$ . Neglecting body forces along  $-x$ ,  $-y$ , and  $-z$  global directions, Eq. (12) reduces to following set of two dimensional equilibrium equations relations in terms of displacement components:

$$\overline{C}_{11} \frac{\partial^2 u}{\partial x^2} + \overline{C}_{13} \frac{\partial^2 w}{\partial x \partial z} + \overline{C}_{16} \frac{\partial^2 v}{\partial x^2} + \overline{C}_{45} \frac{\partial^2 v}{\partial z^2} + \overline{C}_{55} \left( \frac{\partial^2 w}{\partial z \partial x} + \frac{\partial^2 u}{\partial z^2} \right) = 0 \quad (13a)$$

$$\overline{C}_{16} \frac{\partial^2 u}{\partial x^2} + \overline{C}_{36} \frac{\partial^2 w}{\partial x \partial z} + \overline{C}_{44} \frac{\partial^2 v}{\partial z^2} + \overline{C}_{45} \left( \frac{\partial^2 w}{\partial z \partial x} + \frac{\partial^2 u}{\partial z^2} \right) + \overline{C}_{66} \frac{\partial^2 v}{\partial x^2} = 0 \quad (13b)$$

$$\overline{C}_{13} \frac{\partial^2 u}{\partial x \partial z} + \overline{C}_{33} \frac{\partial^2 w}{\partial z^2} + \overline{C}_{36} \frac{\partial^2 v}{\partial z \partial x} + \overline{C}_{45} \frac{\partial^2 v}{\partial x \partial z} + \overline{C}_{55} \left( \frac{\partial^2 w}{\partial x^2} + \frac{\partial^2 u}{\partial x \partial z} \right) = 0 \quad (13c)$$

Identically, Eq. (11) reduces to following set of stress – displacement relations:

$$\sigma_{xx} = \overline{C}_{11} \frac{\partial u}{\partial x} + \overline{C}_{13} \frac{\partial w}{\partial z} + \overline{C}_{16} \frac{\partial v}{\partial x} \quad (14a)$$

$$\sigma_{yy} = \overline{C}_{12} \frac{\partial u}{\partial x} + \overline{C}_{23} \frac{\partial w}{\partial z} + \overline{C}_{26} \frac{\partial v}{\partial x} \quad (14b)$$

$$\sigma_{zz} = \overline{C}_{13} \frac{\partial u}{\partial x} + \overline{C}_{33} \frac{\partial w}{\partial z} + \overline{C}_{36} \frac{\partial v}{\partial x} \quad (14c)$$



$$\sigma_{yz} = \overline{C}_{44} \frac{\partial v}{\partial z} + \overline{C}_{45} \left( \frac{\partial w}{\partial x} + \frac{\partial u}{\partial z} \right) \quad (14d)$$

$$\sigma_{xz} = \overline{C}_{45} \frac{\partial v}{\partial z} + \overline{C}_{55} \left( \frac{\partial w}{\partial x} + \frac{\partial u}{\partial z} \right) \quad (14e)$$

$$\sigma_{xy} = \overline{C}_{16} \frac{\partial u}{\partial x} + \overline{C}_{36} \frac{\partial w}{\partial z} + \overline{C}_{66} \frac{\partial v}{\partial x} \quad (14f)$$

#### 2.4. Derivation of stress components and $k_j$ , $m_j$ , and $n_j$ expressions for a single composite lamina

Before deriving the stress components for a single composite lamina, it is needed to introduce following Fourier transform of displacements beforehand:

$$u(x, z) = \frac{1}{2\pi} \int_{-\infty}^{\infty} \overline{u}(\xi, z) e^{-I\xi x} d\xi \quad (15a)$$

$$v(x, z) = \frac{1}{2\pi} \int_{-\infty}^{\infty} \overline{v}(\xi, z) e^{-I\xi x} d\xi \quad (15b)$$

$$w(x, z) = \frac{1}{2\pi} \int_{-\infty}^{\infty} \overline{w}(\xi, z) e^{-I\xi x} d\xi \quad (15c)$$

where  $\overline{u}(\xi, z)$ ,  $\overline{v}(\xi, z)$ , and  $\overline{w}(\xi, z)$  are transformed displacement components of displacements  $u(x, z)$ ,  $v(x, z)$ , and,  $w(x, z)$ , respectively and can be obtained using

$$\overline{u}(\xi, z) = \sum_{j=1}^6 A_j e^{n_j \xi z} \quad (16a)$$

$$\overline{v}(\xi, z) = \sum_{j=1}^6 A_j m_j e^{n_j \xi z} \quad (16b)$$

$$\overline{w}(\xi, z) = \sum_{j=1}^6 IA_j k_j e^{n_j \xi z} \quad (16c)$$

Note that,  $\xi$  shown in Eq. (15) and Eq. (16) denotes an equation variable such as  $x$  and  $y$ , and  $I$  is imaginary unit ( $I = \sqrt{-1}$ ). Substituting Eq. (15) into Eq. (13), following set of ordinary different equations can be obtained:

$$-\overline{C_{11}}\xi^2\bar{u} - \overline{C_{13}}I\xi\frac{d\bar{w}}{dz} - \overline{C_{16}}\xi^2\bar{v} + \overline{C_{45}}\frac{d^2\bar{v}}{dz^2} + \overline{C_{55}}\frac{d^2\bar{u}}{dz^2} - \overline{C_{55}}I\xi\frac{d\bar{w}}{dz} = 0 \quad (17a)$$

$$\overline{C_{16}}\xi^2\bar{u} - \overline{C_{36}}I\xi\frac{d\bar{w}}{dz} + \overline{C_{44}}\frac{d^2\bar{v}}{dz^2} + \overline{C_{45}}\frac{d^2\bar{u}}{dz^2} - \overline{C_{45}}I\xi\frac{d\bar{w}}{dz} - \overline{C_{66}}\xi^2\bar{v} = 0 \quad (17b)$$

$$-\overline{C_{13}}I\xi\frac{d\bar{u}}{dz} + \overline{C_{33}}\frac{d^2\bar{w}}{dz^2} - \overline{C_{36}}I\xi\frac{d\bar{v}}{dz} - \overline{C_{45}}I\xi\frac{d\bar{v}}{dz} - \overline{C_{55}}\xi^2\bar{w} - \overline{C_{55}}I\xi\frac{d\bar{u}}{dz} = 0 \quad (17c)$$

To obtain stress components for a single composite lamina, it is needed to derive the partial derivatives of Fourier transforms given in Eq. (15) beforehand:

$$\frac{\partial u(x, z)}{\partial x} = \frac{\partial}{\partial x} \left[ \left( \int_{-\infty}^{\infty} \sum_{j=1}^6 A_j e^{n_j \xi z} \right) e^{-I\xi x} d\xi \right] = \int_{-\infty}^{\infty} \left( -I\xi \sum_{j=1}^6 A_j e^{n_j \xi z} \right) e^{-I\xi x} d\xi \quad (18a)$$

$$\frac{\partial u(x, z)}{\partial y} = \frac{\partial}{\partial y} \left[ \left( \int_{-\infty}^{\infty} \sum_{j=1}^6 A_j e^{n_j \xi z} \right) e^{-I\xi x} d\xi \right] = 0 \quad (18b)$$

$$\frac{\partial u(x, z)}{\partial z} = \frac{\partial}{\partial z} \left[ \left( \int_{-\infty}^{\infty} \sum_{j=1}^6 A_j e^{n_j \xi z} \right) e^{-I\xi x} d\xi \right] = \int_{-\infty}^{\infty} \left( \sum_{j=1}^6 A_j n_j \xi e^{n_j \xi z} \right) e^{-I\xi x} d\xi \quad (18c)$$

$$\frac{\partial v(x, z)}{\partial x} = \frac{\partial}{\partial x} \left[ \left( \int_{-\infty}^{\infty} \sum_{j=1}^6 A_j m_j e^{n_j \xi z} \right) e^{-I\xi x} d\xi \right] = \int_{-\infty}^{\infty} -I\xi \left( \sum_{j=1}^6 A_j m_j e^{n_j \xi z} \right) e^{-I\xi x} d\xi \quad (18d)$$

$$\frac{\partial v(x, z)}{\partial y} = \frac{\partial}{\partial y} \left[ \left( \int_{-\infty}^{\infty} \sum_{j=1}^6 A_j m_j e^{n_j \xi z} \right) e^{-I\xi x} d\xi \right] = 0 \quad (18e)$$

$$\frac{\partial v(x, z)}{\partial z} = \frac{\partial}{\partial z} \left[ \left( \int_{-\infty}^{\infty} \sum_{j=1}^6 A_j m_j e^{n_j \xi z} \right) e^{-I\xi x} d\xi \right] = \int_{-\infty}^{\infty} \left( \sum_{j=1}^6 A_j m_j n_j \xi e^{n_j \xi z} \right) e^{-I\xi x} d\xi \quad (18f)$$

$$\frac{\partial w(x, z)}{\partial x} = \frac{\partial}{\partial x} \left[ \left( \int_{-\infty}^{\infty} \sum_{j=1}^6 IA_j k_j e^{n_j \xi z} \right) e^{-I\xi x} d\xi \right] = \int_{-\infty}^{\infty} -I\xi \left( \sum_{j=1}^6 IA_j k_j e^{n_j \xi z} \right) e^{-I\xi x} d\xi \quad (18g)$$

$$\frac{\partial w(x, z)}{\partial y} = \frac{\partial}{\partial y} \left[ \left( \int_{-\infty}^{\infty} \sum_{j=1}^6 IA_j k_j e^{n_j \xi z} \right) e^{-I\xi x} d\xi \right] = 0 \quad (18h)$$

$$\frac{\partial w(x, z)}{\partial z} = \frac{\partial}{\partial z} \left[ \int_{-\infty}^{\infty} \sum_{j=1}^6 IA_j k_j e^{n_j \xi z} \right] e^{-I \xi x} d\xi = \int_{-\infty}^{\infty} \left( I \xi \sum_{j=1}^6 A_j k_j n_j e^{n_j \xi z} \right) e^{-I \xi x} d\xi \quad (18i)$$

Then, stress components for a single composite lamina can be obtained by substituting Eq. (18) into Eq. (14):

$$\sigma_{xx} = \frac{1}{2\pi} \int_{-\infty}^{\infty} -I \xi \sum_{j=1}^6 A_j e^{n_j \xi z} e^{-I \xi x} \left( \overline{C}_{11} - \overline{C}_{13} k_j n_j + \overline{C}_{16} m_j \right) d\xi \quad (19a)$$

$$\sigma_{yy} = \frac{1}{2\pi} \int_{-\infty}^{\infty} -I \xi \sum_{j=1}^6 A_j e^{n_j \xi z} e^{-I \xi x} \left( \overline{C}_{12} - \overline{C}_{23} k_j n_j + \overline{C}_{26} m_j \right) d\xi \quad (19b)$$

$$\sigma_{zz} = \frac{1}{2\pi} \int_{-\infty}^{\infty} -I \xi \sum_{j=1}^6 A_j e^{n_j \xi z} e^{-I \xi x} \left( \overline{C}_{13} - \overline{C}_{33} k_j n_j + \overline{C}_{36} m_j \right) d\xi \quad (19c)$$

$$\sigma_{yz} = \frac{1}{2\pi} \int_{-\infty}^{\infty} \xi \sum_{j=1}^6 A_j e^{n_j \xi z} e^{-I \xi x} \left( \overline{C}_{44} m_j n_j + \overline{C}_{45} (k_j + n_j) \right) d\xi \quad (19d)$$

$$\sigma_{xz} = \frac{1}{2\pi} \int_{-\infty}^{\infty} \xi \sum_{j=1}^6 A_j e^{n_j \xi z} e^{-I \xi x} \left( \overline{C}_{45} m_j n_j + \overline{C}_{55} (k_j + n_j) \right) d\xi \quad (19e)$$

$$\sigma_{xy} = \frac{1}{2\pi} \int_{-\infty}^{\infty} -I \xi \sum_{j=1}^6 A_j e^{n_j \xi z} e^{-I \xi x} \left( \overline{C}_{16} - \overline{C}_{36} k_j n_j + \overline{C}_{66} m_j \right) d\xi \quad (19f)$$

To obtain expressions for  $k_j$ ,  $m_j$ , and  $n_j$  ( $j=1, 2, \dots, 6$ ) firstly presented in Eq. (16), it is needed to calculate the second order partial derivatives of Fourier transforms given in Eq. (15) along with Eq. (13) as

$$\frac{\partial^2 u(x, z)}{\partial x^2} = \frac{\partial^2}{\partial x^2} \left[ \int_{-\infty}^{\infty} \sum_{j=1}^6 A_j e^{n_j \xi z} \right] e^{-I \xi x} d\xi = \int_{-\infty}^{\infty} -\xi^2 \left( \sum_{j=1}^6 A_j e^{n_j \xi z} \right) e^{-I \xi x} d\xi \quad (20a)$$

$$\frac{\partial^2 u(x, z)}{\partial z^2} = \frac{\partial^2}{\partial z^2} \left[ \int_{-\infty}^{\infty} \sum_{j=1}^6 A_j e^{n_j \xi z} \right] e^{-I \xi x} d\xi = \int_{-\infty}^{\infty} \xi^2 \left( \sum_{j=1}^6 A_j n_j^2 e^{n_j \xi z} \right) e^{-I \xi x} d\xi \quad (20b)$$

$$\frac{\partial^2 u(x, z)}{\partial z \partial x} = \frac{\partial^2}{\partial z \partial x} \left[ \int_{-\infty}^{\infty} \sum_{j=1}^6 A_j e^{n_j \xi z} \right] e^{-I \xi x} d\xi = \int_{-\infty}^{\infty} -I \xi^2 \left( \sum_{j=1}^6 A_j n_j e^{n_j \xi z} \right) e^{-I \xi x} d\xi \quad (20c)$$

$$\frac{\partial^2 v(x, z)}{\partial x^2} = \frac{\partial^2}{\partial x^2} \left[ \int_{-\infty}^{\infty} \sum_{j=1}^6 A_j m_j e^{n_j \xi z} \right] e^{-I \xi x} d\xi = \int_{-\infty}^{\infty} -\xi^2 \left( \sum_{j=1}^6 A_j m_j e^{n_j \xi z} \right) e^{-I \xi x} d\xi \quad (20d)$$

$$\frac{\partial^2 v(x, z)}{\partial z^2} = \frac{\partial^2}{\partial z^2} \left[ \left( \int_{-\infty}^{\infty} \sum_{j=1}^6 A_j m_j e^{n_j \xi z} \right) e^{-I \xi x} d\xi \right] = \int_{-\infty}^{\infty} \xi^2 \left( \sum_{j=1}^6 A_j m_j n_j^2 e^{n_j \xi z} \right) e^{-I \xi x} d\xi \quad (20e)$$

$$\frac{\partial^2 v(x, z)}{\partial z \partial x} = \frac{\partial^2}{\partial z \partial x} \left[ \left( \int_{-\infty}^{\infty} \sum_{j=1}^6 A_j m_j e^{n_j \xi z} \right) e^{-I \xi x} d\xi \right] = \int_{-\infty}^{\infty} -I \xi^2 \left( \sum_{j=1}^6 A_j m_j n_j e^{n_j \xi z} \right) e^{-I \xi x} d\xi \quad (20f)$$

$$\frac{\partial^2 w(x, z)}{\partial x^2} = \frac{\partial^2}{\partial x^2} \left[ \left( \int_{-\infty}^{\infty} \sum_{j=1}^6 I A_j k_j e^{n_j \xi z} \right) e^{-I \xi x} d\xi \right] = \int_{-\infty}^{\infty} -I \xi^2 \left( \sum_{j=1}^6 A_j k_j e^{n_j \xi z} \right) e^{-I \xi x} d\xi \quad (20g)$$

$$\frac{\partial^2 w(x, z)}{\partial z^2} = \frac{\partial^2}{\partial z^2} \left[ \left( \int_{-\infty}^{\infty} \sum_{j=1}^6 I A_j k_j e^{n_j \xi z} \right) e^{-I \xi x} d\xi \right] = \int_{-\infty}^{\infty} I \xi^2 \left( \sum_{j=1}^6 A_j k_j n_j^2 e^{n_j \xi z} \right) e^{-I \xi x} d\xi \quad (20h)$$

$$\frac{\partial^2 w(x, z)}{\partial x \partial z} = \frac{\partial^2}{\partial x \partial z} \left[ \left( \int_{-\infty}^{\infty} \sum_{j=1}^6 I A_j k_j e^{n_j \xi z} \right) e^{-I \xi x} d\xi \right] = \int_{-\infty}^{\infty} \xi^2 \left( \sum_{j=1}^6 A_j k_j n_j e^{n_j \xi z} \right) e^{-I \xi x} d\xi \quad (20i)$$

After some mathematical manipulations, Eq. (13) transforms into following:

$$\int_{-\infty}^{\infty} -\xi^2 \sum_{j=1}^6 A_j e^{n_j \xi z} e^{-I \xi x} \left[ \overline{C}_{11} - \overline{C}_{13} k_j n_j + \overline{C}_{16} m_j - \overline{C}_{45} m_j n_j^2 - C_{55} (k_j n_j + n_j^2) \right] d\xi = 0 \quad (21a)$$

$$\int_{-\infty}^{\infty} -\xi^2 \sum_{j=1}^6 A_j e^{n_j \xi z} e^{-I \xi x} \left[ \overline{C}_{16} - \overline{C}_{36} k_j n_j - \overline{C}_{44} m_j n_j^2 - \overline{C}_{45} (k_j n_j + n_j^2) + \overline{C}_{66} m_j \right] d\xi = 0 \quad (21b)$$

$$\int_{-\infty}^{\infty} -\xi^2 \sum_{j=1}^6 A_j e^{n_j \xi z} e^{-I \xi x} \left[ \overline{C}_{13} n_j - \overline{C}_{33} k_j n_j^2 + \overline{C}_{36} m_j n_j + \overline{C}_{45} m_j n_j + \overline{C}_{55} (k_j + n_j) \right] d\xi = 0 \quad (21c)$$

As sub – equations in Eq. (21) are equal to zero, multiplying terms outside square brackets can be omitted. Thence, Eq. (21) yields to following equations:

$$-\overline{C}_{11} + \overline{C}_{13} k_j n_j - \overline{C}_{16} m_j + \overline{C}_{45} m_j n_j^2 + C_{55} (k_j n_j + n_j^2) = 0 \quad (22a)$$

$$-\overline{C}_{16} + \overline{C}_{36} k_j n_j + \overline{C}_{44} m_j n_j^2 + \overline{C}_{45} (k_j n_j + n_j^2) - \overline{C}_{66} m_j = 0 \quad (22b)$$

$$\overline{C}_{13} n_j - \overline{C}_{33} k_j n_j^2 + \overline{C}_{36} m_j n_j + \overline{C}_{45} m_j n_j + \overline{C}_{55} (k_j + n_j) = 0 \quad (22c)$$

Solving Eq. (22), a characteristic equation in terms of  $n_j$  ( $j = 1, 2, \dots, 6$ ) can be obtained as

$$L_4 n_j^6 + L_3 n_j^4 + L_2 n_j^2 + L_1 = 0 \quad (23)$$

where

$$L_1 = \overline{C_{55}}(\overline{C_{16}}^2 - \overline{C_{11}}\overline{C_{66}}) \quad (24a)$$

$$L_2 = -(\overline{C_{16}}^2\overline{C_{33}} - 2\overline{C_{16}}(\overline{C_{13}}(\overline{C_{36}} + \overline{C_{45}}) + \overline{C_{36}}\overline{C_{55}}) + \overline{C_{13}}(\overline{C_{13}} + 2\overline{C_{55}})\overline{C_{66}} + \overline{C_{11}}((\overline{C_{36}} + \overline{C_{45}})^2 - \overline{C_{44}}\overline{C_{55}} - \overline{C_{33}}\overline{C_{66}})) \quad (24b)$$

$$L_3 = (\overline{C_{13}}^2\overline{C_{44}} - 2\overline{C_{13}}\overline{C_{45}}(\overline{C_{36}} + \overline{C_{45}}) + \overline{C_{36}}^2\overline{C_{55}} + 2\overline{C_{13}}\overline{C_{44}}\overline{C_{55}} - \overline{C_{33}}(\overline{C_{11}}\overline{C_{44}} - 2\overline{C_{16}}\overline{C_{45}} + \overline{C_{55}}\overline{C_{66}})) \quad (24c)$$

$$L_4 = -\overline{C_{33}}(\overline{C_{45}}^2 - \overline{C_{44}}\overline{C_{55}}) \quad (24d)$$

After obtaining  $n_j$  ( $j = 1, 2, \dots, 6$ ) by solving Eq. (24),  $m_j$  and  $k_j$  ( $j = 1, 2, \dots, 6$ ) can be found using

$$m_j = \frac{\overline{C_{16}}(-\overline{C_{55}} + \overline{C_{33}}n_j^2) - n_j^2(\overline{C_{13}}(\overline{C_{36}} + \overline{C_{45}}) + \overline{C_{36}}\overline{C_{55}} + \overline{C_{33}}\overline{C_{45}}n_j^2)}{(\overline{C_{36}} + \overline{C_{45}})^2n_j^2 + (\overline{C_{55}} - \overline{C_{33}}n_j^2)(\overline{C_{55}} - \overline{C_{44}}n_j^2)} \quad (25)$$

$$k_j = \frac{(\overline{C_{13}} + \overline{C_{55}} + (\overline{C_{36}} + \overline{C_{45}})m_j)n_j}{-\overline{C_{55}} + \overline{C_{33}}n_j^2} \quad (26)$$

## 2.5. Boundary conditions and singular integral equation (SIE) for a single composite lamina

Presented in Fig. 6, boundary conditions at the top and bottom surfaces of a single composite lamina can be written as

$$\sigma_{zz}(x, 0) = \begin{cases} -p(x) & -a < x < b \\ 0 & x \leq -a, x \geq b \end{cases} \quad (27a)$$

$$\sigma_{yz}(x, 0) = 0 \quad (27b)$$

$$\sigma_{xz}(x, 0) = \begin{cases} -\eta p(x) & -a < x < b \\ 0 & x \leq -a, x \geq b \end{cases} \quad (27c)$$

$$u(x, -h_t) = 0 \quad (27d)$$

$$v(x, -h_t) = 0 \quad (27e)$$

$$w(x, -h_i) = 0 \quad (27f)$$

where  $p(x)$  represents the surface contact stress. To calculate  $A_j$  ( $j = 1, 2, \dots, 6$ ) constants appearing firstly in Eq. (16), it is needed to obtain inverse Fourier transforms of displacement and stress components presented in Eq. (15) and Eq. (19) regarding boundary conditions of the problem as

$$\sigma_{zz}(x, 0) = -I\xi \sum_{j=1}^6 A_j e^{n_j \xi z} \left( \overline{C}_{13} - \overline{C}_{33} k_j n_j + \overline{C}_{36} m_j \right) \quad (28a)$$

$$\sigma_{yz}(x, 0) = \xi \sum_{j=1}^6 A_j e^{n_j \xi z} \left( \overline{C}_{44} m_j n_j + \overline{C}_{45} (k_j + n_j) \right) \quad (28b)$$

$$\sigma_{xz}(x, 0) = \xi \sum_{j=1}^6 A_j e^{n_j \xi z} \left( \overline{C}_{45} m_j n_j + \overline{C}_{55} (k_j + n_j) \right) \quad (28c)$$

$$\overline{u}(\xi, z) = \sum_{j=1}^6 A_j e^{n_j \xi z} \quad (28d)$$

$$\overline{v}(\xi, z) = \sum_{j=1}^6 A_j m_j e^{n_j \xi z} \quad (28e)$$

$$\overline{w}(\xi, z) = \sum_{j=1}^6 I A_j k_j e^{n_j \xi z} \quad (28f)$$

By combining Eq. (27) and Eq. (28), and applying boundary conditions, a set of equations can be created to obtain  $A_j$  ( $j = 1, 2, \dots, 6$ ) constants as

$$-I\xi \sum_{j=1}^6 A_j \left( \overline{C}_{13} - \overline{C}_{33} k_j n_j + \overline{C}_{36} m_j \right) = -p(x) \quad (29a)$$

$$\xi \sum_{j=1}^6 A_j \left( \overline{C}_{44} m_j n_j + \overline{C}_{45} (k_j + n_j) \right) = 0 \quad (29b)$$

$$\xi \sum_{j=1}^6 A_j \left( \overline{C}_{45} m_j n_j + \overline{C}_{55} (k_j + n_j) \right) = -\eta p(x) \quad (29c)$$

$$\sum_{j=1}^6 A_j e^{-n_j \xi h_i} = 0 \quad (29d)$$

$$\sum_{j=1}^6 m_j A_j e^{-n_j \xi h_j} = 0 \quad (29e)$$

$$\sum_{j=1}^6 I k_j A_j e^{-n_j \xi h_j} = 0 \quad (29f)$$

where,  $A_j$  ( $j = 1, 2, \dots, 6$ ) constants can be obtained by solving Eq. (29) with any system of equation solvers. As the profile of cylinder is rigid, deformed shape of the surface for a single composite lamina should be identical to the shape of the cylinder. Therefore,

$$w(x, 0) = -\delta + f(x) \quad (30a)$$

$$\frac{\partial w(x, 0)}{\partial x} = f'(x) \quad (30b)$$

where  $\delta$  and  $f(x)$  represent penetration depth and profile function, respectively. For a rigid cylinder, the profile function can be written as,

$$f(x) = \frac{x^2}{2R} \quad (31a)$$

$$f'(x) = \frac{x}{R} \quad (31b)$$

where  $R$  denotes the radius. Using Eq. (15c) and (31b), Eq. (30b) can be expanded as

$$\frac{\partial w(x, 0)}{\partial x} = \frac{1}{2\pi} \int_{-\infty}^{\infty} I(-I\xi) \left( \sum_{j=1}^6 A_j k_j \right) e^{-I\xi x} d\xi = f'(x) \quad (32)$$

where  $A_j$  ( $j = 1, 2, \dots, 6$ ) constants consists  $A_j^p$  and  $A_j^q$  sub – constants, which are formed by surface contact stress  $p(x)$  and surface in – plane stress  $q(x)$ . The expressions for surface contact stress  $p(x)$  and surface in – plane stress  $q(x)$  can be written as

$$\bar{p}(x) = \int_{-a}^b p(t) e^{I\xi t} dt \quad (33a)$$

$$\bar{q}(x) = \int_{-a}^b \eta p(t) e^{I\xi t} dt \quad (33b)$$

Furthermore, Eq. (32) can be written in an open form regarding  $A_j^p$  and  $A_j^q$  sub – constants as

$$\frac{\partial w(x, 0)}{\partial x} = \frac{1}{2\pi} \int_{-\infty}^{\infty} I(-I\xi) \left( \sum_{j=1}^6 (A_j^p \overline{p(x)} + A_j^q \overline{q(x)}) k_j \right) e^{-I\xi x} d\xi = f'(x) \quad (34)$$

Inserting Eq. (33) into Eq. (34) results to following equation:

$$\begin{aligned} \frac{\partial w(x, 0)}{\partial x} &= \frac{1}{2\pi} \int_{-\infty}^{\infty} I(-I\xi) \sum_{j=1}^6 A_j^p k_j \left( \int_{-a}^b p(t) e^{I\xi t} dt \right) e^{-I\xi x} d\xi \\ &+ \frac{1}{2\pi} \int_{-\infty}^{\infty} I(-I\xi) \sum_{j=1}^6 A_j^q k_j \left( \int_{-a}^b \eta p(t) e^{I\xi t} dt \right) e^{-I\xi x} d\xi = f'(x) \quad (-a < x < b) \end{aligned} \quad (35)$$

where  $-a$  and  $b$  denotes the edges of the contact patch. Then, arranging Eq. (35) following equation can be obtained:

$$\begin{aligned} \frac{\partial w(x, 0)}{\partial x} &= \frac{1}{2\pi} \int_{-a}^b p(t) \left[ \int_{-\infty}^{\infty} M_{10} e^{I\xi(t-x)} d\xi \right] dt \\ &+ \frac{1}{2\pi} \int_{-a}^b \eta p(t) \left[ \int_{-\infty}^{\infty} N_{10} e^{I\xi(t-x)} d\xi \right] dt = f'(x) \quad (-a < x < b) \end{aligned} \quad (36)$$

where

$$M_{10} = I(-I\xi) \sum_{j=1}^6 A_j^p k_j = \xi \sum_{j=1}^6 A_j^p k_j \quad (37a)$$

$$N_{10} = I(-I\xi) \sum_{j=1}^6 A_j^q k_j = \xi \sum_{j=1}^6 A_j^q k_j \quad (37b)$$

Introducing following relations

$$\int_{-\infty}^{\infty} M_{10} e^{I\xi(t-x)} d\xi = -2 \int_0^{\infty} \text{Im}[M_{10}] \sin(\xi(t-x)) d\xi \quad (38a)$$

$$\int_{-\infty}^{\infty} N_{10} e^{I\xi(t-x)} d\xi = 2 \int_0^{\infty} \text{Re}[M_{10}] \cos(\xi(t-x)) d\xi \quad (38b)$$

Inserting Eq. (38) into Eq. (36) yields to:



$$\begin{aligned} \frac{1}{\pi} \int_{-a}^b p(t) \left[ \int_0^{\infty} M_1 \sin(\xi(t-x)) d\xi \right] dt \\ + \frac{1}{\pi} \int_{-a}^b \eta p(t) \left[ \int_0^{\infty} N_1 \cos(\xi(t-x)) d\xi \right] dt = f'(x) \quad (-a < x < b) \end{aligned} \quad (39)$$

where

$$M_1 = -\text{Im}[M_{10}] = IM_{10} = I \xi \sum_{j=1}^6 A_j^p k_j \quad (40a)$$

$$N_1 = \text{Re}[M_{10}] = N_{10} = \xi \sum_{j=1}^6 A_j^q k_j \quad (40b)$$

To obviate the singularity in Eq. (39), two new constants are introduced:

$$\lim_{\xi \rightarrow \infty} M_1 = \psi_1 \quad (41a)$$

$$\lim_{\xi \rightarrow \infty} N_1 = \psi_2 \quad (41b)$$

Then, Eq. (39) becomes

$$\begin{aligned} \frac{1}{\pi} \int_{-a}^b p(t) \left[ \int_0^{\infty} (M_1 - \psi_1) \sin(\xi(t-x)) d\xi + \int_0^{\infty} \psi_1 \sin(\xi(t-x)) d\xi \right] dt \\ + \frac{1}{\pi} \int_{-a}^b \eta p(t) \left[ \int_0^{\infty} (N_1 - \psi_2) \cos(\xi(t-x)) d\xi + \int_0^{\infty} \psi_2 \cos(\xi(t-x)) d\xi \right] dt = f'(x) \quad (-a < x < b) \end{aligned} \quad (42)$$

Applying Fourier integral transformation [57] to Eq. (42), following singular integral equation (SIE) for a single composite lamina can be obtained:

$$\frac{\psi_2}{\psi_1} \eta p(x) + \frac{1}{\pi} \int_{-a}^b p(t) \left[ \frac{1}{t-x} + K_1(x,t) + \eta K_2(x,t) \right] dt = \frac{1}{\psi_1} f'(x) \quad (-a < x < b) \quad (43)$$

where

$$K_1(x,t) = \int_0^{\infty} \frac{1}{\psi_1} (M_1 - \psi_1) \sin(\xi(t-x)) d\xi \quad (44a)$$

$$K_2(x,t) = \int_0^{\infty} \frac{1}{\psi_1} (N_1 - \psi_2) \cos(\xi(t-x)) d\xi \quad (44b)$$

Note that, following equilibrium equation should also be satisfied:

$$\int_{-\infty}^{\infty} \sigma_{zz}(x,0)dx = \int_{-a}^b p(t)dt = P \quad (45)$$

Introducing following normalizations to modify the boundaries of singular integral equation (SIE) in Eq. (43)

$$t = \frac{b+a}{2}r + \frac{b-a}{2} \quad (46a)$$

$$x = \frac{b+a}{2}s + \frac{b-a}{2} \quad (46b)$$

Then, singular integral equation (SIE) in Eq. (43) and equilibrium equation in Eq. (45) transform to following equations:

$$\frac{\psi_2}{\psi_1} \eta p(s) + \frac{1}{\pi} \int_{-1}^1 p(r) \left[ \frac{1}{\frac{b+a}{2}(r-s)} + \overline{K}_1(s,r) + \eta \overline{K}_2(s,r) \right] \frac{b+a}{2} dr = \frac{1}{\psi_1} f'(s) \quad (47a)$$

$$\int_{-\infty}^{\infty} \sigma_{zz}(x,0)dx = \int_{-1}^1 p(r)dr = \frac{2P}{b+a} \quad (47b)$$

where

$$\overline{K}_1(s,r) = \frac{b+a}{2} \int_0^{\infty} (M_1 - \psi_1) \sin \left( \xi \left( \frac{b+a}{2}(r-s) \right) \right) d\xi \quad (48a)$$

$$\overline{K}_2(s,r) = \frac{b+a}{2} \int_0^{\infty} (N_1 - \psi_2) \cos \left( \xi \left( \frac{b+a}{2}(r-s) \right) \right) d\xi \quad (48b)$$

## 2.6. Solution of singular integral equation (SIE) and calculation of contact stress at the surface for a single composite lamina

The principal solution of singular integral equation (SIE) given in Eq. (47a) can be defined as follows:

$$p(r) = g(r)(1-r)^\alpha (1+r)^\beta \quad (49)$$

where

$$\alpha = \frac{1}{2\pi I} \ln \left[ \frac{\eta\psi_2/\psi_1 - I}{\eta\psi_2/\psi_1 + I} \right] + N_0 \quad (50a)$$

$$\beta = -\frac{1}{2\pi I} \ln \left[ \frac{\eta\psi_2/\psi_1 - I}{\eta\psi_2/\psi_1 + I} \right] + M_0 \quad (50b)$$

$N_0$  and  $M_0$  appearing in Eq. (50) are arbitrary integers and can be obtained by utilizing  $-1 < \text{Re}[\alpha, \beta] < 1$ . Using Gauss – Jacobi quadrature [58], singular integral equation (SIE) presented in Eq. (47a) can be converted to following numerical form:

$$\sum_{i=1}^N W_i^N g(r_i) \left[ \frac{1}{r_i - s_k} + \overline{K}_1(s_k, r_i) + \eta \overline{K}_2(s_k, r_i) \right] = \frac{1}{\psi_1} f'(s_k) \quad (k=1, 2, \dots, N - \chi) \quad (51)$$

where  $s_k$  and  $r_i$  are the roots of related Jacobi polynomials.

$$P_N^{(\alpha, \beta)} r_i = 0 \quad (i=1, 2, \dots, N) \quad (52a)$$

$$P_{N-\chi}^{(-\alpha, -\beta)} s_k = 0 \quad (i=1, 2, \dots, N - \chi) \quad (52b)$$

Note that,  $\chi$  is the index of singular integral equation (SIE) and it may vary according to indenter profile (for this study  $\chi = (\alpha + \beta) = -1$  as a rigid cylinder is used). Similar with Eq. (47a), Eq. (47b) can be converted to following numerical form:

$$\sum_{i=1}^N W_i^N g(r_i) = \frac{2P}{\pi(b+a)} \quad (53)$$

where  $W_i^N$  is weighting constant and can be defined as

$$W_i^N = \left[ -\frac{1}{\pi} \frac{(2N + \alpha + \beta + 2) \Gamma(N + \alpha + 1) \Gamma(N + \beta + 1) 2^{(\alpha + \beta)}}{(N+1)! \Gamma(N + \alpha + \beta + 2)} \right] \frac{1}{P_N^{(\alpha, \beta)} r_i P_{N+1}^{(\alpha, \beta)} r_i} \quad (54)$$

To determine the exact values of the edges of the contact patch  $-a$  and  $b$ , it is needed to acquire  $g(r_i)$  beforehand. To obtain it, Eq. (51) needs to be discretized for more than one value of  $N$  by monitoring approximate error between calculations. After that, unknown values for the edges of the contact patch  $-a$  and  $b$  can be obtained using Eq. (53) by employing root finding or bracketing methods. Then, surface contact stress over contact patch for a single composite

lamina can be found using Eq. (49). Here, a simple discretization example is presented using Eq. (51) by taking  $N = 2$ :

$$W_1^N \left[ \frac{1}{r_1 - s_1} + \overline{K}_1(s_1, r_1) + \eta \overline{K}_2(s_1, r_1) \right] g(r_1) + W_2^N \left[ \frac{1}{r_2 - s_1} + \overline{K}_1(s_1, r_2) + \eta \overline{K}_2(s_1, r_2) \right] g(r_2) = \frac{1}{\psi_1} \frac{1}{R} \left( \frac{a+b}{2} s_1 + \frac{b-a}{2} \right) \quad (55a)$$

$$W_1^N \left[ \frac{1}{r_1 - s_2} + \overline{K}_1(s_2, r_1) + \eta \overline{K}_2(s_2, r_1) \right] g(r_1) + W_2^N \left[ \frac{1}{r_2 - s_2} + \overline{K}_1(s_2, r_2) + \eta \overline{K}_2(s_2, r_2) \right] g(r_2) = \frac{1}{\psi_1} \frac{1}{R} \left( \frac{a+b}{2} s_2 + \frac{b-a}{2} \right) \quad (55b)$$

$$W_1^N \left[ \frac{1}{r_1 - s_3} + \overline{K}_1(s_3, r_1) + \eta \overline{K}_2(s_3, r_1) \right] g(r_1) + W_2^N \left[ \frac{1}{r_2 - s_3} + \overline{K}_1(s_3, r_2) + \eta \overline{K}_2(s_3, r_2) \right] g(r_2) = \frac{1}{\psi_1} \frac{1}{R} \left( \frac{a+b}{2} s_3 + \frac{b-a}{2} \right) \quad (55c)$$

where Eq. (55) can be simplified as

$$[A][X] = [B] \quad (56a)$$

$$\begin{bmatrix} W_1^N \left[ \frac{1}{r_1 - s_1} + \overline{K}_1(s_1, r_1) + \eta \overline{K}_2(s_1, r_1) \right] & W_2^N \left[ \frac{1}{r_2 - s_1} + \overline{K}_1(s_1, r_2) + \eta \overline{K}_2(s_1, r_2) \right] \\ W_1^N \left[ \frac{1}{r_1 - s_2} + \overline{K}_1(s_2, r_1) + \eta \overline{K}_2(s_2, r_1) \right] & W_2^N \left[ \frac{1}{r_2 - s_2} + \overline{K}_1(s_2, r_2) + \eta \overline{K}_2(s_2, r_2) \right] \\ W_1^N \left[ \frac{1}{r_1 - s_3} + \overline{K}_1(s_3, r_1) + \eta \overline{K}_2(s_3, r_1) \right] & W_2^N \left[ \frac{1}{r_2 - s_3} + \overline{K}_1(s_3, r_2) + \eta \overline{K}_2(s_3, r_2) \right] \end{bmatrix} \begin{bmatrix} g(r_1) \\ g(r_2) \end{bmatrix} = \begin{bmatrix} \frac{1}{\psi_1} \frac{1}{R} \left( \frac{a+b}{2} s_1 + \frac{b-a}{2} \right) \\ \frac{1}{\psi_1} \frac{1}{R} \left( \frac{a+b}{2} s_2 + \frac{b-a}{2} \right) \\ \frac{1}{\psi_1} \frac{1}{R} \left( \frac{a+b}{2} s_3 + \frac{b-a}{2} \right) \end{bmatrix} \quad (56b)$$

## 2.7. Calculation of in – plane stress at the surface for a single composite lamina

In – plane stress at the surface for a single composite lamina can be defined as

$$\sigma_{xx}(x,0) = \begin{cases} \psi_3 p(x) + H(x) & -a < x < b \\ H(x) & x \leq -a, x \geq b \end{cases} \quad (57)$$

where

$$H(x) = \frac{1}{\pi} \int_{-a}^b p(t) \left[ \frac{\psi_4 \eta}{t-x} + K_3(x,t) + \eta K_4(x,t) \right] dt \quad (58)$$

Sub – equations from Eq. (58) can be written as

$$K_3(x,t) = \int_0^\infty (M_2 - \psi_3) \cos(\xi(t-x)) d\xi \quad (59a)$$

$$K_4(x,t) = \int_0^\infty (N_2 - \psi_4) \sin(\xi(t-x)) d\xi \quad (59b)$$

To modify boundaries of singular integral equation (SIE) in Eq. (58), normalizations presented in Eq. (46) can be used. Then, Eq. (58) transforms to following equation:

$$H(x) = \frac{1}{\pi} \int_{-1}^1 p(r) \left[ \frac{\psi_4 \eta}{\frac{b+a}{2}(r-s)} + \overline{K}_3(s,r) + \eta \overline{K}_4(s,r) \right] \frac{b+a}{2} dr \quad (60)$$

where

$$\overline{K}_3(s,r) = \frac{b+a}{2} \int_0^\infty (M_2 - \psi_3) \cos\left(\xi \left(\frac{b+a}{2}(r-s)\right)\right) d\xi \quad (61a)$$

$$\overline{K}_4(s,r) = \frac{b+a}{2} \int_0^\infty (N_2 - \psi_4) \sin\left(\xi \left(\frac{b+a}{2}(r-s)\right)\right) d\xi \quad (61b)$$

Similarly, sub – equations that from Eq. (59) can be presented as

$$M_2 = -I \xi \sum_{j=1}^6 A_j^p \left( \overline{C}_{11} - \overline{C}_{36} k_j n_j + \overline{C}_{16} m_j \right) \quad (62a)$$

$$N_2 = I \left[ -I \xi \sum_{j=1}^6 A_j^q \left( \overline{C}_{11} - \overline{C}_{36} k_j n_j + \overline{C}_{16} m_j \right) \right] \quad (62b)$$

$$\lim_{\xi \rightarrow \infty} M_2 = \psi_3 \quad (62c)$$

$$\lim_{\xi \rightarrow \infty} N_2 = \psi_4 \quad (62d)$$

Employing Gauss – Jacobi quadrature, singular integral equation (SIE) in Eq. (60) can be transformed into numerical form to obtain surface in – plane stress over contact patch for a single composite lamina.

## 2.8. Calculation of in – plane stress at sub – surface for a single composite lamina

To calculate in – plane stress at sub – surface, it is needed to obtain  $K_3(x, t)$  and  $K_4(x, t)$  (see Eq. (59)) in symbolic form of equation variable  $\xi$  for each desired vertical location (between 0 and  $h_i$ ). To handle that,  $M_2$  and  $N_2$  sub – constants need to be acquired beforehand. Then,  $\psi_3$  and  $\psi_4$  sub – constants can be obtained to form  $M_2 - \psi_3$  and  $N_2 - \psi_4$  in integral equations. After that,  $K_3(x, t)$  and  $K_4(x, t)$  can be calculated for these vertical locations to be used in singular integral equation (SIE) (see Eq. (60)).

## 2.9. Transition of equations from a single composite lamina to laminated glass fiber composite

Proofs and explanations presented in previous sub – sections for a single composite lamina can be expanded for laminated glass fiber composite having identical or dissimilar orientations on  $m$  number of laminae through  $-z$  direction.

### 2.9.1. Material parameters

Similar to sub – section (2.1), calculation for the material parameters for a single composite lamina and laminated glass fiber composite is identical as either of them use individual glass fiber and epoxy matrix material parameters.

## 2.9.2. Transformed rotated stiffness constants

Considering sub – section (2.2), it is needed to relate global stresses ( $\sigma_{m,xx}$ ,  $\sigma_{m,yy}$ ,  $\sigma_{m,zz}$ ,  $\sigma_{m,yz}$ ,  $\sigma_{m,xz}$ , and  $\sigma_{m,xy}$ ) and global strains ( $\varepsilon_{m,xx}$ ,  $\varepsilon_{m,yy}$ ,  $\varepsilon_{m,zz}$ ,  $\gamma_{m,yz}$ ,  $\gamma_{m,xz}$ , and  $\gamma_{m,xy}$ ) with local stresses ( $\sigma_{m,11}$ ,  $\sigma_{m,22}$ ,  $\sigma_{m,33}$ ,  $\sigma_{m,23}$ ,  $\sigma_{m,13}$ , and  $\sigma_{m,12}$ ) and local strains ( $\varepsilon_{m,11}$ ,  $\varepsilon_{m,22}$ ,  $\varepsilon_{m,33}$ ,  $\gamma_{m,23}$ ,  $\gamma_{m,13}$ , and  $\gamma_{m,12}$ ) for  $m$  number of laminae. To do that, rotation matrix presented in Eq. (5) needs to be expanded beforehand:

$$Q_{m,ij} = \cos(\alpha_{m,i}, \alpha_{m,j}) \quad (63a)$$

$$Q_{m,ij} = \begin{bmatrix} rt_{m,1} & rt_{m,4} & rt_{m,7} \\ rt_{m,2} & rt_{m,5} & rt_{m,8} \\ rt_{m,3} & rt_{m,6} & rt_{m,9} \end{bmatrix} \quad (63b)$$

where  $rt_{m,i}$  ( $i=1, 2, \dots, 9$ ) represents counterclockwise rotation cosines and sines between global and local directions, respectively. Then, following relations can be presented to relate global stresses ( $\sigma_{m,xx}$ ,  $\sigma_{m,yy}$ ,  $\sigma_{m,zz}$ ,  $\sigma_{m,yz}$ ,  $\sigma_{m,xz}$ , and  $\sigma_{m,xy}$ ) and global strains ( $\varepsilon_{m,xx}$ ,  $\varepsilon_{m,yy}$ ,  $\varepsilon_{m,zz}$ ,  $\gamma_{m,yz}$ ,  $\gamma_{m,xz}$ , and  $\gamma_{m,xy}$ ) with local stresses ( $\sigma_{m,11}$ ,  $\sigma_{m,22}$ ,  $\sigma_{m,33}$ ,  $\sigma_{m,23}$ ,  $\sigma_{m,13}$ , and  $\sigma_{m,12}$ ) and local strains ( $\varepsilon_{m,11}$ ,  $\varepsilon_{m,22}$ ,  $\varepsilon_{m,33}$ ,  $\gamma_{m,23}$ ,  $\gamma_{m,13}$ , and  $\gamma_{m,12}$ ):

$$[\sigma_{m,123}] = [T_{m,1}] [\sigma_{m,xyz}] \quad (64a)$$

$$[T_{m,1}] = \begin{bmatrix} \cos^2\theta_m & \sin^2\theta_m & 0 & 0 & 0 & 2\sin\theta_m\cos\theta_m \\ \sin^2\theta_m & \cos^2\theta_m & 0 & 0 & 0 & -2\sin\theta_m\cos\theta_m \\ 0 & 0 & 1 & 0 & 0 & 0 \\ 0 & 0 & 0 & \cos\theta_m & -\sin\theta_m & 0 \\ 0 & 0 & 0 & \sin\theta_m & \cos\theta_m & 0 \\ -\cos\theta_m\sin\theta_m & \cos\theta_m\sin\theta_m & 0 & 0 & 0 & \cos^2\theta_m\sin^2\theta_m \end{bmatrix} \quad (64b)$$

$$[\varepsilon_{m,123}] = [T_{m,2}] [\varepsilon_{m,xyz}] \quad (64c)$$

$$[T_{m,2}] = \begin{bmatrix} \cos^2\theta_m & \sin^2\theta_m & 0 & 0 & 0 & \sin\theta_m \cos\theta_m \\ \sin^2\theta_m & \cos^2\theta_m & 0 & 0 & 0 & -\sin\theta_m \cos\theta_m \\ 0 & 0 & 1 & 0 & 0 & 0 \\ 0 & 0 & 0 & \cos\theta_m & -\sin\theta_m & 0 \\ 0 & 0 & 0 & \sin\theta_m & \cos\theta_m & 0 \\ -2\cos\theta_m \sin\theta_m & 2\cos\theta_m \sin\theta_m & 0 & 0 & 0 & \cos^2\theta_m \sin^2\theta_m \end{bmatrix} \quad (64d)$$

After that, transformed rotated stiffness constants  $\overline{C_{m,ij}}$  ( $i = 1, 2, \dots, 6$ ,  $j = 1, 2, \dots, 6$ ) which forms transformed rotated stiffness matrix  $[\overline{C_{m,ij}}]$  ( $i = 1, 2, \dots, 6$ ,  $j = 1, 2, \dots, 6$ ) can be obtained as

$$[T_{m,1}][\sigma_{m,xyz}] = [C_{ij}][T_{m,2}][\varepsilon_{m,xyz}] \quad (65a)$$

$$[\sigma_{m,xyz}] = [T_{m,1}]^{-1}[C_{ij}][T_{m,2}][\varepsilon_{m,xyz}] \quad (65b)$$

$$[\overline{C_{m,ij}}] = [T_{m,1}]^{-1}[C_{ij}][T_{m,2}] \quad (65c)$$

### 2.9.3. Displacement equations and stress – displacement relations

Proofs and explanations for Eqs. (10) – (12) are given in sub – section (2.2). Therefore, they are not included in here. Considering Eq. (13), two dimensional equilibrium equations relations in terms of displacement components for  $m$  number of laminae can be given as

$$\overline{C_{m,11}} \frac{\partial^2 u_m}{\partial x^2} + \overline{C_{m,13}} \frac{\partial^2 w_m}{\partial x \partial z} + \overline{C_{m,16}} \frac{\partial^2 v_m}{\partial x^2} + \overline{C_{m,45}} \frac{\partial^2 v_m}{\partial z^2} + \overline{C_{m,55}} \left( \frac{\partial^2 w_m}{\partial z \partial x} + \frac{\partial^2 u_m}{\partial z^2} \right) = 0 \quad (65a)$$

$$\overline{C_{m,16}} \frac{\partial^2 u_m}{\partial x^2} + \overline{C_{m,36}} \frac{\partial^2 w_m}{\partial x \partial z} + \overline{C_{m,44}} \frac{\partial^2 v_m}{\partial z^2} + \overline{C_{m,45}} \left( \frac{\partial^2 w_m}{\partial z \partial x} + \frac{\partial^2 u_m}{\partial z^2} \right) + \overline{C_{m,66}} \frac{\partial^2 v_m}{\partial x^2} = 0 \quad (65b)$$

$$\overline{C_{m,13}} \frac{\partial^2 u_m}{\partial x \partial z} + \overline{C_{m,33}} \frac{\partial^2 w_m}{\partial z^2} + \overline{C_{m,36}} \frac{\partial^2 v_m}{\partial z \partial x} + \overline{C_{m,45}} \frac{\partial^2 v_m}{\partial x \partial z} + \overline{C_{m,55}} \left( \frac{\partial^2 w_m}{\partial x^2} + \frac{\partial^2 u_m}{\partial x \partial z} \right) = 0 \quad (65c)$$

Similarly stress – displacement relations presented in Eq.(14) can be broaden as,

$$\sigma_{m,xx} = \overline{C_{m,11}} \frac{\partial u_m}{\partial x} + \overline{C_{m,13}} \frac{\partial w_m}{\partial z} + \overline{C_{m,16}} \frac{\partial v_m}{\partial x} \quad (66a)$$



$$\sigma_{m,yy} = \overline{C_{m,12}} \frac{\partial u_m}{\partial x} + \overline{C_{m,23}} \frac{\partial w_m}{\partial z} + \overline{C_{m,26}} \frac{\partial v_m}{\partial x} \quad (66b)$$

$$\sigma_{m,zz} = \overline{C_{m,13}} \frac{\partial u_m}{\partial x} + \overline{C_{m,33}} \frac{\partial w_m}{\partial z} + \overline{C_{m,36}} \frac{\partial v_m}{\partial x} \quad (66c)$$

$$\sigma_{m,yz} = \overline{C_{m,44}} \frac{\partial v_m}{\partial z} + \overline{C_{m,45}} \left( \frac{\partial w_m}{\partial x} + \frac{\partial u_m}{\partial z} \right) \quad (66d)$$

$$\sigma_{m,xz} = \overline{C_{m,45}} \frac{\partial v_m}{\partial z} + \overline{C_{m,55}} \left( \frac{\partial w_m}{\partial x} + \frac{\partial u_m}{\partial z} \right) \quad (66e)$$

$$\sigma_{m,xy} = \overline{C_{m,16}} \frac{\partial u_m}{\partial x} + \overline{C_{m,36}} \frac{\partial w_m}{\partial z} + \overline{C_{m,66}} \frac{\partial v_m}{\partial x} \quad (66f)$$

#### 2.9.4. Stress components and $k_j$ , $m_j$ , and $n_j$ expressions

Regarding Eq. (15) and Eq. (16), the Fourier transforms of displacements for  $m$  number of laminae can be written as

$$u_m(x, z) = \frac{1}{2\pi} \int_{-\infty}^{\infty} \overline{u_m}(\xi, z) e^{-I\xi x} d\xi \quad (67a)$$

$$v_m(x, z) = \frac{1}{2\pi} \int_{-\infty}^{\infty} \overline{v_m}(\xi, z) e^{-I\xi x} d\xi \quad (67b)$$

$$w_m(x, z) = \frac{1}{2\pi} \int_{-\infty}^{\infty} \overline{w_m}(\xi, z) e^{-I\xi x} d\xi \quad (67c)$$

where the transformed displacement components become

$$\overline{u_m}(\xi, z) = \sum_{j=1}^6 A_{m,j} e^{n_{m,j}\xi z} \quad (68a)$$

$$\overline{v_m}(\xi, z) = \sum_{j=1}^6 A_{m,j} m_{m,j} e^{n_{m,j}\xi z} \quad (68b)$$

$$\overline{w_m}(\xi, z) = \sum_{j=1}^6 IA_{m,j} k_{m,j} e^{n_{m,j}\xi z} \quad (68c)$$

Identically, stress components presented in Eq. (19) transform to following:

$$\sigma_{m,xx} = \frac{1}{2\pi} \int_{-\infty}^{\infty} -I\xi \sum_{j=1}^6 A_{m,j} e^{n_{m,j}\xi z} e^{-I\xi x} \left( \overline{C_{m,11}} - \overline{C_{m,13}} k_{m,j} n_{m,j} + \overline{C_{m,16}} m_{m,j} \right) d\xi \quad (69a)$$

$$\sigma_{m,yy} = \frac{1}{2\pi} \int_{-\infty}^{\infty} -I\xi \sum_{j=1}^6 A_{m,j} e^{n_{m,j}\xi z} e^{-I\xi x} \left( \overline{C_{m,12}} - \overline{C_{m,23}} k_{m,j} n_{m,j} + \overline{C_{m,26}} m_{m,j} \right) d\xi \quad (69b)$$

$$\sigma_{m,zz} = \frac{1}{2\pi} \int_{-\infty}^{\infty} -I\xi \sum_{j=1}^6 A_{m,j} e^{n_{m,j}\xi z} e^{-I\xi x} \left( \overline{C_{m,13}} - \overline{C_{m,33}} k_{m,j} n_{m,j} + \overline{C_{m,36}} m_{m,j} \right) d\xi \quad (69c)$$

$$\sigma_{m,yz} = \frac{1}{2\pi} \int_{-\infty}^{\infty} \xi \sum_{j=1}^6 A_{m,j} e^{n_{m,j}\xi z} e^{-I\xi x} \left( \overline{C_{m,44}} m_{m,j} n_{m,j} + \overline{C_{m,45}} (k_{m,j} + n_{m,j}) \right) d\xi \quad (69d)$$

$$\sigma_{m,xz} = \frac{1}{2\pi} \int_{-\infty}^{\infty} \xi \sum_{j=1}^6 A_{m,j} e^{n_{m,j}\xi z} e^{-I\xi x} \left( \overline{C_{m,45}} m_{m,j} n_{m,j} + \overline{C_{m,55}} (k_{m,j} + n_{m,j}) \right) d\xi \quad (69e)$$

$$\sigma_{m,xy} = \frac{1}{2\pi} \int_{-\infty}^{\infty} -I\xi \sum_{j=1}^6 A_{m,j} e^{n_{m,j}\xi z} e^{-I\xi x} \left( \overline{C_{m,16}} - \overline{C_{m,36}} k_{m,j} n_{m,j} + \overline{C_{m,66}} m_{m,j} \right) d\xi \quad (69f)$$

Note that, Eq. (17) and Eq. (18) are not needed to widen stress components for  $m$  number of laminae, therefore they are not included here once again. In the same way, Eqs. (20) – (22) are also omitted. Furthermore, Eq. (23) and Eq. (24) become

$$L_{m,4} n_{m,j}^6 + L_{m,3} n_{m,j}^4 + L_{m,2} n_{m,j}^2 + L_{m,1} = 0 \quad (70)$$

where

$$L_{m,1} = \overline{C_{m,55}} (\overline{C_{m,16}}^2 - \overline{C_{m,11}} \overline{C_{m,66}}) \quad (71a)$$

$$L_{m,2} = -(\overline{C_{m,16}}^2 \overline{C_{m,33}} - 2\overline{C_{m,16}} (\overline{C_{m,13}} (\overline{C_{m,36}} + \overline{C_{m,45}}) + \overline{C_{m,36}} \overline{C_{m,55}}) + \overline{C_{m,13}} (\overline{C_{m,13}} + 2\overline{C_{m,55}}) \overline{C_{m,66}}) + \overline{C_{11}} ((\overline{C_{36}} + \overline{C_{45}})^2 - \overline{C_{44}} \overline{C_{55}} - \overline{C_{33}} \overline{C_{66}})) \quad (71b)$$

$$L_{m,3} = (\overline{C_{m,13}}^2 \overline{C_{m,44}} - 2\overline{C_{m,13}} \overline{C_{m,45}} (\overline{C_{m,36}} + \overline{C_{m,45}}) + \overline{C_{m,36}}^2 \overline{C_{m,55}} + 2\overline{C_{m,13}} \overline{C_{m,44}} \overline{C_{m,55}} - \overline{C_{m,33}} (\overline{C_{m,11}} \overline{C_{m,44}} - 2\overline{C_{m,16}} \overline{C_{m,45}} + \overline{C_{m,55}} \overline{C_{m,66}})) \quad (71c)$$

$$L_{m,4} = -\overline{C_{m,33}} (\overline{C_{m,45}}^2 - \overline{C_{m,44}} \overline{C_{m,55}}) \quad (71d)$$

Solving Eq. (70) yields  $n_{m,j}$  ( $j=1, 2, \dots, 6$ ) values for each laminae. Then, Eq. (25) and Eq. (26) can be expanded to obtain  $m_{m,j}$  ( $j=1, 2, \dots, 6$ ), and  $k_{m,j}$  ( $j=1, 2, \dots, 6$ ) as

$$m_{m,j} = \frac{\overline{C_{m,16}}(-\overline{C_{m,55}} + \overline{C_{m,33}n_{m,j}^2}) - n_{m,j}^2(\overline{C_{m,13}}(\overline{C_{m,36}} + \overline{C_{m,45}}) + \overline{C_{m,36}C_{m,55}} + \overline{C_{m,33}C_{m,45}n_{m,j}^2})}{(\overline{C_{m,36}} + \overline{C_{m,45}})^2 n_{m,j}^2 + (\overline{C_{m,55}} - \overline{C_{m,33}n_{m,j}^2})(\overline{C_{m,55}} - \overline{C_{m,44}n_{m,j}^2})} \quad (72)$$

$$k_{m,j} = \frac{(\overline{C_{m,13}} + \overline{C_{m,55}} + (\overline{C_{m,36}} + \overline{C_{m,45}})m_{m,j})n_{m,j}}{-\overline{C_{m,55}} + \overline{C_{m,33}n_{m,j}^2}} \quad (73)$$

### 2.9.5. Boundary conditions and singular integral equation (SIE)

Considering geometry of laminated glass fiber composite given in Fig. 7, Eq. (27) in sub – section (2.5) can be expanded for  $m$  number of laminae. In order to avoid confusion, the boundary conditions are separated and given separately for each lamina. Thus, boundary conditions of the top surface of the first lamina are given as follows:

$$\sigma_{1,zz}(x, 0) = \begin{cases} -p(x) & -a < x < b \\ 0 & x \leq -a, x \geq b \end{cases} \quad (74a)$$

$$\sigma_{1,yz}(x, 0) = 0 \quad (74b)$$

$$\sigma_{1,xz}(x, 0) = \begin{cases} -\eta p(x) & -a < x < b \\ 0 & x \leq -a, x \geq b \end{cases} \quad (74c)$$

At lamina interfaces, boundary conditions are almost identical to each other, therefore a single explanation for them can be written with ease:

$$u_c(x, -ch) - u_{c+1}(x, -ch) = 0 \quad (75a)$$

$$v_c(x, -ch) - v_{c+1}(x, -ch) = 0 \quad (75b)$$

$$w_c(x, -ch) - w_{c+1}(x, -ch) = 0 \quad (75c)$$

$$\sigma_{c,zz}(x, -ch) - \sigma_{c+1,zz}(x, -ch) = 0 \quad (75d)$$

$$\sigma_{c,yz}(x, -ch) - \sigma_{c+1,yz}(x, -ch) = 0 \quad (75e)$$

$$\sigma_{c,xz}(x, -ch) - \sigma_{c+1,xz}(x, -ch) = 0 \quad (75f)$$

where  $(c = 1, 2, \dots, m-1)$  and  $h = h_c / m$ . Then, boundary conditions at the bottom surface of  $m^{th}$  lamina can be presented as

$$u_m(x, -mh) = 0 \quad (76a)$$

$$v_m(x, -mh) = 0 \quad (76b)$$

$$w_m(x, -mh) = 0 \quad (76c)$$

To obtain symbolic expressions for  $A_{m,j}$  ( $j = 1, 2, \dots, 6$ ) constants, firstly appeared in Eq. (68), it is needed to obtain inverse Fourier transforms of stress and displacement expressions for each lamina (see Eq. (28), Eq. (67), and Eq. (69)) in advance. Then, combining them with Eqs. (74) – (76), following set of equations can be created:

$$-I\xi \sum_{j=1}^6 A_{1,j} \left( \overline{C_{1,13}} - \overline{C_{1,33}} k_{1,j} n_{1,j} + \overline{C_{1,36}} m_{1,j} \right) = -p(x) \quad (77a)$$

$$\xi \sum_{j=1}^6 A_{1,j} \left( \overline{C_{1,44}} m_{1,j} n_{1,j} + \overline{C_{1,45}} (k_{1,j} + n_{1,j}) \right) = 0 \quad (77b)$$

$$\xi \sum_{j=1}^6 A_{1,j} \left( \overline{C_{1,45}} m_{1,j} n_{1,j} + \overline{C_{1,55}} (k_{1,j} + n_{1,j}) \right) = -\eta p(x) \quad (77c)$$

$$\sum_{j=1}^6 A_{c,j} e^{-n_{c,j} \xi ch} - \sum_{j=1}^6 A_{c+1,j} e^{-n_{c+1,j} \xi ch} = 0 \quad (77d)$$

$$\sum_{j=1}^6 m_{c,j} A_{c,j} e^{-n_{c,j} \xi ch} - \sum_{j=1}^6 m_{c+1,j} A_{c+1,j} e^{-n_{c+1,j} \xi ch} = 0 \quad (77e)$$

$$\sum_{j=1}^6 I k_{c,j} A_{c,j} e^{-n_{c,j} \xi h} - \sum_{j=1}^6 I k_{c+1,j} A_{c+1,j} e^{-n_{c+1,j} \xi ch} = 0 \quad (77f)$$

$$\begin{aligned} -I\xi \sum_{j=1}^6 A_{c,j} e^{n_{c,j} \xi h} \left( \overline{C_{c,13}} - \overline{C_{c,33}} k_{c,j} n_{c,j} + \overline{C_{c,36}} m_{c,j} \right) \\ + I\xi \sum_{j=1}^6 A_{c+1,j} e^{n_{c+1,j} \xi ch} \left( \overline{C_{c+1,13}} - \overline{C_{c+1,33}} k_{c+1,j} n_{c+1,j} + \overline{C_{c+1,36}} m_{c+1,j} \right) = 0 \end{aligned} \quad (77g)$$

$$\begin{aligned} \xi \sum_{j=1}^6 A_{c,j} e^{n_{c,j} \xi ch} \left( \overline{C_{c,44}} m_{c,j} n_{c,j} + \overline{C_{c,45}} (k_{c,j} + n_{c,j}) \right) \\ - \xi \sum_{j=1}^6 A_{c+1,j} e^{n_{c+1,j} \xi ch} \left( \overline{C_{c+1,44}} m_{c+1,j} n_{c+1,j} + \overline{C_{c+1,45}} (k_{c+1,j} + n_{c+1,j}) \right) = 0 \end{aligned} \quad (77h)$$

$$\begin{aligned} \xi \sum_{j=1}^6 A_{c,j} e^{n_{c,j} \xi ch} \left( \overline{C_{c,45}} m_{c,j} n_{c,j} + \overline{C_{c,55}} (k_{c,j} + n_{c,j}) \right) \\ - \xi \sum_{j=1}^6 A_{c+1,j} e^{n_{c+1,j} \xi ch} \left( \overline{C_{c+1,45}} m_{c+1,j} n_{c+1,j} + \overline{C_{c+1,55}} (k_{c+1,j} + n_{c+1,j}) \right) = 0 \end{aligned} \quad (77i)$$

$$\sum_{j=1}^6 A_{m,j} e^{-n_{m,j} \xi mh} = 0 \quad (77j)$$

$$\sum_{j=1}^6 m_{m,j} A_{m,j} e^{-n_{m,j} \xi mh} = 0 \quad (77k)$$

$$\sum_{j=1}^6 I k_{m,j} A_{m,j} e^{-n_{m,j} \xi mh} = 0 \quad (77l)$$

where  $(c = 1, 2, \dots, m-1)$  and  $h = h_t / m$  again. For the configurations considered in this study  $m = 12$ . Thus,  $6m$  number of equations needs to be created. To further explain this, an example is given in the following, where Eq. (77) is expanded for a four – lamina order:

$$-I \xi \sum_{j=1}^6 A_{1,j} \left( \overline{C_{1,13}} - \overline{C_{1,33}} k_{1,j} n_{1,j} + \overline{C_{1,36}} m_{1,j} \right) = -p(x) \quad (78a)$$

$$\xi \sum_{j=1}^6 A_{1,j} \left( \overline{C_{1,44}} m_{1,j} n_{1,j} + \overline{C_{1,45}} (k_{1,j} + n_{1,j}) \right) = 0 \quad (78b)$$

$$\xi \sum_{j=1}^6 A_{1,j} \left( \overline{C_{1,45}} m_{1,j} n_{1,j} + \overline{C_{1,55}} (k_{1,j} + n_{1,j}) \right) = -\eta p(x) \quad (78c)$$

$$\sum_{j=1}^6 A_{1,j} e^{-n_{1,j} \xi h} - \sum_{j=1}^6 A_{2,j} e^{-n_{2,j} \xi h} = 0 \quad (78d)$$

$$\sum_{j=1}^6 m_{1,j} A_{1,j} e^{-n_{1,j} \xi h} - \sum_{j=1}^6 m_{2,j} A_{2,j} e^{-n_{2,j} \xi h} = 0 \quad (78e)$$

$$\sum_{j=1}^6 Ik_{1,j}A_{1,j}e^{-n_{1,j}\xi h} - \sum_{j=1}^6 Ik_{2,j}A_{2,j}e^{-n_{2,j}\xi h} = 0 \quad (78f)$$

$$\begin{aligned} -I\xi \sum_{j=1}^6 A_{1,j}e^{n_{1,j}\xi h} \left( \overline{C_{1,13}} - \overline{C_{1,33}}k_{1,j}n_{1,j} + \overline{C_{1,36}}m_{1,j} \right) \\ + I\xi \sum_{j=1}^6 A_{2,j}e^{n_{2,j}\xi h} \left( \overline{C_{2,13}} - \overline{C_{2,33}}k_{2,j}n_{2,j} + \overline{C_{2,36}}m_{2,j} \right) = 0 \end{aligned} \quad (78g)$$

$$\begin{aligned} \xi \sum_{j=1}^6 A_{1,j}e^{n_{1,j}\xi h} \left( \overline{C_{1,44}}m_{1,j}n_{1,j} + \overline{C_{1,45}}(k_{1,j} + n_{1,j}) \right) \\ - \xi \sum_{j=1}^6 A_{2,j}e^{n_{2,j}\xi h} \left( \overline{C_{2,44}}m_{2,j}n_{2,j} + \overline{C_{2,45}}(k_{2,j} + n_{2,j}) \right) = 0 \end{aligned} \quad (78h)$$

$$\begin{aligned} \xi \sum_{j=1}^6 A_{1,j}e^{n_{1,j}\xi h} \left( \overline{C_{1,45}}m_{1,j}n_{1,j} + \overline{C_{1,55}}(k_{1,j} + n_{1,j}) \right) \\ - \xi \sum_{j=1}^6 A_{2,j}e^{n_{2,j}\xi h} \left( \overline{C_{2,45}}m_{2,j}n_{2,j} + \overline{C_{2,55}}(k_{2,j} + n_{2,j}) \right) = 0 \end{aligned} \quad (78i)$$

$$\sum_{j=1}^6 A_{2,j}e^{-n_{2,j}\xi 2h} - \sum_{j=1}^6 A_{3,j}e^{-n_{3,j}\xi 2h} = 0 \quad (78j)$$

$$\sum_{j=1}^6 m_{2,j}A_{2,j}e^{-n_{2,j}\xi 2h} - \sum_{j=1}^6 m_{3,j}A_{3,j}e^{-n_{3,j}\xi 2h} = 0 \quad (78k)$$

$$\sum_{j=1}^6 Ik_{2,j}A_{2,j}e^{-n_{2,j}\xi 2h} - \sum_{j=1}^6 Ik_{3,j}A_{3,j}e^{-n_{3,j}\xi 2h} = 0 \quad (78l)$$

$$\begin{aligned} -I\xi \sum_{j=1}^6 A_{2,j}e^{n_{2,j}\xi 2h} \left( \overline{C_{2,13}} - \overline{C_{2,33}}k_{2,j}n_{2,j} + \overline{C_{2,36}}m_{2,j} \right) \\ + I\xi \sum_{j=1}^6 A_{3,j}e^{n_{3,j}\xi 2h} \left( \overline{C_{3,13}} - \overline{C_{3,33}}k_{3,j}n_{3,j} + \overline{C_{3,36}}m_{3,j} \right) = 0 \end{aligned} \quad (78m)$$

$$\begin{aligned} \xi \sum_{j=1}^6 A_{2,j}e^{n_{2,j}\xi 2h} \left( \overline{C_{2,44}}m_{2,j}n_{2,j} + \overline{C_{2,45}}(k_{2,j} + n_{2,j}) \right) \\ - \xi \sum_{j=1}^6 A_{3,j}e^{n_{3,j}\xi 2h} \left( \overline{C_{3,44}}m_{3,j}n_{3,j} + \overline{C_{3,45}}(k_{3,j} + n_{3,j}) \right) = 0 \end{aligned} \quad (78n)$$

$$\begin{aligned} \xi \sum_{j=1}^6 A_{2,j} e^{n_{2,j} \xi 2h} \left( \overline{C_{2,45}} m_{2,j} n_{2,j} + \overline{C_{2,55}} (k_{2,j} + n_{2,j}) \right) \\ - \xi \sum_{j=1}^6 A_{3,j} e^{n_{3,j} \xi 2h} \left( \overline{C_{3,45}} m_{3,j} n_{3,j} + \overline{C_{3,55}} (k_{3,j} + n_{3,j}) \right) = 0 \end{aligned} \quad (78o)$$

$$\sum_{j=1}^6 A_{3,j} e^{-n_{3,j} \xi 3h} - \sum_{j=1}^6 A_{4,j} e^{-n_{4,j} \xi 3h} = 0 \quad (78p)$$

$$\sum_{j=1}^6 m_{3,j} A_{3,j} e^{-n_{3,j} \xi 3h} - \sum_{j=1}^6 m_{4,j} A_{4,j} e^{-n_{4,j} \xi 3h} = 0 \quad (78r)$$

$$\sum_{j=1}^6 I k_{3,j} A_{3,j} e^{-n_{3,j} \xi 3h} - \sum_{j=1}^6 I k_{4,j} A_{4,j} e^{-n_{4,j} \xi 3h} = 0 \quad (78s)$$

$$\begin{aligned} -I \xi \sum_{j=1}^6 A_{3,j} e^{n_{3,j} \xi 3h} \left( \overline{C_{3,13}} - \overline{C_{3,33}} k_{3,j} n_{3,j} + \overline{C_{3,36}} m_{3,j} \right) \\ + I \xi \sum_{j=1}^6 A_{4,j} e^{n_{4,j} \xi 3h} \left( \overline{C_{4,13}} - \overline{C_{4,33}} k_{4,j} n_{4,j} + \overline{C_{4,36}} m_{4,j} \right) = 0 \end{aligned} \quad (78t)$$

$$\begin{aligned} \xi \sum_{j=1}^6 A_{3,j} e^{n_{3,j} \xi 3h} \left( \overline{C_{3,44}} m_{3,j} n_{3,j} + \overline{C_{3,45}} (k_{3,j} + n_{3,j}) \right) \\ - \xi \sum_{j=1}^6 A_{4,j} e^{n_{4,j} \xi 3h} \left( \overline{C_{4,44}} m_{4,j} n_{4,j} + \overline{C_{4,45}} (k_{4,j} + n_{4,j}) \right) = 0 \end{aligned} \quad (78u)$$

$$\begin{aligned} \xi \sum_{j=1}^6 A_{3,j} e^{n_{3,j} \xi 3h} \left( \overline{C_{3,45}} m_{3,j} n_{3,j} + \overline{C_{3,55}} (k_{3,j} + n_{3,j}) \right) \\ - \xi \sum_{j=1}^6 A_{4,j} e^{n_{4,j} \xi 3h} \left( \overline{C_{4,45}} m_{4,j} n_{4,j} + \overline{C_{4,55}} (k_{4,j} + n_{4,j}) \right) = 0 \end{aligned} \quad (78v)$$

$$\sum_{j=1}^6 A_{4,j} e^{-n_{4,j} \xi 4h} = 0$$

(78w)

$$\sum_{j=1}^6 m_{4,j} A_{4,j} e^{-n_{4,j} \xi 4h} = 0 \quad (78y)$$

$$\sum_{j=1}^6 I k_{4,j} A_{4,j} e^{-n_{4,j} \xi 4h} = 0 \quad (78z)$$

Deriving symbolic expressions dependent on equation variable  $\xi$  for  $A_{m,j}$  ( $j=1, 2, \dots, 6$ ) constants with conventional system of equation solvers are impossible (for instance, for  $m=4$ , the number of equations are 24 and for  $m=12$ , the number of equations are 72). For this reason, numerical values starting from zero to a predefined upper limit based on mathematical calculations are appointed to equation variable  $\xi$ . Then,  $A_{m,j}$  ( $j=1, 2, \dots, 6$ ) constants are obtained numerically for each  $\xi$  using Cholesky decomposition and Gauss elimination [59 – 60]. Note that, there is no change in the preparation of singular integral equation (SIE) proofs (see Eqs. (30) – (48)) for a single composite lamina and laminated glass fiber composite except for explanations between  $A_j$  ( $j=1, 2, \dots, 6$ ) and  $A_{m,j}$  ( $j=1, 2, \dots, 6$ ) constants. To obtain  $K_1(x,t)$  and  $K_2(x,t)$  (see Eq. (43) and Eq. (44)) in singular integral equation (SIE), it is needed to obtain  $M_1$  and  $N_1$  sub – constants for each  $\xi$ . To perform that,  $A_{m,j}$  ( $j=1, 2, \dots, 6$ ) constants needs to divided into  $A_{m,j}^p$  and  $A_{m,j}^q$  sub – constants as explained in sub – section (2.5). After that, related  $\psi_1$  and  $\psi_2$  sub – constants can be calculated numerically for each  $\xi$ . However, to utilize  $K_1(x,t)$  and  $K_2(x,t)$  in singular integral equation (SIE), sub – constants that form  $1/\psi_1(M_1 - \psi_1)$  and  $1/\psi_1(M_1 - \psi_2)$  in related integrals need to be converted into symbolic form. To do that, Hermite orthogonal polynomials and interpolating splines order of at least 8<sup>th</sup> can be used and  $1/\psi_1(M_1 - \psi_1)$  and  $1/\psi_1(M_1 - \psi_2)$  can be converted to symbolic form of equation variable  $\xi$  [61]. Subsequently,  $\overline{K}_1(x,t)$  and  $\overline{K}_2(x,t)$  can be implemented properly into singular integral equation (SIE). Curve fit plots for  $1/\psi_1(M_1 - \psi_1)$  and  $1/\psi_1(M_1 - \psi_2)$  for  $[90_3/0_3]_s$  configuration are shown in Appendix 1.



### 2.9.6 Solution of singular integral equation (SIE) and calculation of contact stress at the surface

Considering sub – section (2.6), Eqs. (49) – (56) are valid for calculation of contact stress at the surface for laminated glass fiber composite. Therefore, no further explanation is presented here.

### 2.9.7 Calculation of in – plane stress at the surface

Considering sub – section (2.7), proofs presented in Eqs. (57) – (62) can be used to calculate in – plane stress at the surface for laminated glass fiber composite. However, to calculate it properly, it is needed to obtain  $K_3(x,t)$  and  $K_4(x,t)$  beforehand (see Eq. (59)). To perform that,  $M_2$  and  $N_2$  sub – constants for each  $\xi$  need to be obtained using previously dismantled  $A_{m,j}^p$  and  $A_{m,j}^q$  sub – constants,. Then,  $\psi_3$  and  $\psi_4$  sub – constants can be acquired numerically to be used in  $M_2 - \psi_3$  and  $N_2 - \psi_4$ . In order to calculate integrals in Eq. (59),  $M_2 - \psi_3$  and  $N_2 - \psi_4$  need to be converted to symbolic form of equation variable  $\xi$  by employing Hermite orthogonal polynomials and interpolating splines order of at least  $8^{th}$ . After that,  $K_3(x,t)$  and  $K_4(x,t)$  can be added into singular integral equation (SIE) to acquire in – plane stress at the surface.

### 2.9.8 Calculation of in – plane stress at the sub – surface

Identical to calculation of in – plane stress at the sub – surface for a single composite lamina, it is needed to obtain  $K_3(x,t)$  and  $K_4(x,t)$  (see Eq. (59)) in symbolic form of equation variable  $\xi$  for each desired vertical location (between 0 and  $h_i$ ). However, sub – constants  $M_2$ ,  $N_2$ ,  $\psi_3$ , and  $\psi_4$  that form  $K_3(x,t)$  and  $K_4(x,t)$  are in numerical form at each vertical location. For this reason,  $M_2 - \psi_3$  and  $N_2 - \psi_4$  need to be converted to symbolic form of equation variable  $\xi$  by employing Hermite orthogonal polynomials and interpolating splines order of at

least  $8^{th}$ . Then,  $K_3(x,t)$  and  $K_4(x,t)$  can be calculated for these vertical locations to be used in singular integral equation (SIE) (see Eq. (60)).

### **3. FINITE ELEMENT METHOD**

#### **3.1. Literature review on contact mechanics and computational advances regarding finite element method, layered structures, and laminated composites**

Finite element method is a unique numerical technique in solving boundary value problems (BVPs) and partial differential equations (PDEs) approximately by subdividing problem domain into simpler parts named as finite elements. Structural analyses, numerical solution of heat, mass transfer, and contact mechanics problems, thermo – chemical, thermo – chemo – mechanical and bio – mechanical problems are the most obvious examples for the finite element method. The historical background of finite element method goes back to mid 1940s, where the scientific pillars were firstly constructed because of the need for solving complex structural problems in mechanical and aeronautical engineering. The first two studies were conducted to solve the stress fields in continuous plane elastic solids with element discretization methods [62 – 63]. In that studies, two different and unique approaches were presented and concluded to the identical comment in which they named these discretized units as finite elements.

Solution of sliding contact conditions using finite element method and reducing solution times by improving computing efficiency had received great attention in literature regarding layered structures and laminated composites. Effect of lamina orientation, macro matrix cracks, and delamination of layers were studied with finite element method by employing a contact mechanics problem between a laminated orthotropic beam and a rigid indenter. Findings were presented in terms of stress distributions and notch depths. It was found that, they were greatly affected by lamina orientation and shape of the indenter [64]. A new numerical method based on finite elements were presented to prevent micro crack formations around local yield positions for hard coated surfaces bonded to layered structures [65]. Then, a novel numerical algorithm was advanced to reveal surface stresses and contact kinematics of surfaces. It was concluded that, mortar finite elements have been found to be very effective in simulations compared to conventional finite elements [66]. After that, a contact algorithm

based on numerical methods was developed to investigate relations between surface roughness and lamina orientations. Analogy with experimental methods showed that developed contact algorithm could successfully predict dense contact regions and wear areas resulting from surface roughness and lamina orientations [67]. Contact capacities and efficiency of graded finite elements were investigated and parametric benchmark studies were presented to be served as a basis for onward studies [68]. To investigate the effect of surface friction on three dissimilar contact types, new and novel finite element simulations were carried out by pressing surfaces with Berkovich nanoindenters. It was revealed that, surface friction had great effect on post – processed results [69]. To assess the strength of contact surface and endurance limit of interlayers, an interesting multi – axial loading test was presented by employing ceramic laminates and rigid indenters. It was found that, interlayers could fail before the contact surface under intense loads [70]. Then, precision and effectiveness of element based and segment based mortar finite element integration types were compared, some numerical models were presented regarding computational contact mechanics [71]. Normal contact stress and wear depths were presented for a finite thick layer loaded by a rigid sphere. It was found that, dual mortar method based on Lagrangean shape functions were quite capable in modeling fretting wear effects [72]. Subsequently, accuracy of isogeometric dual mortar contact formulation was compared with classical finite element method. It is concluded that, isogeometric dual mortar contact formulation yielded smoother contact pressure distribution over contact patch [73]. Frictional contact effects and surface shape changes due to wear were investigated using Lagrangean finite elements. The results showed that, iterations between Lagrangean shape functions yielded faster convergence and robustness [74]. Two – scale asymptotic homogenization method was used to obtain elastic properties of a laminated shell composite with defective interface contacts. Results were compared with finite element and spherical assemblage model and concluded that, two – scale asymptotic homogenization method could be used in contact problems [75]. Three different contact conditions were utilized to investigate performance of Lagrange multipliers, where several numerical examples were provided using mortar finite elements [76].

### **3.2. Advantages of finite element method**

Finite element method is the most extensive numerical method to solve and analyze complex industrial problems. It is quite capable and accurate in modeling because mixed boundaries, material non – linearities

, and geometrical defects can be easily taken into account. Displacements, stresses, strains, strain – rates, damage, temperature, and forces can be easily implemented [77]. With the visualization of the problem, interior and exterior of complex geometries and erratic shapes can be optimized and configured. Problem related specifications can be readily adapted to increase accuracy and to decrease physical need in design and/or benchmark stages as transcribing these specifications physically can be excessively time consuming. Thus, safe simulation of potentially dangerous problems can be achieved. Furthermore, simultaneous calculation of physical parameters and/or desired results can be acquired to rapidly increase analyze performance.

### **3.3. Modeling of laminated glass fiber composite**

Finite element modeling of laminated glass fiber composite is implemented in this sub-section, where the numerical models are prepared using ANSYS Mechanical APDL R2020. Detailed examples and comments for finite element types, augmented contact formulation (ACF), model preparation, adaptive mesh refinement and solution descriptions are given below.

#### **3.3.1. Finite element types**

Laminated glass fiber composite considered in this study is modeled using 8 – noded quadrilateral *PLANE183* solid finite elements, where the element geometries and stress output are illustrated in Fig. 8. Using this element type; quadratic displacement behavior, irregular and regular mesh types, plane strain, plane stress, and generalized plane strain conditions can be implemented. This element offers successful prediction of creep, large deflection and stress, plasticity, elasticity, hyperelasticity, and stress stiffening behavior. It can be used as an axisymmetric or planar symmetric finite element, where symmetry conditions need to be defined in advance. It can also be utilized to model

enhanced stress formulations in cyclic symmetry analyses to apply cyclic loadings and to increase solution efficiency. Some important necessities and restrictions for this element regarding contact mechanics are presented below:

- To obtain a numerical solution, the area of the finite element must be greater than zero.
- To utilize symmetry conditions, vertical axis must be the axis of symmetry.
- Stress stiffening and pre – stress effects are always included in nonlinear analyses.
- To use mixed contact formulation, sparse solver must be activated.
- Rezoning and nonlinear contact adaptivity are not supported.
- Linear perturbation and material force evaluation are not supported.

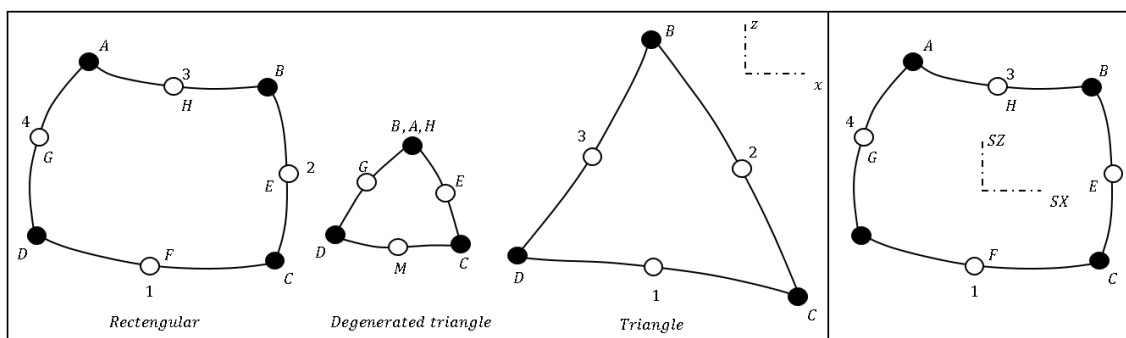


Fig. 8. Element geometries and stress output of *PLANE183* finite element

To represent rigid cylinder *TARGE169* target segment elements are utilized, where the element geometries and 2 – D segment element types are given in Fig. 9 and Fig. 10, respectively. Translational and rotational displacement, forces, moments, magnetic potential, temperature, voltage, concentration, and pore pressure can be imposed on target segment elements. It can be used for both pair – based and general contact types. In pair – based contact type, 2 – D target segment elements are associated with 2 – D contact line elements using an identical real constant set involving interaction properties, material parameters, and friction related terms. The target surface can be either flexible or rigid. For flexible – flexible contacts, one of the flexible surfaces must be identified using *TARGE169* target segment elements. For flexible – rigid contacts, rigid surface must be represented by *TARGE169* target segment elements. Modeling of target

surface in flexible – rigid contacts is quite simpleforward as elements will not overlay and intertwine with solid finite elements, complex rigid target surfaces can be modeled. In general contact type, contact surfaces are generated automatically by an embedded sub – routine, which scans interacting geometric shapes and physical parts in the model. Unline pair – based contact type, 2 – D target segment elements and 2 – D contact line elements are not associated with these interaction properties, material parameters, and friction related terms. Therefore, there is no real constant set sharing. Furthermore, some important necessities and restrictions for this element regarding contact mechanics are presented below:

- *TARGE169* target segment elements must be defined in global workspace.
- For parabolic segment elements, third target point must lie at the middle of the parabola.
- Linear pertubation is not supported.
- Monitoring contact birth and death is not supported.

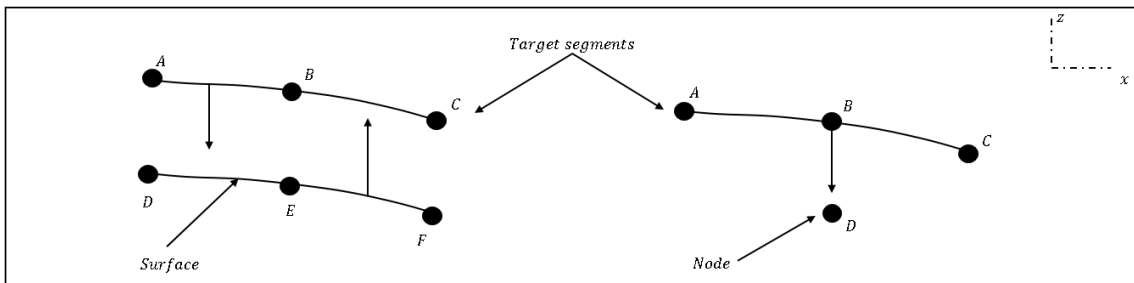


Fig. 9. Element geometries of *TARGE169* target segment elements

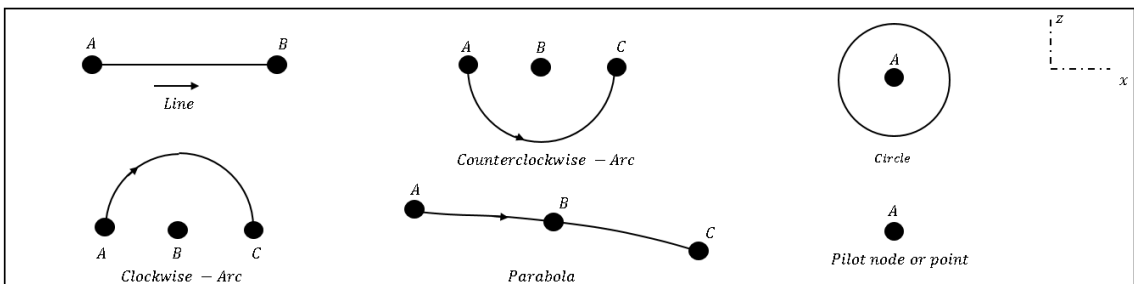


Fig. 10. Segment element types of *TARGE169* target segment elements

To represent sliding contact behavior between 8 – noded quadrilateral *PLANE183* solid finite elements and *TARGE169* target segment elements, *CONTA172* contact line elements are utilized (see Fig. 11 for element geometry). This element type is well applicable to 2 – D structural and coupled – field contact analyses, where it can be utilized for both pair – based and general contact types. Coulomb and shear stress friction models can be implemented for both flexible – flexible and rigid – flexible contacts. It also allows dissociation of flexible surfaces, where interface delamination of layered structures and laminated composites can be examined. Moreover, some important necessities and restrictions for this element regarding contact mechanics are presented below:

- *CONTA172* contact line elements must be defined in global workspace.
- To utilize symmetry conditions, vertical axis must be the axis of symmetry.
- Utilization with axisymmetric harmonic elements is not supported.
- It can also be utilized with *TARGE170* target segment elements to define 3 – D pair – based and general contacts.
- User – defined contact is not supported.
- Monitoring contact birth and death is not supported.

Note that, additional information for finite element types and their utilization in ANSYS Mechanical APDL R2020 can be found in [78 – 80].

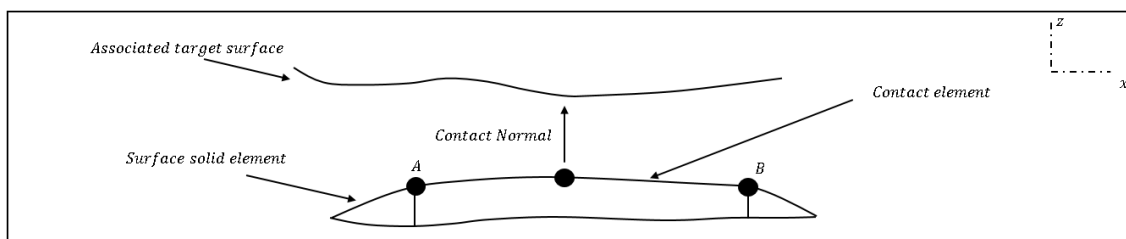


Fig. 11. Element geometry of *CONTA172* contact line element

### 3.3.2. Augmented contact formulation (ACF)

To model dis – continuities resulting from interaction properties, material parameters, and friction related terms, an augmented contact formulation (ACF) based on Lagrange multiplier and penalty methods is utilized in ANSYS



Mechanical APDL R2020. The aim is to increase contact accuracy by capturing strong and weak spots, as they create numerical ill – continuities at the surface of laminated glass fiber composite. In augmented contact formulation (ACF), governing non – linear contact equations consist of two different sets; a set without numerical ill – continuities and a set with numerical ill – continuities associated to dis – continuities. Solutions can be obtained by resolving non – linear equations with residual controlled iterative algorithms, such as Newton – Raphson and bisection methods. To model contact behavior between laminae, bonded contacts are utilized, as no separation or interlaminar debonding are wanted [81 – 83].

### **3.3.3. Preperation of the model, adaptive mesh refinement, and solution details**

Prepared finite element model and deformed shape of laminated glass fiber composite are presented in Fig. 12, wherein plane strain conditions are applied. Parametric benchmarks are created by diversifying interaction properties, material parameters, friction related terms, and lamina order. Regardless of lamina order and post – processing path, 378383 total number of 8 – noded quadrilateral *PLANE183* solid finite elements are utilized along with 2 *TARGE169* target segment elements, and 2326 *CONTA172* contact line elements. To improve solution efficiency without decreasing accuracy, an adaptive mesh – refinement sub – routine is prepared. Element size is automatically adjusted by comparing approximate absolute error between surface contact and in – plane stress distributions peaks at  $x=0.0$  and  $z=0.0$ , edges of the contact patch, and sub – surface center – line in –plane stress distributions peaks at  $x=0.0$  and  $z=-1.125mm$  in each iteration. In transition regions, 8 – noded quadrilateral *PLANE183* solid finite elements are connected using 6 – noded ones. For the element behavior and element formulation, plane strain conditions and pure displacement element formulation are utilized, respectively. To hinder rotation and translation of rigid cylinder through  $-z$  and  $-x$  global directions, pilot node for *TARGE169* target segment elements is restricted. Identically, the bottom surface of the laminated glass fiber composite

is fixed, where all rotations and translations are restricted  $-x$ ,  $-y$ , and  $-z$  global directions. To further increase the understanding, solution details are shown in Fig. 13 in an iterative scheme.

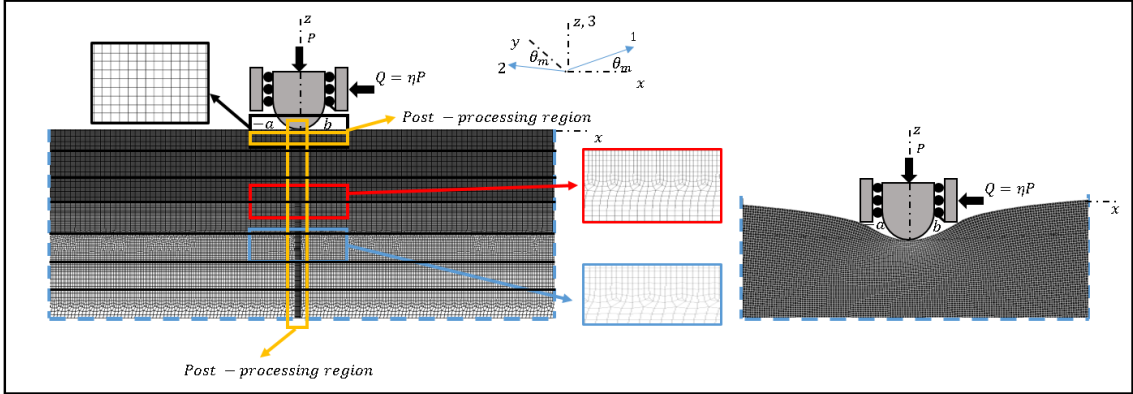


Fig. 12. Finite element model and deformed shape of laminated glass fiber composite

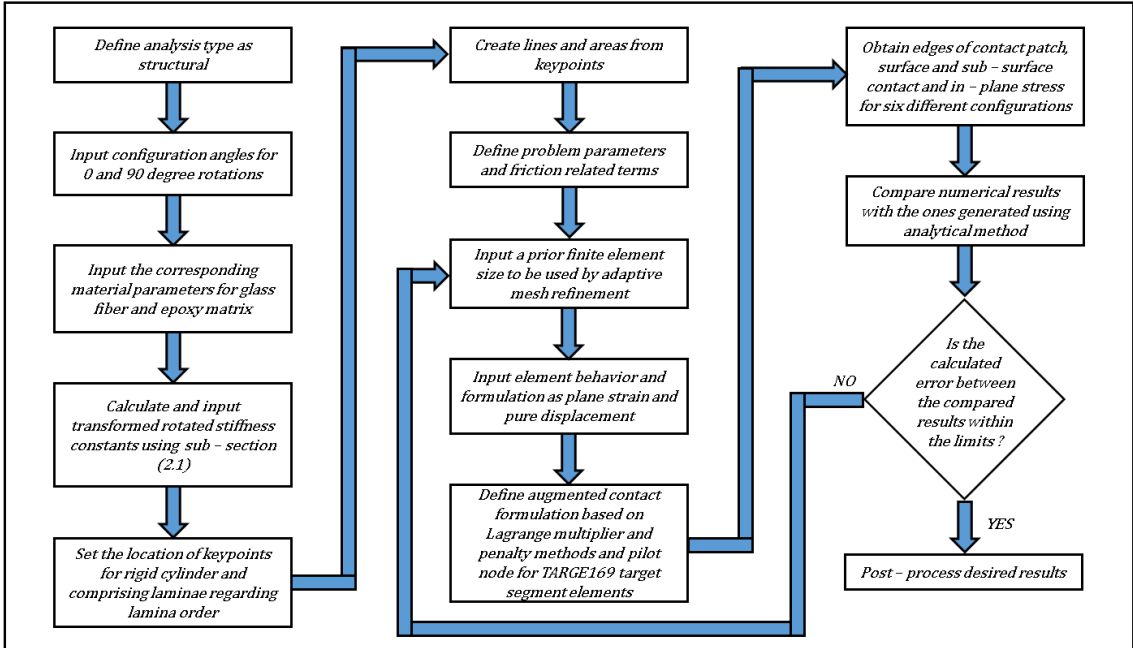


Fig. 13. Iterative scheme

**3.3.4. Accuracy of adaptive mesh refinement and solution times**

To increase accuracy for results on post – processing regions, a prior mesh sensitivity analysis is conducted. Using coarser finite elements away from regions

of interest provided an extensive decrease on solution time without compromising solution accuracy. Numerical validation is performed for  $[90_3/0_3]_s$  configuration, where approximate absolute error comparison between surface contact and in – plane stress distributions peaks at  $x=0.0$  and  $z=0.0$ , edges of the contact patch, and sub – surface center – line in –plane stress distributions peaks at  $x=0.0$  and  $z=-1.125mm$  are presented in Tables 2 – 4 for increasing number of finite elements in each iteration.

Table 2. Accuracy of adaptive mesh refinement – 1

$R=100mm, P=100N/mm, \eta=0.4, V_f=\%40, h_t=4.5mm, h=0.375mm,$ $W=90mm, m=12$					
# of iteratio n	# of element s	$\sigma_{1,zz}(0,0)$ (MPa)	$\sigma_{1,xx}(0,0)$ (MPa)	$ \varepsilon_a $ (%), $\sigma_{1,zz}(0,0)$ (MPa)	$ \varepsilon_a $ (%), $\sigma_{1,xx}(0,0)$ (MPa)
1	436	-17.64	-22.93	100.0	100.0
2	2874	-24.32	-32.11	27.5	28.6
3	25889	-34.55	-38.97	29.5	17.4
4	53245	-46.61	-51.42	25.9	24.3
5	99522	-57.29	-59.41	18.5	13.6
6	256152	-64.82	-62.76	11.7	5.2
7	378383	-65.71	-63.33	1.3	0.9

After numerical models are prepared in ANSYS Mechanical APDL R2020, computational solutions are obtained using a simulation environment with a 16 core, 32 thread CPU running at 4.5GHz base speed and 64GB of RAM. Each parametric solution takes less than 450 seconds to compute owing to adaptive mesh refinement.

Table 3. Accuracy of adaptive mesh refinement – 2

$$R = 100\text{mm}, P = 100\text{N/mm}, \eta = 0.4, V_f = \%40, h_t = 4.5\text{mm}, h = 0.375\text{mm},$$

$$W = 90\text{mm}, m = 12$$

# of iteration	# of elements	$-a$ (mm)	$b$ (mm)	$ \varepsilon_a $ (%), $-a$ (mm)	$ \varepsilon_a $ (%), $b$ (mm)
1	436	-1.348	1.622	100.0	100.0
2	2874	-1.152	1.496	17.0	9.2
3	25889	-0.994	1.358	15.8	8.7
4	53245	-0.926	1.239	7.3	7.7
5	99522	-0.893	1.143	3.6	5.7
6	256152	-0.871	1.081	2.5	9.4
7	378383	-0.865	1.068	0.6	1.2

Table 4. Accuracy of adaptive mesh refinement – 3

$$R = 100\text{mm}, P = 100\text{N/mm}, \eta = 0.4, V_f = \%40, h_t = 4.5\text{mm}, h = 0.375\text{mm},$$

$$W = 90\text{mm}, m = 12$$

# of iteration	# of elements	$\sigma_{3,xx}$ (0, -1.125) (MPa)	$\sigma_{4,xx}$ (0, -1.125) (MPa)	$ \varepsilon_a $ (%), $\sigma_{3,xx}$ (0, -1.125) (MPa)	$ \varepsilon_a $ (%), $\sigma_{4,xx}$ (0, -1.125) (MPa)
1	436	-3.56	-0.77	100.0	100.0
2	2874	-7.24	-0.92	50.8	16.3
3	25889	-9.12	-1.04	20.6	11.5
4	53245	-10.11	-1.15	9.7	9.5
5	99522	-10.87	-1.21	6.9	4.9
6	256152	-11.34	-1.24	4.1	2.4
7	378383	-11.46	-1.26	1.0	1.5

## 4. RESULTS AND DISCUSSION

In this section, the study findings are presented. By diversifying interaction properties, material parameters, friction related terms, and lamina order, the results of analytical and finite element methods are contrasted. The compared results are surface contact and in – plane stress distributions, edges of the contact patch, sub – surface center – line in –plane stress distributions, and sub – surface in – plane stress contours. It can be noted that, results from both methods are matched perfectly. Following limits,  $50N/mm \leq P \leq 200N/mm$  ,  $0.0 \leq \eta \leq 0.8$  ,  $100mm \leq R \leq 200mm$  , and  $\%40 \leq V_f \leq \%60$  and six different configurations for lamina order  $[0_{12}]$ ,  $[90_{12}]$ ,  $[0_3/90_3]_s$ ,  $[90_3/0_3]_s$ ,  $[0_3/90_3]_2$ , and  $[90_3/0_3]_2$  are utilized to post – process results. Firstly, the effects of interaction properties, material parameters, and friction related terms on surface contact and in – plane stress distributions and edges of contact patch are investigated in sub – section (4.1), where comparisons are described in Figs. 14 – 25 and Tables 5 – 28, respectively. Comparisons are then shown in Figs. 26 – 27 for surface contact and in – plane stress and sub – surface center – line in – plane stress distributions for six different configurations for lamina order in sub – section (4.2). After that, in sub – section (4.3), comparisons for sub – surface in – plane stress contours for six different configurations for lamina order are given using analytical and finite element methods, where Figs. 28 – 29 have been added.

### 4.1. Effects of interaction properties, material parameters, and friction related terms on surface contact and in – plane stress distributions

Comparison of surface contact and in – plane stress distributions and edges of contact patch for unidirectional configurations  $[0_{12}]$  and  $[90_{12}]$  are given in Figs. 14 – 17 and Tables 5 – 12. Effect of concentrated normal force  $P$  on surface contact and in – plane stress distributions and edges of contact patch is presented in Fig. 14, where the remainder interaction properties and friction related terms are taken as  $R=100mm$  ,  $\eta=0.4$  ,  $V_f=\%40$  ,  $h_t=4.5mm$  ,  $h=0.375mm$  ,  $W=90mm$  ,  $m=12$  . Increase in concentrated normal force  $P$

causes the rigid cylinder to penetrate deeper into the surface of laminated glass fiber composite. Thus, resulting compressive and tensional peaks on surface contact and in – plane stress distributions are greatly increased and contact patch is widened (see Table 5 and Table 6 for the edges of contact patch). For higher values of  $P$ , successful monitoring of these peaks in surface contact and in – plane stress distributions is very important as high peaks may cause unpredictable and instant micro cracks at the surface of laminated glass fiber composite. In industrial applications where the product is used as a coating or a mechanical barrier, micro cracks may adversely affect surface performance. To prevent these local failures, surface optimization can be conducted with respect to concentrated normal force  $P$ .

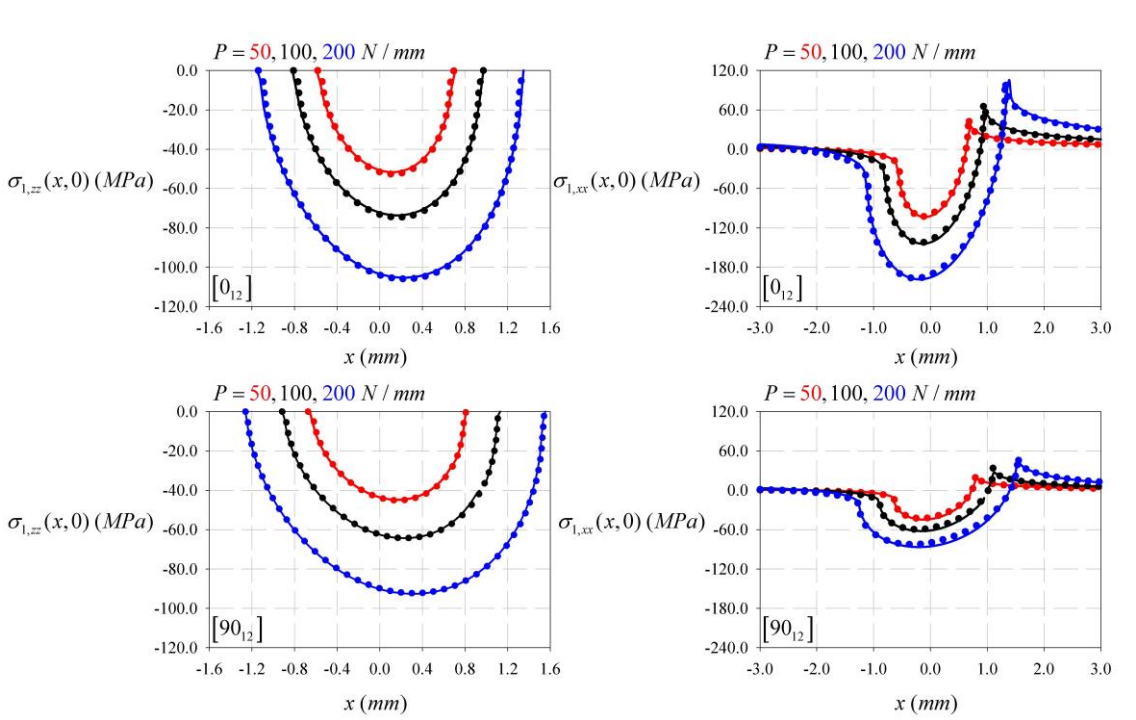


Fig. 14. Comparison of surface contact and in – plane stress distribution for  $R=100mm$ ,  $\eta=0.4$ ,  $V_f = \%40$ ,  $h_t = 4.5mm$ ,  $h=0.375mm$ ,  $W=90mm$ ,  $m=12$ , solid lines represent finite element method, dotted lines represent analytical method

In Fig. 15, effect of Coulomb’s static coefficient of friction  $\eta$  on surface contact and in – plane stress distributions and edges of contact patch is illustrated. Unrelated interaction properties are taken as  $R=100mm$ ,  $P=100N/mm$ ,

$V_f = \%40$ ,  $h_t = 4.5mm$ ,  $h = 0.375mm$ ,  $W = 90mm$ ,  $m = 12$ . Increase in  $\eta$  slanted surface contact stress distributions to leading edge of the contact patch (see Table 7 and Table 8 for the variation of  $-a$  and  $b$  for varying values of Coulomb's static coefficient of friction  $\eta$ ). Resulting compressive peaks are not affected because there is no relation between concentrated normal force  $P$  and Coulomb's static coefficient of friction  $\eta$ . On the other hand, increase in  $\eta$  drastically affected resulting peaks on surface in  $-$  plane stress distributions (see the connection between  $\eta$  and  $Q = \eta P$ ). Monitoring these tensional peaks is crucial in designing strong wear resistant surfaces. The tensile peaks on the surface can be minimized by using surface lubricants, hard interlaminar layers, and applying a homogeneous distribution to individual glass fiber and epoxy matrix material parameters. Surface wear will therefore decrease.

Table 5. Edges of contact patch for unidirectional configuration  $[0_{12}]$  for varying  $P$

$R = 100mm$ , $\eta = 0.4$ , $V_f = \%40$ , $h_t = 4.5mm$ , $h = 0.375mm$ , $W = 90mm$ , $m = 12$						
Concentrated normal force $P$  ( $N/mm$ )	Analytical method		FEM		$ \varepsilon_t $ (%), $-a$  ( $mm$ )	$ \varepsilon_t $ (%), $b$  ( $mm$ )
	$-a$	$b$	$-a$	$b$		
	( $mm$ )	( $mm$ )	( $mm$ )	( $mm$ )		
50	-0.584	0.694	-0.596	0.708	2.0	2.0
100	-0.812	0.972	-0.824	0.976	1.4	0.4
200	-1.142	1.342	-1.156	1.352	1.2	0.7

Table 6. Edges of contact patch for unidirectional configuration  $[90_{12}]$  for varying  $P$

Concentrated normal force $P$  ( $N/mm$ )	Analytical method		FEM		$ \varepsilon_t $ (%), $-a$	$ \varepsilon_t $ (%), $b$
	$-a$	$b$	$-a$	$b$	( $mm$ )	( $mm$ )
	( $mm$ )	( $mm$ )	( $mm$ )	( $mm$ )		
50	-0.674	0.808	-0.660	0.812	2.1	0.4
100	-0.918	1.112	-0.924	1.132	0.6	1.7
200	-1.262	1.544	-1.276	1.556	1.0	0.7

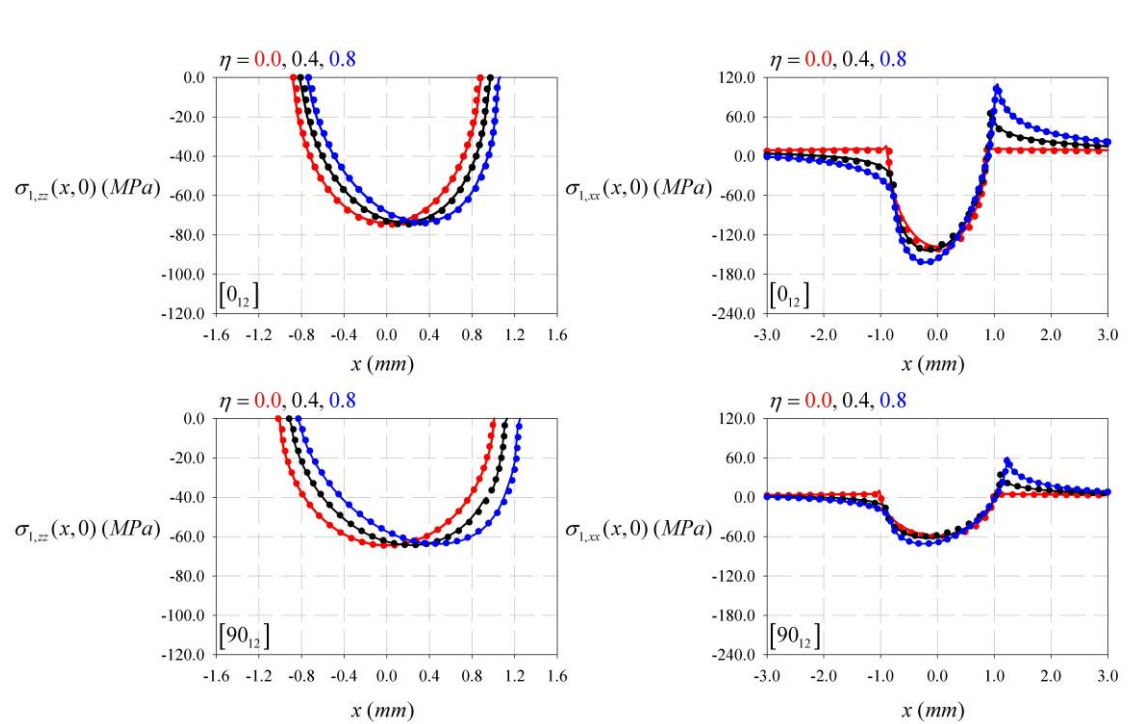


Fig. 15. Comparison of surface contact and in – plane stress distribution for  $R=100mm$ ,  $P=100N/mm$ ,  $V_f = \%40$ ,  $h_t = 4.5mm$ ,  $h = 0.375mm$ ,  $W = 90mm$ ,  $m = 12$ , solid lines represent finite element method, dotted lines represent analytical method



Table 7. Edges of contact patch for unidirectional configuration  $[0_{12}]$  for varying  $\eta$

$R = 100mm, P = 100N/mm, V_f = \%40, h_t = 4.5mm, h = 0.375mm, W = 90mm,$						
$m = 12$						
Coulomb's static coefficient of friction $\eta$	Analytical method		FEM		$ \varepsilon_t (\%), -a$	$ \varepsilon_t (\%), b$
	$-a$	$b$	$-a$	$b$	(mm)	(mm)
	(mm)	(mm)	(mm)	(mm)		
0.0	-0.878	0.878	-0.888	0.888	1.1	1.1
0.4	-0.812	0.972	-0.824	0.976	1.4	0.4
0.8	-0.736	1.048	-0.748	1.064	1.6	1.5

Table 8. Edges of contact patch for unidirectional configuration  $[90_{12}]$  for varying  $\eta$

$R = 100mm, P = 100N/mm, V_f = \%40, h_t = 4.5mm, h = 0.375mm, W = 90mm,$						
$m = 12$						
Coulomb's static coefficient of friction $\eta$	Analytical method		FEM		$ \varepsilon_t (\%), -a$	$ \varepsilon_t (\%), b$
	$-a$	$b$	$-a$	$b$	(mm)	(mm)
	(mm)	(mm)	(mm)	(mm)		
0.0	-1.020	1.020	-1.008	1.008	1.1	1.1
0.4	-0.918	1.112	-0.924	1.132	0.6	1.7
0.8	-0.832	1.250	-0.840	1.252	0.9	0.1

Effect of rigid cylinder radius  $R$  on on surface contact and in – plane stress distributions and edges of contact patch is shown in Fig. 16, where  $\eta = 0.4$ ,  $P = 100N/mm, V_f = \%40, h_t = 4.5mm, h = 0.375mm, W = 90mm, m = 12$ . For high values of  $R$ , resulting surface contact and in – plane stress distributions peaks

are decreased and contact patch is increased (see Table 9 and Table 10). Thus, a more equal stress distribution is monitored. If an application requires the use of lower values of  $R$  for rigid cylinder, proper surface lubrication may be needed to reduce the surface wear. Lower values of  $R$  may cause surface contact and in – plane stress distributions to concentrate at one point.

In Fig. 17, effect of glass fiber volume fraction  $V_f$  on surface contact and in – plane stress distributions and edges of contact patch is given, where  $\eta = 0.4$ ,  $P = 100N/mm$ ,  $R = 100mm$ ,  $h_t = 4.5mm$ ,  $h = 0.375mm$ ,  $W = 90mm$ ,  $m = 12$ . In engineering applications, the highest achievable fiber volume fraction  $V_f$  is around %70 due to manufacturing processes. Adding too much fiber volume may decrease the strength of laminated glass fiber composite as there will be no space for the epoxy matrix components to bond with fibers, choosing an optimal value for fiber volume fraction  $V_f$  is very important. Therefore, %40, %50, and %60 fiber volume fraction  $V_f$  are chosen for parametric studies. For higher values of  $V_f$ , laminated glass fiber composite became more stiff in loading directions. Therefore, higher compressive and tensional peaks are observed. This stiff behavior has a potential to lead unpredictable and instant micro cracks at the surface of laminated glass fiber composite, which may instantly reduce surface performance. To observe the variation on edges of contact patch for unidirectional configurations  $[0_{12}]$  and  $[90_{12}]$ , see Table 11 and Table 12, respectively.

In Figs. 18 – 25 and Tables 13 – 28, comparison of surface contact and in – plane stress distributions and edges of contact patch for configurations  $[0_3/90_3]_s$ ,  $[90_3/0_3]_s$ ,  $[0_3/90_3]_2$ , and  $[90_3/0_3]_2$  are presented. Explanations related to surface contact and in – plane stress distributions and edges of contact patch for unidirectional configurations  $[0_{12}]$  and  $[90_{12}]$  are also valid for configurations  $[0_3/90_3]_s$ ,  $[90_3/0_3]_s$ ,  $[0_3/90_3]_2$ , and  $[90_3/0_3]_2$ . One of the interesting observations that differed from unidirectional configurations  $[0_{12}]$  and  $[90_{12}]$  is that the compressive and tensional peaks in surface contact and in – plane stress distributions decreased for configurations started with 0 degree rotation and

increased for configurations started with 90 degree, respectively. Lamina order affected total stiffness of laminated glass fiber composite in normal and horizontal loading directions. Furthermore, surface contact and in – plane stress distributions shifted to leading edge of contact patch more specifically.

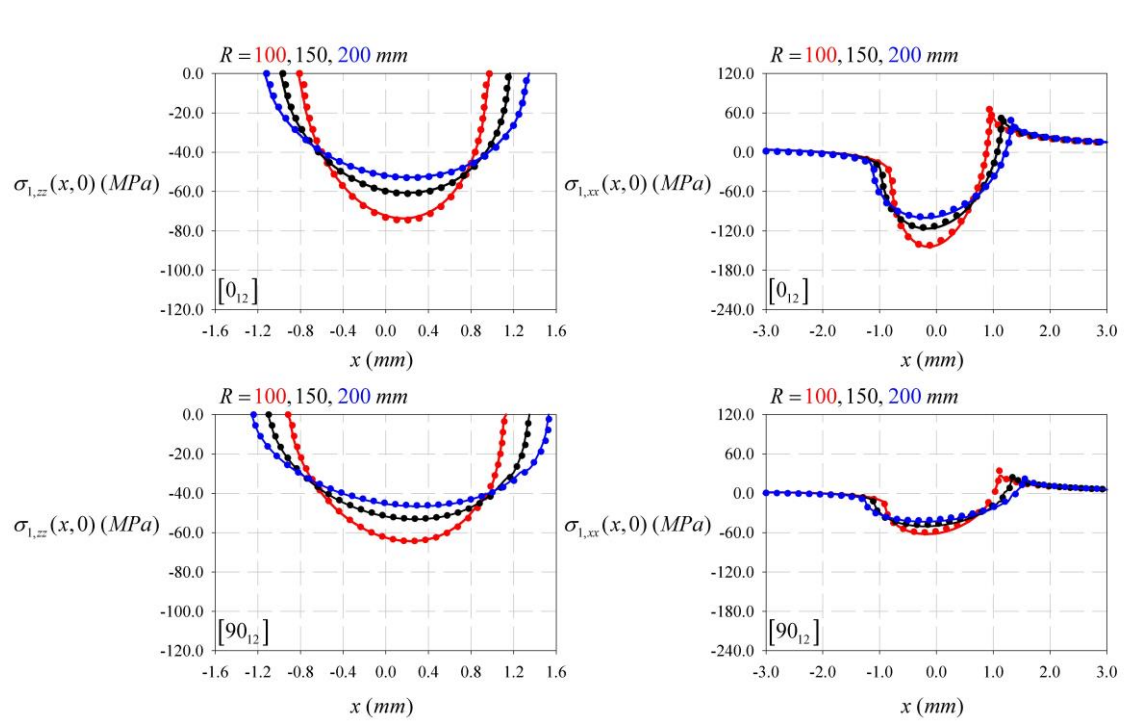


Fig. 16. Comparison of surface contact and in – plane stress distribution for  $\eta = 0.4$ ,  $P = 100N / mm$ ,  $V_f = \%40$ ,  $h_t = 4.5mm$ ,  $h = 0.375mm$ ,  $W = 90mm$ ,  $m = 12$ , solid lines represent finite element method, dotted lines represent analytical method

Table 9. Edges of contact patch for unidirectional configuration  $[0_{12}]$  for varying  $R$

$$\eta = 0.4, P = 100N/mm, V_f = \%40, h_t = 4.5mm, h = 0.375mm, W = 90mm,$$

$$m = 12$$

Rigid cylinder radius $R$ (mm)	Analytical method		FEM		$ \varepsilon_t $ (%), $-a$ (mm)	$ \varepsilon_t $ (%), $b$ (mm)
	$-a$	$b$	$-a$	$b$		
	(mm)	(mm)	(mm)	(mm)		
100	-0.812	0.972	-0.824	0.976	1.4	0.4
150	-0.968	1.154	-0.988	1.168	2.0	1.1
200	-1.121	1.339	-1.140	1.348	1.7	0.6

Table 10. Edges of contact patch for unidirectional configuration  $[90_{12}]$  for varying  $R$

$$\eta = 0.4, P = 100N/mm, V_f = \%40, h_t = 4.5mm, h = 0.375mm, W = 90mm,$$

$$m = 12$$

Rigid cylinder radius $R$ (mm)	Analytical method		FEM		$ \varepsilon_t $ (%), $-a$ (mm)	$ \varepsilon_t $ (%), $b$ (mm)
	$-a$	$b$	$-a$	$b$		
	(mm)	(mm)	(mm)	(mm)		
100	-0.918	1.112	-0.924	1.132	0.6	1.7
150	-1.100	1.339	-1.100	1.339	0.7	0.6
200	-1.242	1.530	-1.242	1.530	1.4	0.1

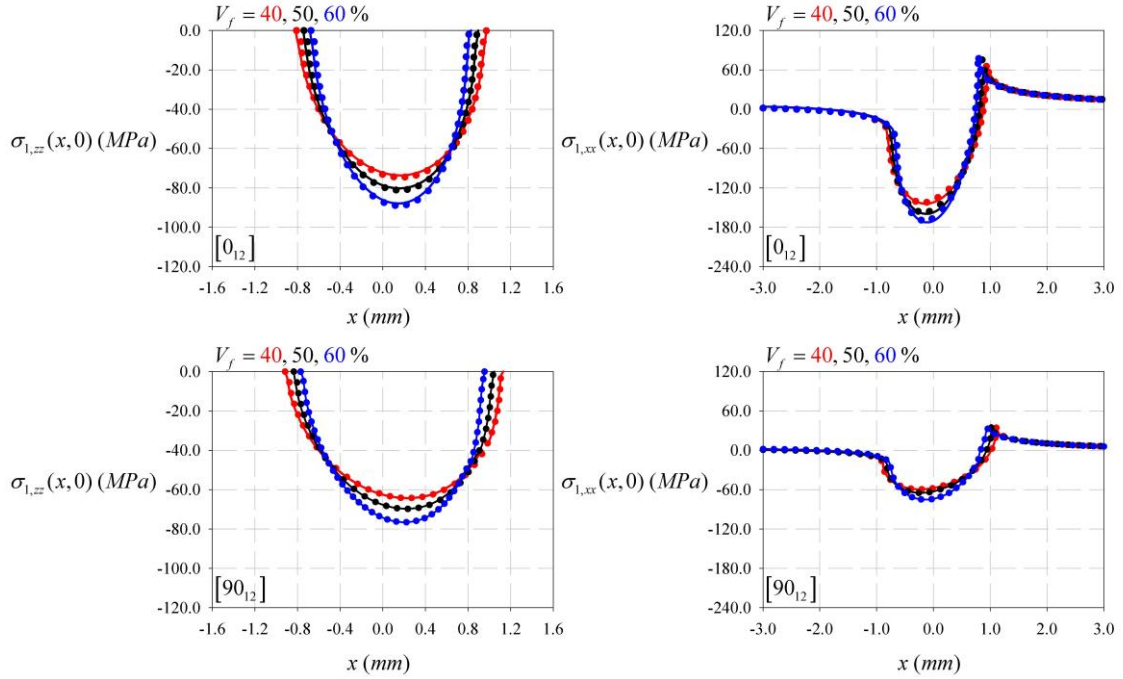


Fig. 17. Comparison of surface contact and in – plane stress distribution for  $\eta = 0.4$ ,  $P = 100N/mm$ ,  $R = 100mm$ ,  $h_t = 4.5mm$ ,  $h = 0.375mm$ ,  $W = 90mm$ ,  $m = 12$ , solid lines represent finite element method, dotted lines represent analytical method

Table 11. Edges of contact patch for unidirectional configuration  $[90_{12}]$  for varying  $V_f$

$\eta = 0.4$ , $P = 100N/mm$ , $R = 100mm$ , $h_t = 4.5mm$ , $h = 0.375mm$ , $W = 90mm$ , $m = 12$						
Fiber volume fraction $V_f$ (%)	Analytical method		FEM		$ \varepsilon_t $ (%), $-a$	$ \varepsilon_t $ (%), $b$
	$-a$ (mm)	$b$ (mm)	$-a$ (mm)	$b$ (mm)	(mm)	(mm)
40	-0.812	0.972	-0.824	0.976	1.4	0.4
50	-0.742	0.889	-0.752	0.896	1.3	0.7
60	-0.675	0.812	-0.688	0.832	1.8	2.4

Table 12. Edges of contact patch for unidirectional configuration  $[90_{12}]$  for varying  $V_f$

$\eta = 0.4, P = 100N/mm, R = 100mm, h_t = 4.5mm, h = 0.375mm, W = 90mm,$						
$m = 12$						
Fiber volume fraction $V_f$ (%)	Analytical method		FEM		$ \varepsilon_t $ (%), $-a$ (mm)	$ \varepsilon_t $ (%), $b$ (mm)
	$-a$	$b$	$-a$	$b$		
	(mm)	(mm)	(mm)	(mm)		
40	-0.918	1.112	-0.924	1.132	0.6	1.7
50	-0.836	1.038	-0.840	1.048	0.4	0.9
60	-0.764	0.948	-0.772	0.956	1.0	0.8

#### 4.2. Effects of lamina order on surface contact and in – plane stress and sub – surface center – line in – plane stress distributions

Effects of lamina order on surface contact and in – plane stress and sub – surface center – line in – plane stress distributions and comparisons for six different configurations for lamina order are illustrated in this sub – section, in which Figs. 26 – 27 present the relevant details. Following generalization can be made for surface contact and in – plane stress distributions for six different configurations for lamina order  $[0_{12}]$ ,  $[90_{12}]$ ,  $[0_3/90_3]_s$ ,  $[90_3/0_3]_s$ ,  $[0_3/90_3]_2$ , and  $[90_3/0_3]_2$ : configuration started with 0 degree rotation resulted in higher compressive and tensional peaks as 90 degree rotation resulted in a softer behavior in normal loading direction than 0 degree. Seen from Fig. 26,  $[90_{12}]$  configuration is softer than  $[0_{12}]$  in normal loading direction. Therefore, lower compressive and tensional peaks are monitored. Due to this soft behavior and smooth penetration on the surface, a wider contact patch is observed. On the other hand, no considerable variation is observed on surface contact stress distributions between  $[0_3/90_3]_s$ ,  $[90_3/0_3]_s$ ,  $[0_3/90_3]_2$ , and  $[90_3/0_3]_2$  configurations as they demonstrated near identical stiffness behavior in normal loading direction, where

the laminae except the one in contact contributed to overall stiffness. Furthermore, a remarkable variation in horizontal direction of loading is then observed for surface in – plane stress distributions. Since the surface stiffness of laminated glass fiber composites started with 90 degree rotation is much lower than 0 degree rotation, surface in – plane stresses are more uniformly spread across the contact patch and lower tensional peaks are found. Even so, changes on edges of contact patch are negligible for these configurations.

Considering lamina order, the stiffness in normal and horizontal loading directions varies between configurations. For each laminated glass fiber composite, this can cause sub – surface center – line in – plane stress distributions to be different (see Fig. 27). In unidirectional configurations  $[0_{12}]$  and  $[90_{12}]$ , total stiffness along normal and horizontal loading directions is constant and  $[0_{12}]$  configuration is properly stiffer than the opposite one in both loading directions. Thus, on the surface, higher compressive peaks are found for center – line in – plane stress distributions. Therefore, away from surface, stress values are decreased faster than those in the configuration of  $[90_{12}]$ . Stiffer behavior lead to stresses that concentrate on the surface rather than extending to the sub – surface of the laminated glass fiber composite.

For  $[0_3/90_3]_s$  and  $[90_3/0_3]_s$  configurations, contact effect is diminished specially after the mid – plane where  $y = -2.250mm$ , as sub – surface center – line in – plane stress values are demonstrated a very close behavior for varying values of concentrated normal force  $P$ . However, at  $y = -1.125mm$ , a substantial difference is observed at the area of lamina angle shift. The sub – surface center – line in – plane stresses for the configuration of  $[90_3/0_3]_s$  changed in first three laminae in a broader stress band relative to  $[0_3/90_3]_s$ . This showed that first three laminae of 90 degree rotation served as a cushion and the next six laminae of 0 degree rotation transmitted a decreased load. For  $[0_3/90_3]_s$  configuration, owing to high stiffness, almost the entire loading is focused on the contact patch. At the lamina angle shift area, high compressive and tensional peaks are observed where  $y = -1.125mm$ . Proper analysis of these peaks is very important

to prevent interface cracks and interlaminar debonding. Behavior of  $[0_3/90_3]_2$  and  $[90_3/0_3]_2$  are similar to  $[0_3/90_3]_s$  and  $[90_3/0_3]_s$  configurations. Therefore, identical expressions can be made. In comparison, an improved compressive and tensile stress peak region is tracked at  $y = -2.250mm$  for the  $[0_3/90_3]_s$  configuration. Compared to  $[0_3/90_3]_s$ , the explanation for this discrepancy is that the three 90 degree rotation laminae are unable to absorb the stresses and thus the above peaks are found in the second lamina angle shift area. Furthermore, less compressive and tensile peaks are found for the  $[90_3/0_3]_2$  configuration as the first three 90 degree rotation laminae distributed stresses.

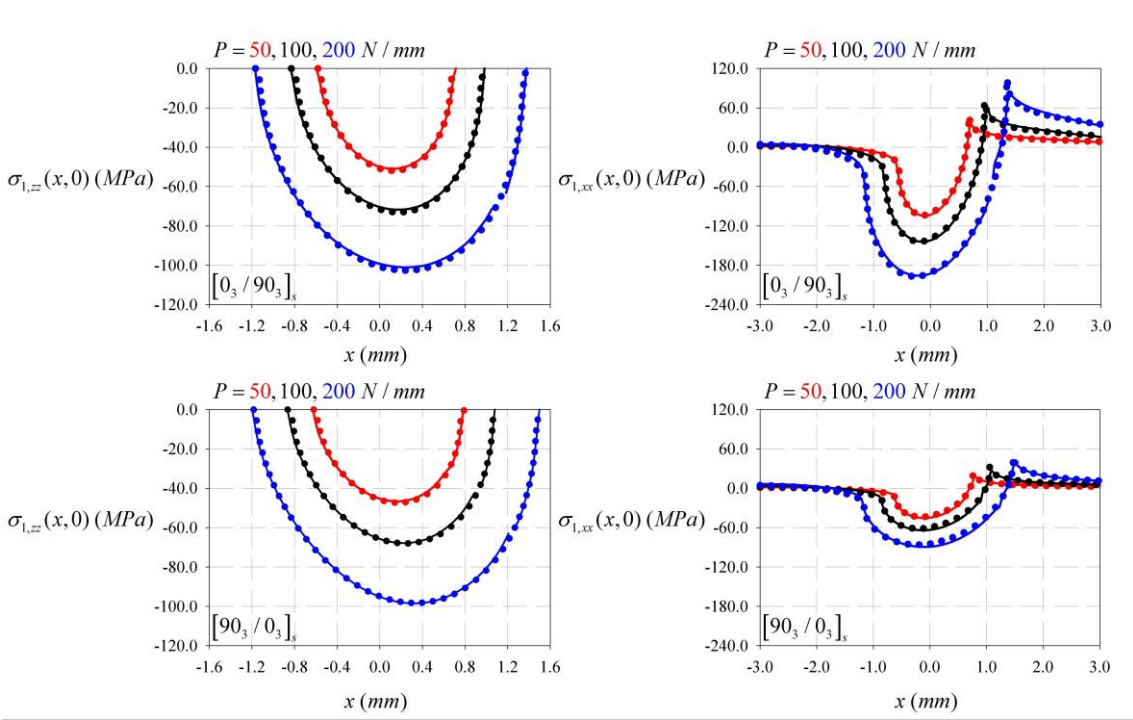


Fig. 18. Comparison of surface contact and in – plane stress distribution for  $R = 100mm$ ,  $\eta = 0.4$ ,  $V_f = \%40$ ,  $h_t = 4.5mm$ ,  $h = 0.375mm$ ,  $W = 90mm$ ,  $m = 12$ , solid lines represent finite element method, dotted lines represent analytical method



Table 13. Edges of contact patch for configuration  $[0_3/90_3]_s$  for varying  $P$

$R=100mm, \eta=0.4, V_f=\%40, h_t=4.5mm, h=0.375mm, W=90mm, m=12$

Concentrated normal force $P$  ( $N/mm$ )	Analytical method		FEM		$ \varepsilon_t $ (%), $-a$  ( $mm$ )	$ \varepsilon_t $ (%), $b$  ( $mm$ )
	$-a$	$b$	$-a$	$b$		
	( $mm$ )	( $mm$ )	( $mm$ )	( $mm$ )		
50	-0.582	0.704	-0.596	0.716	2.3	1.6
100	-0.832	0.974	-0.840	0.984	0.9	1.0
200	-1.168	1.372	-1.180	1.380	1.0	0.5

Table 14. Edges of contact patch for configuration  $[90_3/0_3]_s$  for varying  $P$

$R=100mm, \eta=0.4, V_f=\%40, h_t=4.5mm, h=0.375mm, W=90mm, m=12$

Concentrated normal force $P$  ( $N/mm$ )	Analytical method		FEM		$ \varepsilon_t $ (%), $-a$  ( $mm$ )	$ \varepsilon_t $ (%), $b$  ( $mm$ )
	$-a$	$b$	$-a$	$b$		
	( $mm$ )	( $mm$ )	( $mm$ )	( $mm$ )		
50	-0.621	0.792	-0.632	0.800	1.7	1.0
100	-0.865	1.068	-0.872	1.080	0.7	1.1
200	-1.185	1.494	-1.200	1.500	1.2	0.4

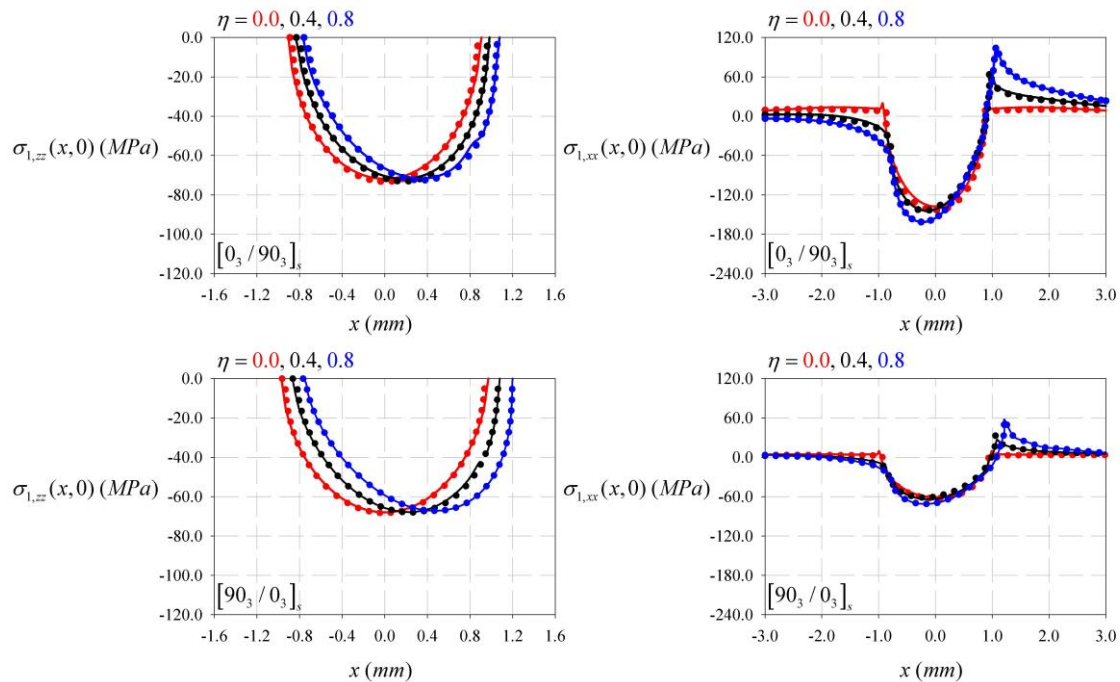


Fig. 19. Comparison of surface contact and in – plane stress distribution for  $R=100mm$ ,  $P=100N/mm$ ,  $V_f = \%40$ ,  $h_t = 4.5mm$ ,  $h = 0.375mm$ ,  $W = 90mm$ ,  $m = 12$ , solid lines represent finite element method, dotted lines represent analytical method

Table 15. Edges of contact patch for configuration  $[0_3/90_3]_s$  for varying  $\eta$

$R=100mm$ ,  $P=100N/mm$ ,  $V_f = \%40$ ,  $h_t = 4.5mm$ ,  $h = 0.375mm$ ,  $W = 90mm$ ,  
 $m = 12$

Coulomb's static coefficient of friction $\eta$	Analytical method		FEM		$ \varepsilon_t $ (%), $-a$ (mm)	$ \varepsilon_t $ (%), $b$ (mm)
	$-a$	$b$	$-a$	$b$		
	(mm)	(mm)	(mm)	(mm)		
0.0	-0.892	0.892	-0.908	0.908	1.76	1.76
0.4	-0.832	0.974	-0.840	0.984	0.9	1.0
0.8	-0.760	1.080	-0.772	1.080	1.5	1.8

Table 16. Edges of contact patch for configuration  $[90_3/0_3]_s$  for varying  $\eta$

$R=100mm, P=100N/mm, V_f = \%40, h_t = 4.5mm, h = 0.375mm, W = 90mm,$   
 $m = 12$

Coulomb's static coefficient of friction $\eta$	Analytical method		FEM		$ \varepsilon_t (\%), -a$ (mm)	$ \varepsilon_t (\%), b$ (mm)
	$-a$	$b$	$-a$	$b$		
	(mm)	(mm)	(mm)	(mm)		
0.0	-0.966	0.966	-0.972	0.972	0.6	0.6
0.4	-0.865	1.068	-0.872	1.080	0.7	1.1
0.8	-0.768	1.198	-0.780	1.200	1.5	0.1

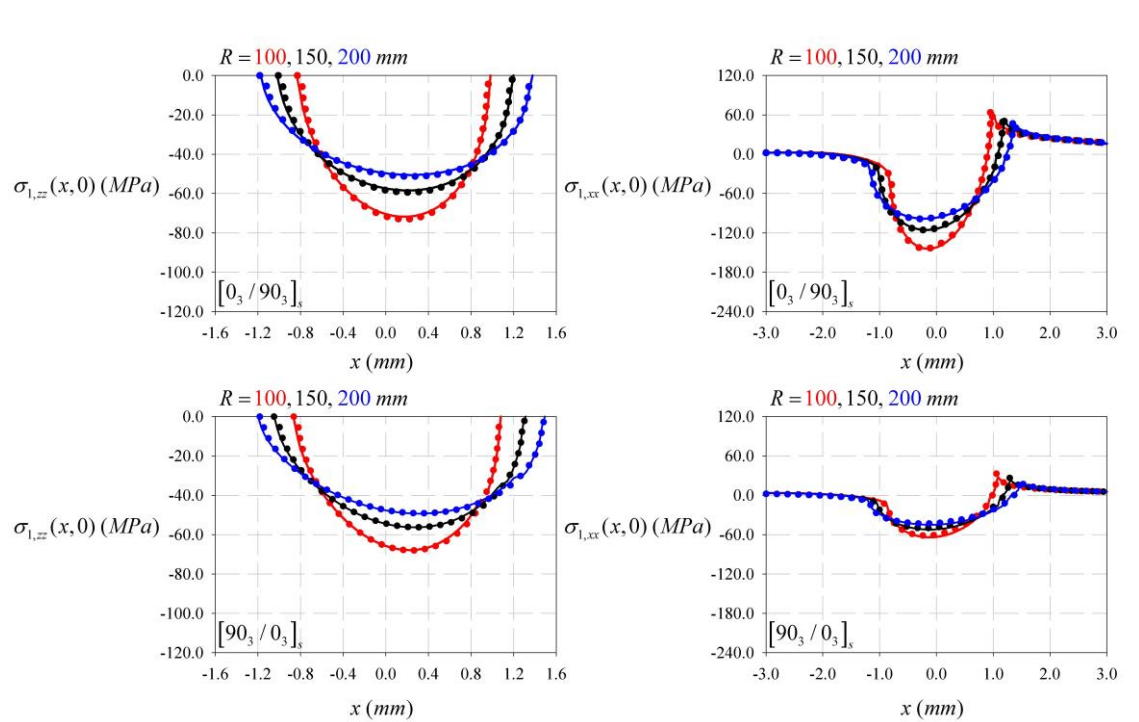


Fig. 20. Comparison of surface contact and in – plane stress distribution for  $\eta = 0.4, P = 100N/mm, V_f = \%40, h_t = 4.5mm, h = 0.375mm, W = 90mm, m = 12,$  solid lines represent finite element method, dotted lines represent analytical method

Table 17. Edges of contact patch for configuration  $[0_3/90_3]_s$  for varying  $R$

$\eta = 0.4, P = 100N/mm, V_f = \%40, h_t = 4.5mm, h = 0.375mm, W = 90mm,$   
 $m = 12$

Rigid cylinder radius $R$ (mm)	Analytical method		FEM		$ \varepsilon_t $ (%), $-a$ (mm)	$ \varepsilon_t $ (%), $b$ (mm)
	$-a$	$b$	$-a$	$b$		
	(mm)	(mm)	(mm)	(mm)		
100	-0.832	0.974	-0.840	0.984	0.9	1.0
150	-1.010	1.198	-1.028	1.200	1.7	0.1
200	-1.184	1.375	-1.192	1.380	0.6	0.3

Table 18. Edges of contact patch for configuration  $[90_3/0_3]_s$  for varying  $R$

$\eta = 0.4, P = 100N/mm, V_f = \%40, h_t = 4.5mm, h = 0.375mm, W = 90mm,$   
 $m = 12$

Rigid cylinder radius $R$ (mm)	Analytical method		FEM		$ \varepsilon_t $ (%), $-a$ (mm)	$ \varepsilon_t $ (%), $b$ (mm)
	$-a$	$b$	$-a$	$b$		
	(mm)	(mm)	(mm)	(mm)		
100	-0.865	1.068	-0.872	1.080	0.8	1.1
150	-1.050	1.311	-1.052	1.316	0.1	0.3
200	-1.184	1.494	-1.200	1.496	1.3	0.1

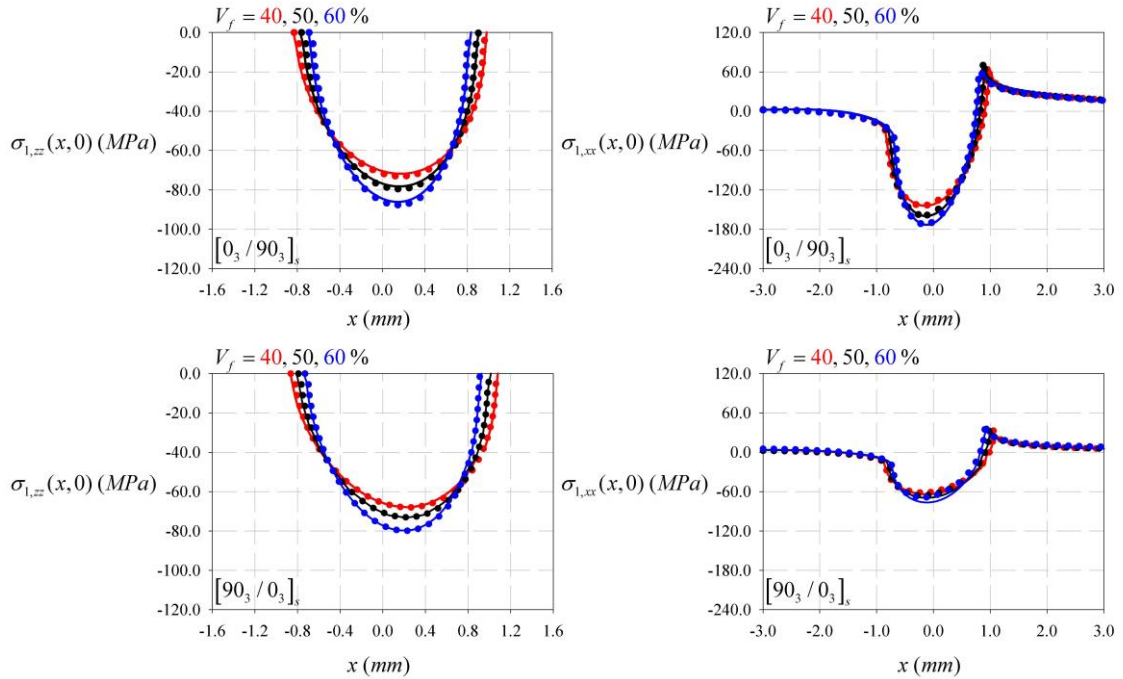


Fig. 21. Comparison of surface contact and in – plane stress distribution for  $\eta = 0.4$ ,  $P = 100N/mm$ ,  $R = 100mm$ ,  $h_t = 4.5mm$ ,  $h = 0.375mm$ ,  $W = 90mm$ ,  $m = 12$ , solid lines represent finite element method, dotted lines represent analytical method

Table 19. Edges of contact patch for configuration  $[0_3/90_3]_s$  for varying  $V_f$

$\eta = 0.4$ ,  $P = 100N/mm$ ,  $R = 100mm$ ,  $h_t = 4.5mm$ ,  $h = 0.375mm$ ,  $W = 90mm$ ,  
 $m = 12$

Fiber volume fraction $V_f$ (%)	Analytical method		FEM		$ \varepsilon_t $ (%), $-a$ (mm)	$ \varepsilon_t $ (%), $b$ (mm)
	$-a$	$b$	$-a$	$b$		
	(mm)	(mm)	(mm)	(mm)		
40	-0.832	0.974	-0.840	0.984	0.9	1.0
50	-0.762	0.905	-0.776	0.920	1.8	1.6
60	-0.690	0.825	-0.708	0.836	2.5	1.2

Table 20. Edges of contact patch for configuration  $[90_3/0_3]_s$  for varying  $V_f$

$\eta = 0.4, P = 100N/mm, R = 100mm, h_t = 4.5mm, h = 0.375mm, W = 90mm,$   
 $m = 12$

Fiber volume fraction $V_f$ (%)	Analytical method		FEM		$ \varepsilon_t $ (%), $-a$ (mm)	$ \varepsilon_t $ (%), $b$ (mm)
	$-a$	$b$	$-a$	$b$		
	(mm)	(mm)	(mm)	(mm)		
40	-0.865	1.068	-0.872	1.080	0.7	1.1
50	-0.793	1.005	-0.810	1.014	2.1	0.8
60	-0.732	0.912	-0.744	0.928	1.5	1.7

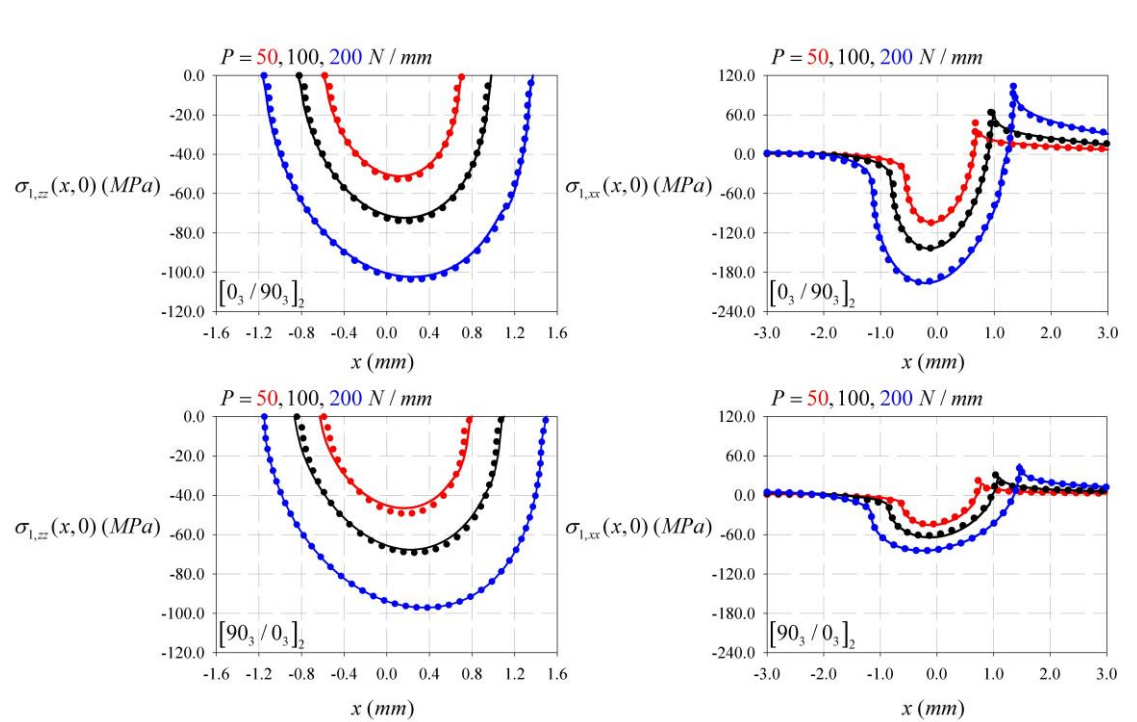


Fig. 22. Comparison of surface contact and in – plane stress distribution for  $R = 100mm, \eta = 0.4, V_f = \%40, h_t = 4.5mm, h = 0.375mm, W = 90mm, m = 12,$  solid lines represent finite element method, dotted lines represent analytical method

Table 21. Edges of contact patch for configuration  $[0_3/90_3]_2$  for varying  $P$

$R=100mm, \eta=0.4, V_f=\%40, h_t=4.5mm, h=0.375mm, W=90mm, m=12$

Concentrated normal force $P$  ( $N/mm$ )	Analytical method		FEM		$ \varepsilon_t $ (%), $-a$  ( $mm$ )	$ \varepsilon_t $ (%), $b$  ( $mm$ )
	$-a$	$b$	$-a$	$b$		
	( $mm$ )	( $mm$ )	( $mm$ )	( $mm$ )		
50	-0.584	0.708	-0.596	0.712	2.0	0.5
100	-0.824	0.972	-0.836	0.980	1.4	0.8
200	-1.154	1.368	-1.168	1.372	1.1	0.2

Table 22. Edges of contact patch for configuration  $[90_3/0_3]_2$  for varying  $P$

$R=100mm, \eta=0.4, V_f=\%40, h_t=4.5mm, h=0.375mm, W=90mm, m=12$

Concentrated normal force $P$  ( $N/mm$ )	Analytical method		FEM		$ \varepsilon_t $ (%), $-a$  ( $mm$ )	$ \varepsilon_t $ (%), $b$  ( $mm$ )
	$-a$	$b$	$-a$	$b$		
	( $mm$ )	( $mm$ )	( $mm$ )	( $mm$ )		
50	-0.592	0.794	-0.602	0.804	1.6	1.2
100	-0.845	1.080	-0.872	1.080	3.0	1.8
200	-1.182	1.496	-1.200	1.500	1.5	0.2

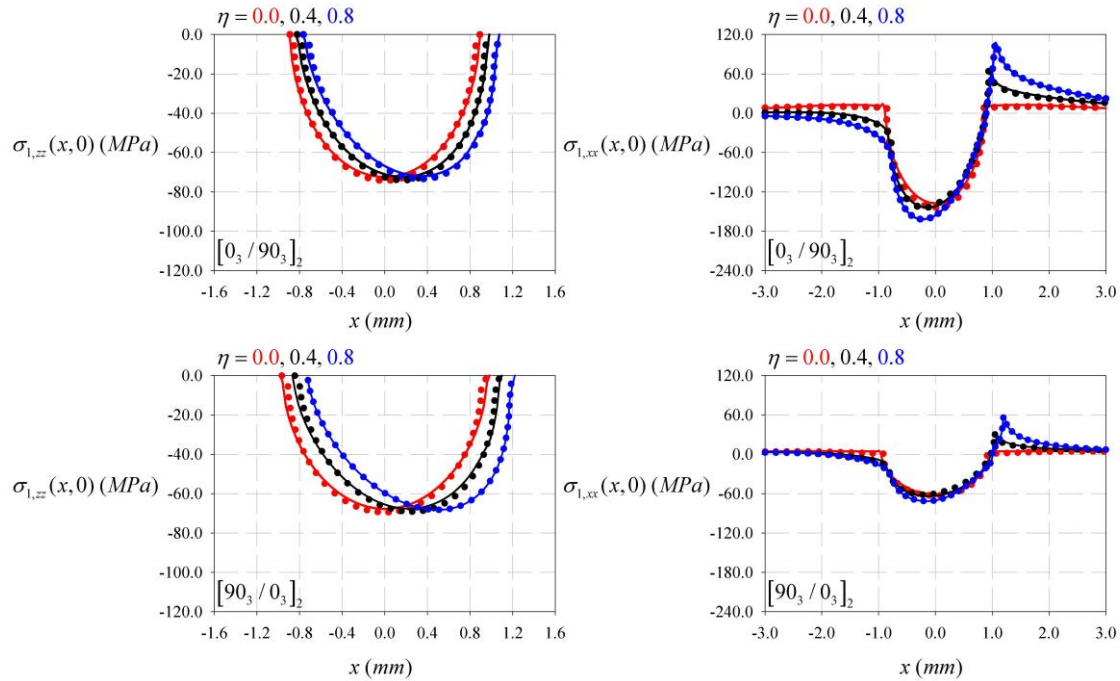


Fig. 23. Comparison of surface contact and in – plane stress distribution for  $R=100mm$ ,  $P=100N/mm$ ,  $V_f = \%40$ ,  $h_t = 4.5mm$ ,  $h = 0.375mm$ ,  $W = 90mm$ ,  $m = 12$ , solid lines represent finite element method, dotted lines represent analytical method

Table 23. Edges of contact patch for configuration  $[0_3/90_3]_2$  for varying  $\eta$

$R=100mm$ ,  $P=100N/mm$ ,  $V_f = \%40$ ,  $h_t = 4.5mm$ ,  $h = 0.375mm$ ,  $W = 90mm$ ,  
 $m = 12$

Coulomb's static coefficient of friction $\eta$	Analytical method		FEM		$ \varepsilon_t $ (%), $-a$ (mm)	$ \varepsilon_t $ (%), $b$ (mm)
	$-a$	$b$	$-a$	$b$		
	(mm)	(mm)	(mm)	(mm)		
0.0	-0.892	0.892	-0.896	0.896	0.4	0.4
0.4	-0.824	0.972	-0.836	0.980	1.4	0.8
0.8	-0.765	1.062	-0.776	1.076	1.4	1.3



Table 24. Edges of contact patch for configuration  $[90_3/0_3]_2$  for varying  $\eta$

$R = 100\text{mm}$ ,  $P = 100\text{N/mm}$ ,  $V_f = \%40$ ,  $h_t = 4.5\text{mm}$ ,  $h = 0.375\text{mm}$ ,  $W = 90\text{mm}$ ,  
 $m = 12$

Coulomb's static coefficient of friction $\eta$	Analytical method		FEM		$ \varepsilon_t $ (%), $-a$ (mm)	$ \varepsilon_t $ (%), $b$ (mm)
	$-a$	$b$	$-a$	$b$		
	(mm)	(mm)	(mm)	(mm)		
0.0	-0.968	0.968	-0.984	-0.984	1.6	1.6
0.4	-0.845	1.080	-0.872	1.100	3.0	1.8
0.8	-0.761	1.193	-0.772	1.228	1.3	2.8

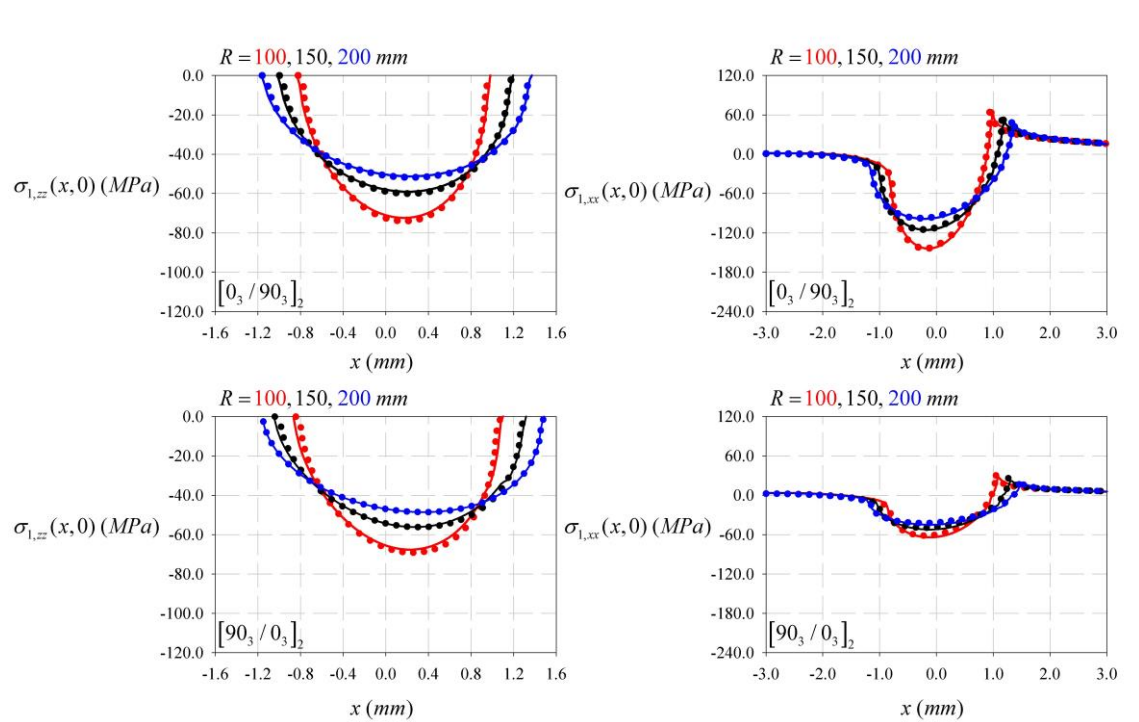


Fig. 24. Comparison of surface contact and in – plane stress distribution for  $\eta = 0.4$ ,  $P = 100\text{N/mm}$ ,  $V_f = \%40$ ,  $h_t = 4.5\text{mm}$ ,  $h = 0.375\text{mm}$ ,  $W = 90\text{mm}$ ,  $m = 12$ , solid lines represent finite element method, dotted lines represent analytical method

Table 25. Edges of contact patch for configuration  $[0_3/90_3]_2$  for varying  $R$

$\eta = 0.4, P = 100N/mm, V_f = \%40, h_t = 4.5mm, h = 0.375mm, W = 90mm,$   
 $m = 12$

Rigid cylinder radius $R$ (mm)	Analytical method		FEM		$ \varepsilon_t $ (%), $-a$ (mm)	$ \varepsilon_t $ (%), $b$ (mm)
	$-a$	$b$	$-a$	$b$		
	(mm)	(mm)	(mm)	(mm)		
100	-0.824	0.972	-0.836	0.980	1.4	0.8
150	-0.999	1.188	-1.020	1.196	2.0	0.6
200	-1.162	1.366	-1.168	1.372	0.5	0.4

Table 26. Edges of contact patch for configuration  $[90_3/0_3]_2$  for varying  $R$

$\eta = 0.4, P = 100N/mm, V_f = \%40, h_t = 4.5mm, h = 0.375mm, W = 90mm,$   
 $m = 12$

Rigid cylinder radius $R$ (mm)	Analytical method		FEM		$ \varepsilon_t $ (%), $-a$ (mm)	$ \varepsilon_t $ (%), $b$ (mm)
	$-a$	$b$	$-a$	$b$		
	(mm)	(mm)	(mm)	(mm)		
100	-0.845	1.080	-0.872	1.100	3.0	1.8
150	-1.042	1.300	-1.064	1.320	2.0	1.5
200	-1.191	1.484	-1.220	1.500	2.4	1.0

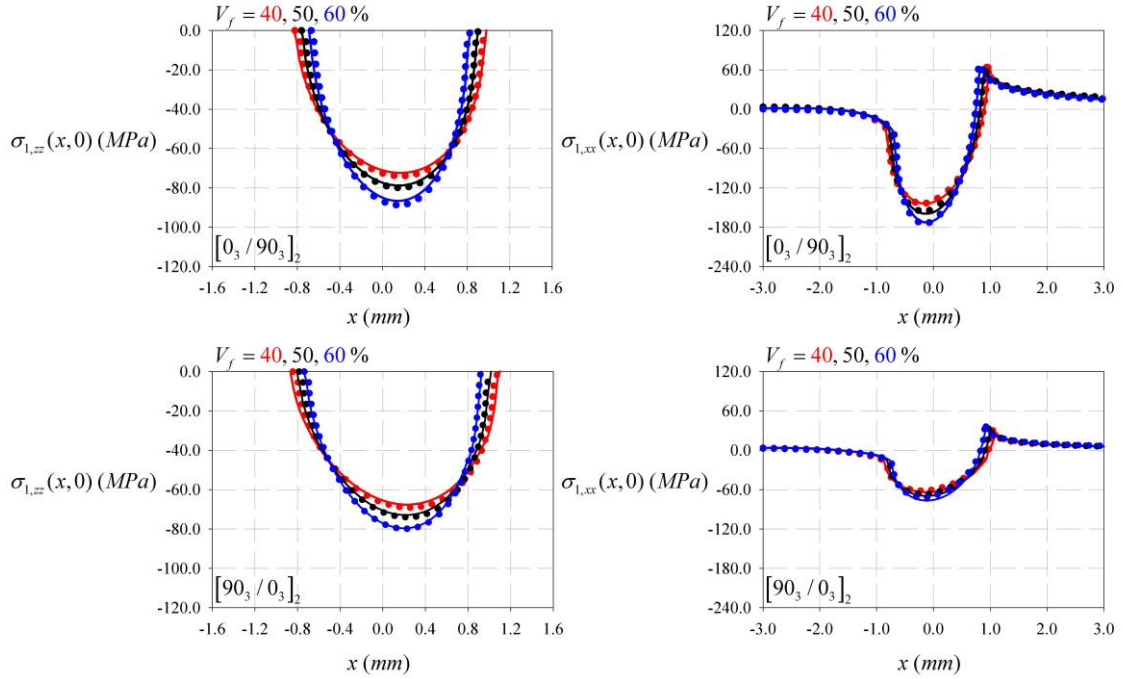


Fig. 25. Comparison of surface contact and in – plane stress distribution for  $\eta = 0.4$ ,  $P = 100N/mm$ ,  $R = 100mm$ ,  $h_t = 4.5mm$ ,  $h = 0.375mm$ ,  $W = 90mm$ ,  $m = 12$ , solid lines represent finite element method, dotted lines represent analytical method

Table 27. Edges of contact patch for configuration  $[0_3/90_3]_2$  for varying  $V_f$

$\eta = 0.4$ ,  $P = 100N/mm$ ,  $R = 100mm$ ,  $h_t = 4.5mm$ ,  $h = 0.375mm$ ,  $W = 90mm$ ,  
 $m = 12$

Fiber volume fraction $V_f$ (%)	Analytical method		FEM		$ \varepsilon_t $ (%), $-a$ (mm)	$ \varepsilon_t $ (%), $b$ (mm)
	$-a$	$b$	$-a$	$b$		
	(mm)	(mm)	(mm)	(mm)		
40	-0.824	0.972	-0.836	0.980	1.4	0.8
50	-0.762	0.889	-0.772	0.900	1.2	1.2
60	-0.688	0.828	-0.696	0.836	1.1	0.9

Table 28. Edges of contact patch for configuration  $[90_3/0_3]_2$  for varying  $V_f$

$\eta = 0.4, P = 100N/mm, R = 100mm, h_t = 4.5mm, h = 0.375mm, W = 90mm,$   
 $m = 12$

Fiber volume fraction $V_f$ (%)	Analytical method		FEM		$ \varepsilon_t $ (%), $-a$ (mm)	$ \varepsilon_t $ (%), $b$ (mm)
	$-a$	$b$	$-a$	$b$		
	(mm)	(mm)	(mm)	(mm)		
40	-0.845	1.080	-0.872	1.100	3.0	1.8
50	-0.788	1.010	-0.808	1.020	2.4	0.9
60	-0.738	0.918	-0.744	0.928	0.8	1.0

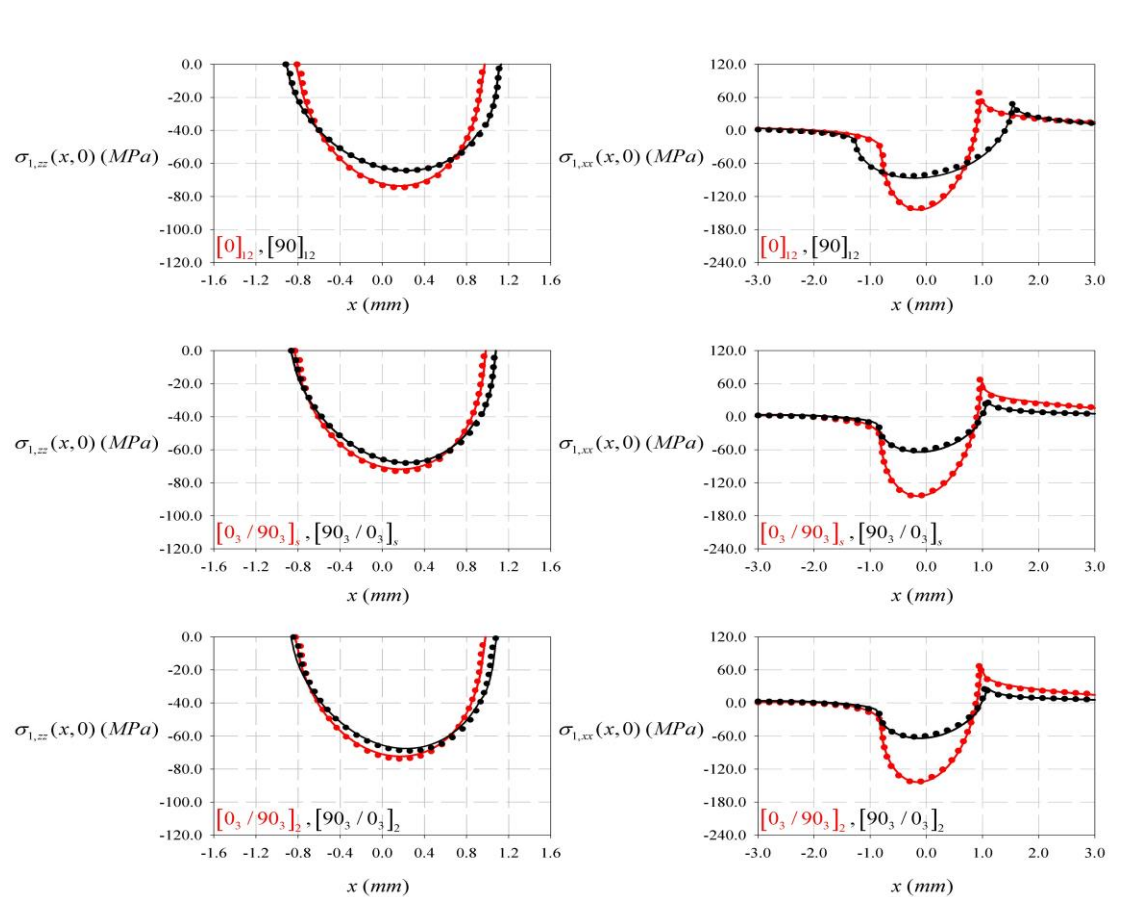


Fig. 26. Comparison of surface contact and in – plane stress distribution for  $\eta = 0.4, P = 100N/mm, R = 100mm, V_f = \%40, h_t = 4.5mm, h = 0.375mm, W = 90mm, m = 12$ , solid lines represent finite element method, dotted lines represent analytical method

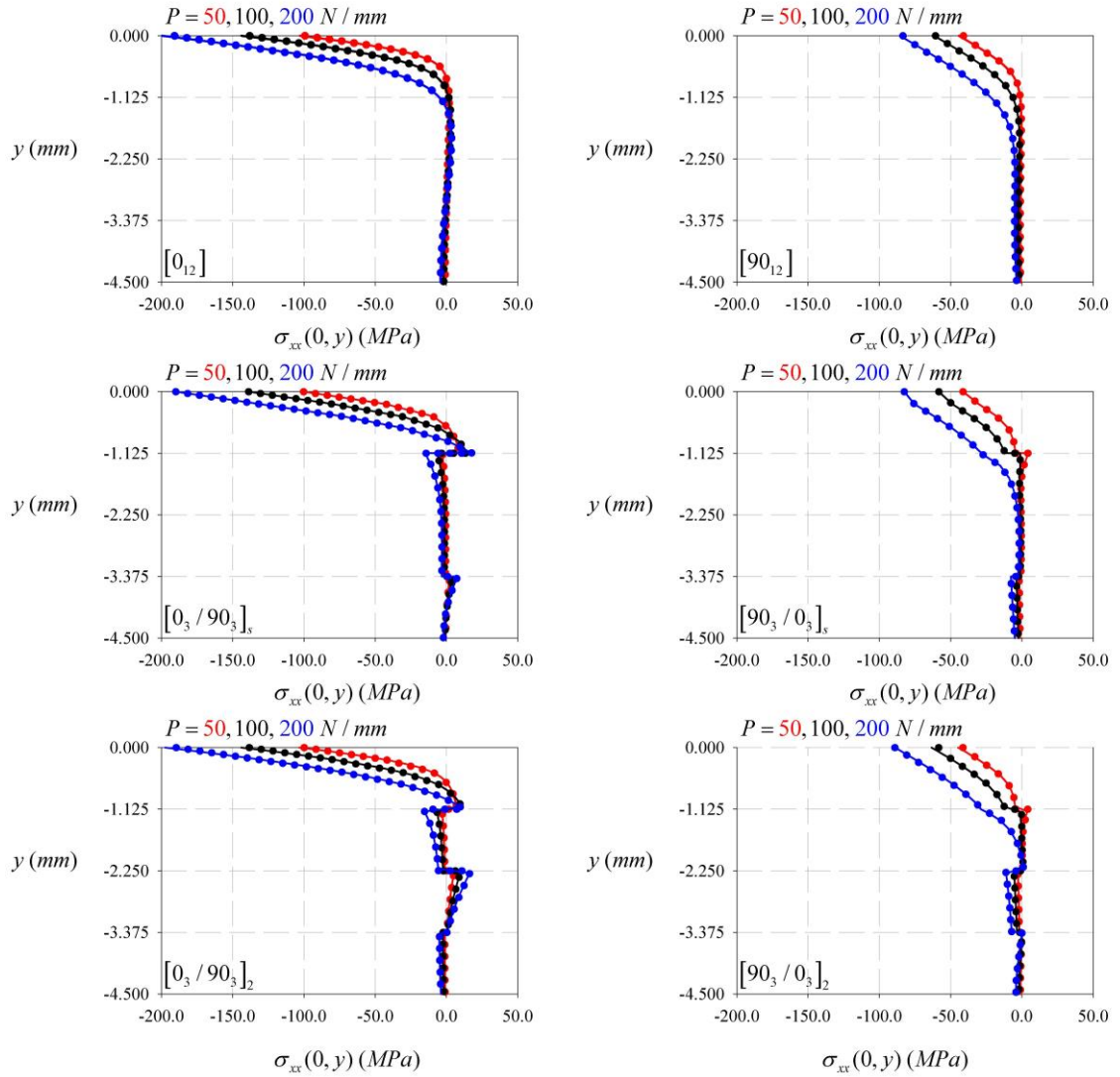


Fig. 27. Comparison of sub – surface center – line in – plane stress distributions for  $\eta = 0.4$ ,  $R = 100\text{mm}$ ,  $V_f = \%40$ ,  $h_i = 4.5\text{mm}$ ,  $h = 0.375\text{mm}$ ,  $W = 90\text{mm}$ ,  $m = 12$ , solid lines represent finite element method, dotted lines represent analytical method

### 4.3. Comparison of sub – surface in – plane stress contours

Comparison of sub – surface in – plane stress contours for six different configurations for lamina order are displayed using analytical and finite element methods. It can be seen that, the contours formed by both methods displayed very similar behavior. At the surface and sub-surface, the maximum compression and tensional peak areas matched each other.

In Fig. 28, unidirectional configurations  $[0]_{12}$  and  $[90]_{12}$  are compared. For  $[90]_{12}$ , as stiffness in normal loading direction is lower, sub – surface in – plane stresses distributed more uniformly than  $[0]_{12}$  configuration. By testing high stress areas around contact patch, this behavior can also be observed. Low stiffness behavior can result in interlaminar debonding and interface cracks as some of the contact load is still handled by the sub – surface. In comparison, the use of unidirectional configuration  $[0]_{12}$  can cause unwanted wear and micro cracks over the contact patch. To achieve optimal surface and sub – surface efficiency, the application – oriented configuration should therefore be selected.

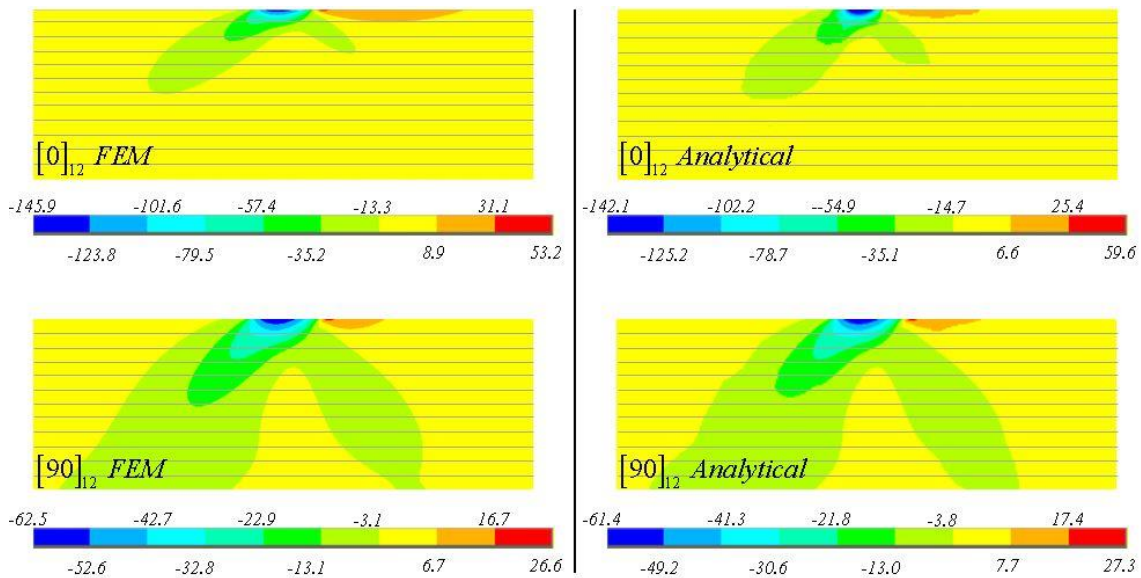


Fig. 28. Comparison of sub – surface in – plane stress contours for  $\eta = 0.4$ ,  $P = 100N/mm$ ,  $R = 100mm$ ,  $V_f = \%40$ ,  $h_t = 4.5mm$ ,  $h = 0.375mm$ ,  $W = 90mm$ ,  $m = 12$

In Fig. 29, sub – surface in – plane stress contours for  $[0_3/90_3]_s$ ,  $[90_3/0_3]_s$ ,  $[0_3/90_3]_2$ , and  $[90_3/0_3]_2$  configurations are compared. These contours validate the results presented in sub – sections (4.1 – 4.2), respectively. Lamina in contact has higher stiffness in configurations beginning with 0 degree rotation; less stress is thus moved to the sub – surface. Furthermore, low initial lamina stresses are observed for configurations started with 90 degree rotation. Tensional peaks

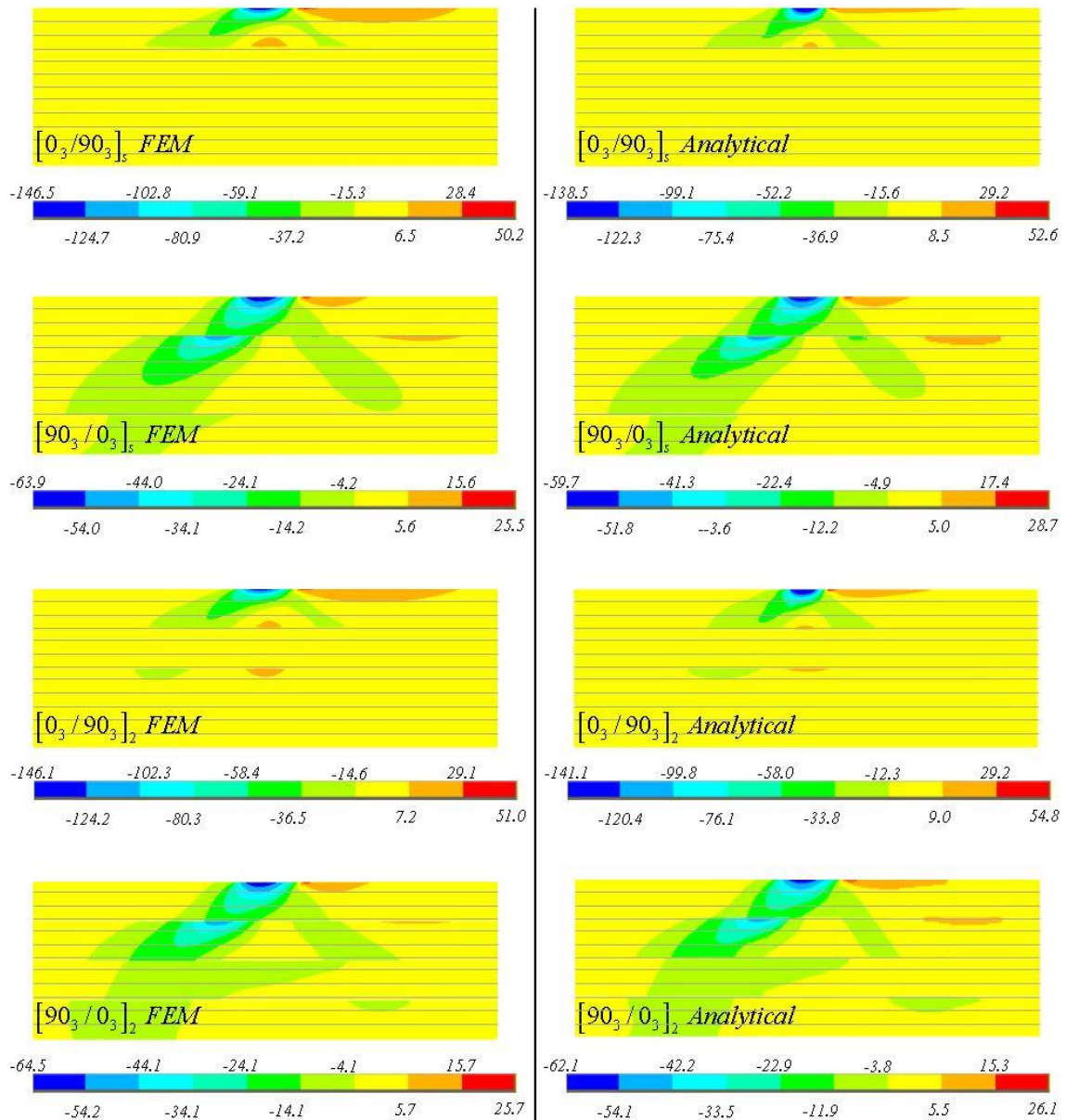


Fig. 29. Comparison of sub – surface in – plane stress contours for  $\eta = 0.4$ ,  $P = 100N/mm$ ,  $R = 100mm$ ,  $V_f = \%40$ ,  $h_t = 4.5mm$ ,  $h = 0.375mm$ ,  $W = 90mm$ ,  $m = 12$

are tracked near lamina angle shift areas at  $y = -1.125mm$  and  $y = -2.250mm$  for  $[0_3/90_3]_s$  and  $[0_3/90_3]_2$  relative to  $[90_3/0_3]_s$  and  $[90_3/0_3]_2$  configurations. Another fascinating finding presented is that a tiny compressive peak zone is monitored for  $[90_3/0_3]_2$  configuration near lamina angle shift area at  $y = -3.375mm$ , which occurred due to the direction of horizontal loading. Each of these configurations has its own advantages and disadvantages. Tribology

engineers need to take into account the most available configuration for the application to obtain maximum surface and sub – surface performance.



## 5. CONCLUSIONS

In this study, a contact mechanics problem between a frictional rigid cylinder and laminated glass fiber composites with different orientations is considered. A competent and novel parametric analysis is introduced to the industry that may be very helpful in the design of wear and micro crack resistant laminated glass fiber composites and composite coatings for tribology engineers. Analytical results are obtained by introducing a novel and modern system of analysis that relies on Cholesky decomposition, Gauss elimination, Hermite orthogonal polynomials, Fourier transforms and singular integral equation (SIE). The numerical results are achieved using a super efficient and self mesh adaptive computational model based on augmented contact formulation (ACF) and finite element method. This study can be further extended to study the dynamics of short – fiber composites, carbon – based constructs, and nonwoven fabrics for contact behavior and fracture. The following results can be drawn on the basis of observations from analytical and finite element methods:

- A numerical model based on augmented contact formulation (ACF) and finite element method for various interaction properties, material parameters, friction related terms, and lamina order is used to validate the precision of the novel analytical method.
- The consistency and speed of the integral solutions in analytical method is significantly improved by the use of Cholesky decomposition, Gauss elimination, and Hermite orthogonal polynomials. Instead of classical symbolic expressions, the use of these techniques made multi – layered contact mechanics solutions practical and achievable.
- The surface and sub – surface stress distributions and the edges of contact patch are substantially influenced by interaction properties, material parameters, friction related terms, and lamina order. In wear and micro crack resistant laminated composite architecture, application – oriented optimization of these parameters is very important.
- Surface contact stresses are more uniformly spread over the contact patch and lower compressive stress peaks are found for unidirectional

configuration of  $[90_{12}]$  relative to  $[0_{12}]$ . For other configurations began with 90 degree rotation, compression peaks in surface contact stress distributions decreased relative to the ones started with 0 degree rotation.

- Configuration angle and lamina order significantly influenced surface in – plane stress distributions. Configurations began with 90 degree rotation resulted a more distributed stress distributions over the contact patch compared to the configurations started with 0 degree rotation.
- Configuration angle and lamina order adversely affected sub – surface center – line in – plane stress distributions. Major variations are observed for stress bands in the vertical position.
- Developed analytical and finite element methods for sub – surface in – plane stress contours performed successfully with each other. Created contours showed very similar behavior, where high stress zones are matched at surface and sub –surface.

## 6. REFERENCES

- [1] H. P. Jost, Lubrication (tribology), education and research; a report on the present position and industry's needs, 1. Edition, National Government Publication, **1966**.
- [2] H. Hertz, Journal für die reine und angewandte Mathematik, 92 (**1881**) 156 – 171.
- [3] J. R. Barber, M. Ciavarella, International Journal of Solids and Structures, 37 (**2000**) 29 – 43.
- [4] L. W. McKeen, Introduction to the tribology of fluorocoatings, 2. Edition, William Andrew Publishing, **2016**.
- [5] P. Wriggers, Thermo – mechanical contact, 1. Edition, Springer Berlin Publishing, **2006**.
- [6] A. L. Dumont, J. P. Bonnet, T. Charlier, J. M. Ferreira, Journal of the European Ceramic Society, 21 (**2001**) 2353 – 2360.
- [7] X. Jin, L. Wu, Y. Sun, L. Guo, Materials Science and Engineering, 509 (**2009**) 63 – 68.
- [8] M. Nemat – Alla, M. Ata, M. Ragab, W. Khair – Eldeen, Material Sciences and Applications, 2 (**2011**) 1708 – 1718.
- [9] M. Thieme, K. P. Wieters, F. Bergner, D. Scharnweber, H. Worch, J. Ndop, T. J. Kim, W. Grill, Journal of Materials Science: Materials in Medicine, 12 (**2001**)
- [10] W. G. Cooley, Application of functionally graded materials in aircraft structures, PhD Thesis, Air Force Institute of Technology, **2005**.
- [11] P. Baumli, A. Al – Azzawi, Materials Science and Engineering, 40 (**2015**) 26 – 32.
- [12] S. Toros, K. Altinel, Journal of Mechanical Science and Technology, 30 (**2016**) 3137 – 3141.
- [13] J. He, M. Wang, 4. International Conference on Sustainable Energy and Environmental Engineering, 20 – 21 December 2015, Atlantis Press, Beijing, **2016**, p. 715.

- [14] R. M. Mahamood, E. T. Akinlabi, Types of functionally graded materials and their areas of application, 2. Edition, Springer International Publishing, **2017**.
- [15] R. D. Mindlin, Journal of Applied Mechanics, 16 (**1949**) 259 – 268.
- [16] I. N. Sneddon, Fourier transforms, 1. Edition, Dover Publications, **1951**.
- [17] N. I. Muskhelishvili, Some basic problems of the mathematical theory of elasticity, 1. Edition, Springer Netherlands, **1977**.
- [18] D. A. Spence, Journal of Elasticity, 5 (**1975**) 297 – 319.
- [19] L. M. Keer, D. B. Mowry, International Journal of Solids and Structures, 15 (**1979**) 33 – 39.
- [20] M. T. Hanson, Journal of Tribology, 114 (**1992**) 606 – 611.
- [21] C. H. Kuo, L. M. Keer, Journal of Tribology, 114 (**1992**) 253 – 261.
- [22] X. Ning, M. Lovell, W. S. Slaughter, Wear, 260 (**2006**) 693 – 698.
- [23] R. C. Batra, W. Jiang, International Journal of Solids and Structures, 45 (**2008**) 5814 – 5830.
- [24] D. Jasinska, M. Janus – Michalska, Engineering Transactions, 56 (**2008**) 201 – 225.
- [25] C. Bagault, D. Nelias, M. – C. Baietto, Journal of Tribology, 134 (**2012**) 031401 – 1.
- [26] T. Hayashi, H. Koguchi, N. Nishi, Journal of Mechanics and Physics of Solids, 61 (**2013**) 1753 – 1767.
- [27] Y. – T. Zhou, T. – W. Kim, International Journal of Mechanical Sciences, 89 (**2014**) 332 – 343.
- [28] M. Mokhtari, D. J. Schipper, N. Vleugels, J. W. M. Noordermer, International Tribology Conference, 16 – 20 September 2015, Japanese Society of Tribologists Press, Tokyo, **2015**, p. 34.
- [29] T. Hayashi, H. Koguchi, International Journal of Solids and Structures, 53 (**2015**) 138 – 147.
- [30] W. W. F. Chong, S. J. Chidlow, Mechanics of Materials, 84 (**2015**) 1 – 11.
- [31] W. W. F. Chong, S. J. Chidlow, Mechanics of Materials, 101 (**2016**) 1 –

13.

[32] M. Mokhtari, D. J. Schipper, N. Vleugels, J. W. M. Noordermer, *Tribology International*, 97 (2016) 116 – 123.

[33] H. Liu, E. Pan, *Mechanics of Materials*, 118 (2018) 62 – 73.

[34] D. A. Pozharskii, *Journal of Applied Mechanics and Technical Physics*, 59 (2018) 491 – 497.

[35] W. K. Binienda, M. – J. Pindera, *Composites Science and Technology*, 50 (1994), 119 – 128.

[36] C. Hwu, C. W. Fan, *International Journal of Solids and Structures*, 35 (1998) 3945 – 3960.

[37] O. Jorgensen, A. E. Giannakopoulos, S. Suresh, *International Journal of Solids and Structures*, 35 (1998), 5097 – 5113.

[38] W. Zhang, W. K. Binienda, M. – J. Pindera, *Composites Science and Technology*, 59 (1999) 331 – 343.

[39] M. Krumova, C. Klingshirn, F. Hauptert, K. Friedrich, *Composites Science and Technology*, 61 (2001) 557 – 563.

[40] S. R. Swanson, *International Journal of Solids and Structures*, 41 (2004) 1945 – 1959.

[41] B. Erbas, E. Yusufoglu, J. Kaplunov, *Journal of Engineering Mathematics*, 70 (2010) 399 – 409.

[42] A. Soom, C. – C. Chen, Y. Berthier, 6th European Conference on Braking, 24 – 25 November 2010, CCSD Press, Lille, 2010, p. 54.

[43] H. Ashrafi, M. Mahzoon, M. Shariyat, *Iranian Journal of Materials Science & Engineering*, 9 (2012) 29 – 41.

[44] N. Myshkin, A. Kovalev, D. Spaltman, M. Woydt, *Journal of Applied Polymer Science*, 131 (2014) 1 – 9.

[45] M. A. Guler, *International Journal of Mechanical Sciences*, 87 (2014) 72 – 88.

[46] Y. – T. Zhou, K. Y. Lee, *Mechanics of Materials*, 69 (2014) 237 – 250.

- [47] P. Chen, S. Chen, J. Peng, *Acta Mechanica*, 226 (2015) 4207 – 4221.
- [48] D. Sarikaya, S. Dag, *International Journal of Solids and Structures*, 90 (2016) 1 – 11.
- [49] Y. Alinia, M. Hosseini – Nasab, M. A. Guler, *European Journal of Mechanics / A Solids*, 70 (2018) 156 – 171.
- [50] I. Comez, K. B. Yilmaz, M. A. Guler, B. Yildirim, *Archieve of Applied Mechanics*, 89 (2019) 1403 – 1419.
- [51] K. B. Yilmaz, I. Comez, M. A. Guler, B. Yildirim, *Zeitschrift für angewandte Mathematik und Physik*, 99 (2019) e201800117.
- [52] K. B. Yilmaz, I. Comez, M. A. Guler, B. Yildirim, *Mechanics of Materials*, 137 (2019) 103132.
- [53] I. Comez, K. B. Yilmaz, *Zeitschrift für angewandte Mathematik und Physik*, 99 (2019) e201800084.
- [54] K. B. Yilmaz, I. Comez, M. A. Guler, B. Yildirim, *Journal of Strain Analysis for Engineering Design*, 54 (2019) 254 – 275.
- [55] Chamis, C., *Journal of Composites, Technology and Research*, 11 (1989) 3 – 14.
- [56] Sadd, M., *Elasticity: Theory, applications, and numerics*, 4. Edition, Academic Press, 2021.
- [57] Sneddon, I. N., *Fourier transforms*, 1. Edition, Dover Publications, 1995.
- [58] Erdogan, F., *Mixed boundary – value problems in mechanics in: mechanics today*, 4th Edition, Pergamon Press, 1978.
- [59] Higham, N. J., *Wiley Interdisciplinary Reviews Computational Statistics*, 1 (2009) 251 – 254.
- [60] Higham, N. J., *Wiley Interdisciplinary Reviews Computational Statistics*, 3 (2011) 230 – 238.
- [61] Dattoli, G., Srivastava, H. M., Zhukovsky, K., *Journal of Computational and Applied Mathematics*, 182 (2004), 165 – 172.
- [62] Hrennikoff, A., *Journal of Applied Mechanics*, 8 (1941) 169 – 175.

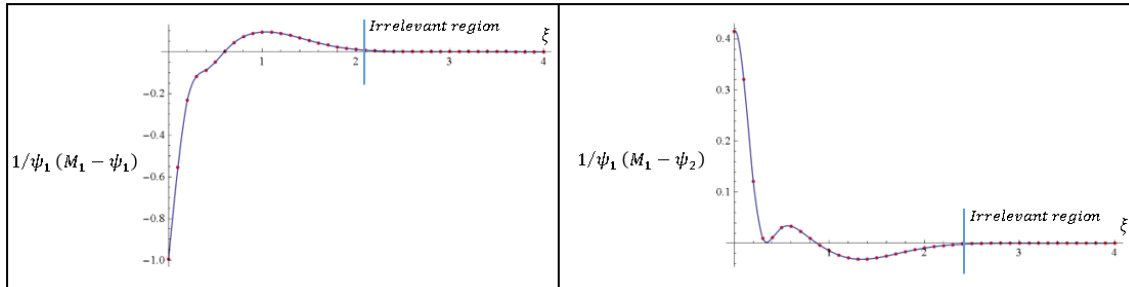
- [63] Courant, R., Bulletin of the American Mathematical Society, 49 (1943) 1 – 23.
- [64] Mahajan, P., Composite Science and Technology, 58 (1998) 505 – 513.
- [65] Diao, D. F., Tribology International, 32 (1999) 25 – 32.
- [66] McDevitt, T. W., Laursen, T. A., International Journal for Numerical Methods in Engineering, 48 (2000) 1525 – 1547.
- [67] Varadi, K., Neder, Z., Friedrich, K., Flöck, J., Composites Science and Technology, 61 (2001) 1853 – 1862.
- [68] Kim, J. H., Paulino, G. H., Journal of Applied Mechanics, 69 (2002) 502 – 514.
- [69] Huang, X., Pelegri, A., Composites Science and Technology, 67 (2007) 1311 – 1319.
- [70] Ceseracciu L., Jimenez – Pique, E., Fett, T., Anglada, M., Composites Science and Technology, 68 (2008) 209 – 214.
- [71] Farah, P., Popp, A., Wall, W. A., Computational Mechanics 55 (2015) 209 – 228.
- [72] Farah, P., Gitterle, M., Wall, W. A., Popp, A., Key Engineering Materials 681 (2016) 1 – 18.
- [73] Seitz, A., Farah, P., Kremheller, J., Wohlmuth, B. I., Wall, W. A., Popp, A., Computer Methods in Applied Mechanics and Engineering, 301 (2016) 259 – 280.
- [74] Farah, P., Wall, W. A., Popp, A., International Journal for Numerical Methods in Engineering, 111 (2017) 325 – 353.
- [75] Guinovart – Sanjuan, D., Rizzoni, R., Rodriguez – Ramos, R., Gunioart – Diaz, R., Bravo – Castellero, J., Alfonso – Rodriguez, R., Lebon, F., Dumont, S., Sevostianov, I., Sabina, F. J., Composite Structures, 176 (2017) 539 – 546.
- [76] Farah, P., Wall, W. A., Popp, A., International Journal for Numerical Methods in Engineering, 114 (2018) 255 – 291.
- [77] Tekkaya, A. E., Martins, P. A. F., Engineering Computations, 26 (2009) 1026 – 1055.

- [78] ANSYS Inc., ANSYS Mechanical Structural Nonlinearities, Design Report, Canonsburg, **2016**.
- [79] ANSYS Inc., ANSYS Mechanical APDL Structural Analysis Guide, Design Report, Canonsburg, **2018**.
- [80] ANSYS Inc., ANSYS Mechanical APDL Modeling and Meshing Guide, Design Report, Canonsburg, **2018**.
- [81] Mijar, A. R., Arora, J. S., Structural and Multidisciplinary Optimization, 28 (**2004**) 99 – 112.
- [82] Ling. D., Yang, Q., Cox, B. N., International Journal of Fracture, 156 (**2009**) 53 – 73.
- [83] Hirmand, M., Vahab, M, Khoei, A. R., Finite Elements in Analysis and Design, 107 (**2015**), 28 – 43.



# APPENDIX

## APPENDIX 1 – Curve fit plots for $1/\psi_1(M_1 - \psi_1)$ and $1/\psi_1(M_1 - \psi_2)$ for $[90_3/0_3]_s$ configuration



## APPENDIX 2 – Publications derived from thesis



Research paper

### Sliding frictional contact analysis of a monoclinic coating/isotropic substrate system



K.B. Yilmaz<sup>a</sup>, İ. Çömez<sup>a,b</sup>, M.A. Güler<sup>c</sup>, B. Yildirim<sup>a</sup>

<sup>a</sup> Department of Mechanical Engineering, Hacettepe University, Ankara 06800, Turkey

<sup>b</sup> Department of Civil Engineering, Karadeniz Technical University, Trabzon 61080, Turkey

<sup>c</sup> College of Engineering and Technology, American University of the Middle East, Kuwait

#### ARTICLE INFO

##### Keywords:

Sliding contact  
Metal and polymer matrix monoclinic coating  
Singular integral equation  
Augmented finite element method  
Stress intensity factors

#### ABSTRACT

Owing to innovative developments and the need to satisfy the requirements of engineering applications, new and improved materials are investigated by engineers to compensate for the drawbacks of conventional materials. There is an urgent need for the tribology community to properly investigate the behavior of these materials before utilizing them in real life. In this study, the sliding frictional contact between a monoclinic coating/isotropic substrate system and a rigid cylindrical punch is provided using an analytical formulation and finite element method (FEM). The analytical expressions for the stress and displacement fields are presented, and the resulting singular integral equations (SIEs) are solved numerically. Details of the analytical formulation and the discretization used in the solution method for the SIEs are also presented. For obtaining the numerical solution, an augmented finite element method is used with plane strain conditions and 6-node higher order finite elements. According to the results, the analytical formulation and FEM results are consistent. Using different lamina orientations, coefficient of friction, and geometric/material parameters, provides the tribology community with a highly qualified parametric study that informs surface wear and surface fatigue crack initiation in contact mechanics problems

#### 1. Introduction

The tribology community can benefit from studies that explore benchmark problems with different types of materials and contact conditions. The goal is to improve the characteristics of surfaces that are in motion in order to reduce surface friction, wear, and/or to improve lubrication. In recent decades, more research has focused on these problems as nearly all engineering applications require to be designed more effectively to compensate for the extravagance of resources due to high wear and high surface friction. Using unconventional materials for engineering purposes provides many advantages because one can achieve identical or better material characteristics by combining a number of properties that are not commonly found together in a single conventional material, such as better chemical resistance, higher thermal resistance, or higher strength. The contact and material behaviors of these unconventional materials is load transferring systems should be explored. Therefore, understanding the characteristics of contact surfaces made of different materials is important in systems design.

Engineers have used unconventional materials since early times, such as anisotropic, transversely isotropic, orthotropic, and monoclinic materials. Nowadays, unconventional materials are used in many applications, including automotive, marine, defense, construction, medicine, and aerospace. Turbine blade coatings, steering systems in vehicles, bullet proof -vests, armored plates, propeller shafts, carbon fiber car parts, dental implants, water proof ceiling parts, cylindrical pressure vessels, functionally graded thermal barrier coatings, and fire insulation vests are some prevalent examples of products that use unconventional materials (Baumli and Al-Azzawi, 2015; He and Wang, 2016).

Understanding wear/friction mechanisms and investigating the resulting stress distribution/surface traction are key aspects in contact mechanics problems. In unconventional materials, such as anisotropic, transversely isotropic, orthotropic, and monoclinic materials, solution methods are much more complicated as there is a large number of independent and dependent elastic constants in the analytical formulations because material properties vary along the principle axes. Therefore, fewer studies have focused on problems involving these

\* Corresponding author.

E-mail addresses: korhanb.yilmaz@hacettepe.edu.tr, korhanbabacanyilmaz@gmail.com (K.B. Yilmaz), isacomez@ktu.edu.tr (İ. Çömez), mehmet.guler@aum.edu.kw (M.A. Güler), boray@hacettepe.edu.tr (B. Yildirim).

<https://doi.org/10.1016/j.mechmat.2019.103132>

Received 20 April 2019; Received in revised form 22 July 2019; Accepted 24 July 2019

Available online 27 July 2019

0167-6636/ © 2019 Elsevier Ltd. All rights reserved.

types of materials. We provide some detail regarding contact mechanics studies conducted with these materials. *Batra and Jiang (2008)* examined plane contact using Stroh's formalism. A highly parametric study was used to delimit the parameters, and some qualified results that serve as comparable benchmarks for other solution methods were presented. The exact solutions for the interplay between two different punches and the effect of elastic parameters on contact deformation were presented by *Zhou and Kim (2014)*. Furthermore, *Keer and Mowry (1979)* examined the behavior of two transversely isotropic spheres in sliding contact. In that study, they determined the stress field due to the tangential load and superposed this with the case of normal loading. A problem involving a multi-layered transversely isotropic half-plane was studied (*Kuo and Keer, 1992*); a frictional spherical punch was used as the punch profile and the variation in stresses related to contact failure were investigated. The frictional Hertzian contact was examined by including surface traction and Coulomb friction into the analytical equations (*Hanson, 1992*). It was shown that Green's functions are very effective in analytical problems. Later, a contact problem was solved by assuming bonded and unbonded contact types, allowing the accuracy of solution methods to be checked (*Ning et al., 2006*). Persson's theory on contact mechanics problems was used to model deformation behavior using experimental and numerical methods (*Mokhtari et al., 2016*). It was found that, using an unconventional material greatly affects the contact and friction behavior of solids compared to classical isotropic materials. The effect of transversely isotropic material property along a thin interlayer with various interface conditions were also investigated by *Liu and Pan (2018)*, where a flat-ended rigid cylindrical punch profile was used and a new approach in generating the results was presented.

Contact mechanics studies have also focused on orthotropic materials. A detailed analysis of contact problems involving orthotropic materials focused on using the methods for interface crack problems (*Hwu and Fan, 1998*). In another frictionless study (*Shi et al., 2003*), the stress equations for a rigid ellipsoidal indenter in contact with an orthotropic surface were solved numerically. The formulation in *Willis (1966)* and *Srinivas and Rao (1970)* was extended in *Swanson (2004)* to calculate the stresses on orthotropic materials. A singular integral equation (SIE) approach, was used to investigate the contact behavior for a thick orthotropic strip (*Erbas et al., 2011*). Then, Gauss-Chebyshev integration formulas were used to provide analytical benchmark solutions (*Alinia et al., 2018*).

Studies that considered monoclinic materials are quite limited, yet the behavior of the stresses and contact areas of metal and polymer-matrix composites under loading with a rigid parabolic punch was investigated (*Binienda and Pindera, 1994*). By altering the off-axis lamina orientation and using different values for stiffness parameters, they concluded that local bending characteristics are highly dependent on the lamina sequence. A contact problem for a monoclinic layer and frictional rigid punch was considered by *Zhou and Lee (2014)*, where Fourier transformation was used to reduce the problem to a SIE, and the effect of friction on the results was demonstrated. Later, the effects of sliding surface friction, orientation angle, and gradation parameter on an arbitrarily oriented half-plane were investigated; it was concluded that, these type of studies can provide early benchmark results in designing strong wear resistant surfaces (*Chen et al., 2015*).

Many studies have focused on investigating contact mechanics problems with computational methods. A finite element (FE) study was conducted to investigate the force/indentation behavior of laminated composite beams using the multi-point constraint method in ABAQUS (*Mahajan, 1998*). An elliptic contact loading condition was used to investigate the critical yielding behavior of hard coatings with FE study, and it was found that using low values for the critical yielding ratio is very important as higher values may initiate interlayer yielding (*Diao, 1999*). Results from contact strength tests on ceramic laminates under Hertzian contact conditions were conducted to investigate the surface and inner layer failure behaviors experimentally and using

finite element method (FEM) (*Ceseracciu et al., 2008*). It was found that high stresses can arise far from the contact region, which may lead to failure in the inner layers of the composite. Imperfect contact conditions for laminated shell composites were studied, where the goal was to determine effective elastic properties in contact areas (*Guinovart-Sanjuán et al., 2017*).

Mortar finite elements were used for the first time to discretize the contact surface in frictional contact mechanics problems, and it was shown that contact kinematics can be easily evaluated with these type of finite elements (*McDevitt and Laursen, 2000*). A new contact algorithm was developed (*Váradí et al., 2001*), where different types of experiments and numerical simulations were used to predict the surface wear and contact temperature in anisotropic materials. A contact problem for an infinitely long orthotropic plate was investigated by linearly and exponentially graded finite elements to investigate the efficiency of graded finite elements over conventional ones (*Kim and Paulino, 2002*). It was found that using graded finite elements can help predict local stress concentration more accurately. Later, it was found that unsmoothed mortar formulations for contact mechanics problems have better mating characteristics with non-conforming mesh structures (*Tur et al., 2012*). An isogeometric enrichment technique for contact mechanics problems involving frictional contacts and mixed-mode debonding was also presented (*Corbett and Sauer, 2015*), where a discretization on the contact surface for the enrichment technique was used; it was shown that this technique has advantages in generating surfaces. A comparison and benchmark study for segment-based and element-based integration methods for finite elements were conducted in *Farah et al. (2015)*.

An interesting study was presented by *Huang and Pelegri (2007)*, where some complex nano-indentation problems for film/substrate interfaces were considered by employing different types of rigid punches and interface conditions. The contact mechanics problem for an elastically graded material and an arbitrary sliding rigid punch was considered (*Dag et al., 2009*), where quadratic finite elements for elemental discretization were used and the effects of lateral inhomogeneity and friction on the resulting surface stresses were investigated. Two different types of Hertzian contact conditions were later studied using FEM (*Brezeanu, 2014*). After that, the contact behavior of a hard coating loaded by a rigid flat punch was investigated with FEM, and a new method for calculating the elasticity limit in coated surfaces was presented (*Goltsberg and Etsion, 2016*).

Some studies related to contact mechanics of monoclinic materials are discussed in the aforementioned paragraph. However, further investigation of the literature indicates that there are no preceding studies related to sliding frictional contact mechanics problems involving monoclinic coated surfaces. Therefore, a sliding frictional contact problem of a monoclinic coating/isotropic substrate system with a rigid cylindrical punch is considered in this study under plane strain conditions. The problem is solved analytically (SIE) and numerically (FEM). The novelty of this study originates from investigating the frictional contact conditions and lamina orientation on a coating/substrate system by employing different types of composite coatings (polymer-matrix and metal-matrix composites), geometric parameters, and different punch profiles. Furthermore, the objective of this study is to provide highly qualified benchmark solutions to be used by the tribology community regarding composite coated surfaces. The results presented in this paper clearly show the effects of lamina orientation angle, coefficient of friction, geometric parameters, monoclinic material type on surface and subsurface stresses.

## 2. Analytical formulation

A graphical representation of the problem considered in this study is shown in *Fig. 1*, where the substrate is assumed to be a half-plane and perfectly bonded to a monoclinic coating. The monoclinic coating is loaded with various types of punch profiles (cylindrical, parabolic, and

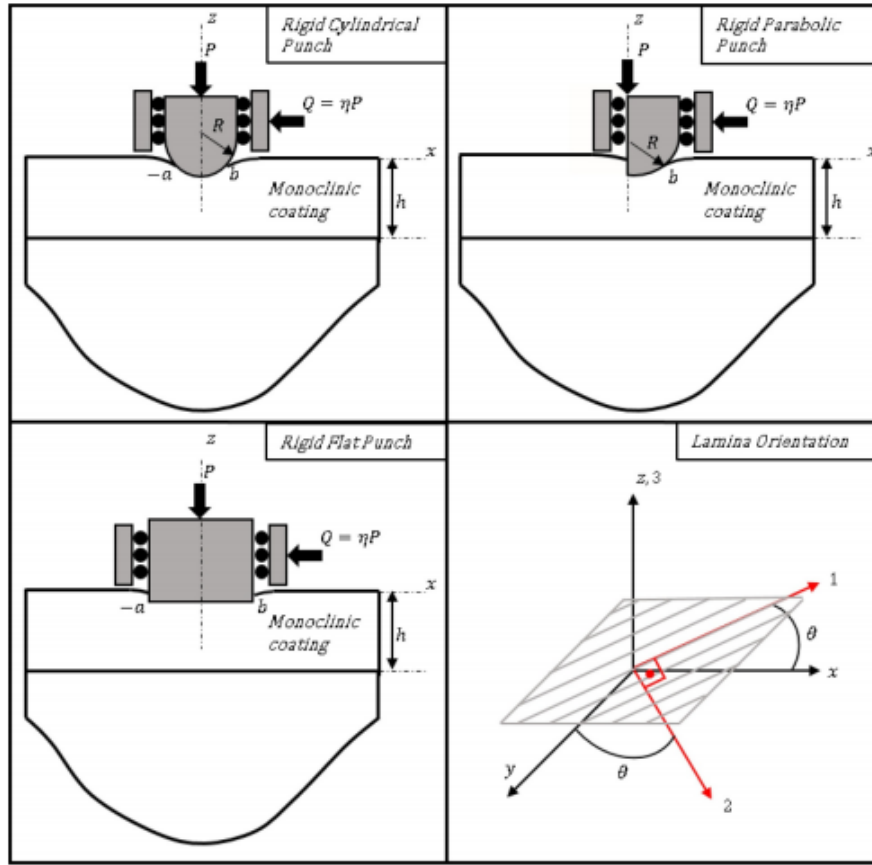


Fig. 1. Geometry of the sliding frictional contact problem for the monoclinic coating/isotropic substrate system.

flat) under plane strain conditions. The stress-displacement relations for a monoclinic coating are

$$\sigma_{xx} = \hat{C}_{11} \frac{\partial u_1}{\partial x} + \hat{C}_{13} \frac{\partial w_1}{\partial z} + \hat{C}_{16} \frac{\partial v_1}{\partial x} \quad (1a)$$

$$\sigma_{yy} = \hat{C}_{12} \frac{\partial u_1}{\partial x} + \hat{C}_{23} \frac{\partial w_1}{\partial z} + \hat{C}_{26} \frac{\partial v_1}{\partial x} \quad (1b)$$

$$\sigma_{zz} = \hat{C}_{13} \frac{\partial u_1}{\partial x} + \hat{C}_{33} \frac{\partial w_1}{\partial z} + \hat{C}_{36} \frac{\partial v_1}{\partial x} \quad (1c)$$

$$\tau_{xz} = \hat{C}_{55} \left( \frac{\partial u_1}{\partial z} + \frac{\partial w_1}{\partial x} \right) + \hat{C}_{45} \frac{\partial v_1}{\partial z} \quad (1d)$$

$$\tau_{yz} = \hat{C}_{44} \frac{\partial v_1}{\partial z} + \hat{C}_{45} \left( \frac{\partial u_1}{\partial z} + \frac{\partial w_1}{\partial x} \right) \quad (1e)$$

$$\tau_{xy} = \hat{C}_{16} \frac{\partial u_1}{\partial x} + \hat{C}_{36} \frac{\partial w_1}{\partial z} + \hat{C}_{66} \frac{\partial v_1}{\partial x} \quad (1f)$$

where  $\hat{C}_i$  represents the global stiffness coefficients along the  $-x$ ,  $-y$ , and  $-z$  directions. They can be calculated in terms of the lamina

orientation angle  $\theta$  and the local stiffness coefficients  $C_{ij}$  along the  $-x_1$ ,  $-y_1$ , and  $-z_1$  directions as follows:

$$C_{11} = C_{11} \cos^4 \theta + 2(C_{12} + 2C_{66}) \cos^2 \theta \sin^2 \theta + C_{22} \sin^4 \theta \quad (2a)$$

$$\hat{C}_{12} = (C_{11} + C_{22} - 4C_{66}) \cos^2 \theta \sin^2 \theta + C_{12} (\cos^4 \theta + \sin^4 \theta) \quad (2b)$$

$$\hat{C}_{13} = C_{13} \cos^2 \theta + C_{23} \sin^2 \theta \quad (2c)$$

$$C_{16} = \cos \theta \sin \theta (\cos^2 \theta (C_{11} - C_{12} - 2C_{66}) + \sin^2 \theta (C_{12} - C_{22} + 2C_{66})) \quad (2d)$$

$$\hat{C}_{22} = C_{11} \sin^4 \theta + 2(C_{12} + 2C_{66}) \cos^2 \theta \sin^2 \theta + C_{22} \cos^4 \theta \quad (2e)$$

$$\hat{C}_{23} = C_{23} \cos^2 \theta + C_{13} \sin^2 \theta \quad (2f)$$

$$C_{33} = C_{33} \quad (2g)$$

$$\hat{C}_{36} = (C_{13} - C_{23}) \cos \theta \sin \theta \quad (2h)$$

$$\hat{C}_{44} = C_{44} \cos^2 \theta + C_{55} \sin^2 \theta \quad (2i)$$

$$C_{45} = (C_{55} - C_{44}) \cos \theta \sin \theta \quad (2j)$$

$$\hat{C}_{55} = C_{55} \cos^2 \theta + C_{44} \sin^2 \theta \tag{2k}$$

$$\hat{C}_{66} = (C_{11} - 2C_{12} - 2C_{22}) \cos^2 \theta \sin^2 \theta + C_{66} (\sin^2 \theta - \cos^2 \theta)^2 \tag{2l}$$

The displacements are,

$$C_{11} \frac{\partial^2 u_0}{\partial x^2} + C_{55} \frac{\partial^2 u_0}{\partial z^2} + C_{16} \frac{\partial^2 v_1}{\partial x^2} + C_{45} \frac{\partial^2 v_1}{\partial z^2} + (C_{13} + C_{33}) \frac{\partial^2 w_1}{\partial x \partial z} = 0 \tag{3a}$$

$$C_{36} \frac{\partial^2 u_1}{\partial x^2} + C_{45} \frac{\partial^2 u_0}{\partial z^2} + C_{66} \frac{\partial^2 v_1}{\partial x^2} + C_{44} \frac{\partial^2 v_1}{\partial z^2} + (C_{36} + C_{45}) \frac{\partial^2 w_1}{\partial x \partial z} = 0 \tag{3b}$$

$$(C_{13} + C_{33}) \frac{\partial^2 u_0}{\partial x \partial z} + (C_{36} + C_{45}) \frac{\partial^2 v_1}{\partial x \partial z} + C_{55} \frac{\partial^2 w_1}{\partial x^2} + C_{33} \frac{\partial^2 w_1}{\partial z^2} = 0 \tag{3c}$$

Applying a Fourier transform to Eq. (3) yields

$$-\hat{C}_{11} \xi^2 \hat{u} - \hat{C}_{16} \xi^2 \hat{v} - I_1^2 (\hat{C}_{13} + \hat{C}_{33}) \frac{d\hat{w}}{dz} + \hat{C}_{55} \frac{d^2 \hat{u}}{dz^2} + \hat{C}_{45} \frac{d^2 \hat{v}}{dz^2} = 0 \tag{4a}$$

$$-C_{36} \xi^2 \hat{u} - C_{45} \xi^2 \hat{v} - I_1^2 (C_{36} + C_{45}) \frac{d\hat{w}}{dz} + C_{45} \frac{d^2 \hat{u}}{dz^2} + C_{44} \frac{d^2 \hat{v}}{dz^2} = 0 \tag{4b}$$

$$-C_{55} \xi^2 \hat{w} - I_1^2 (\hat{C}_{13} + \hat{C}_{33}) \frac{d\hat{u}}{dz} - I_1^2 (C_{36} + C_{45}) \frac{d\hat{v}}{dz} - C_{33} \frac{d^2 \hat{w}}{dz^2} = 0 \tag{4c}$$

The transformed displacement components for the monoclinic coating are

$$\{\hat{u}_j(\xi, z), \hat{v}_j(\xi, z), \hat{w}_j(\xi, z)\} = \sum_{j=1}^6 \{1, I k_j, I m_j\} A_{ij} e^{\eta_j z} \tag{5}$$

where the expressions for  $\eta_j$ ,  $k_j$ , and  $m_j$  ( $j = 1, 2, \dots, 6$ ) are given in Appendix A. Moreover, the stresses on the monoclinic coating can be found by substituting Eq. (5) into (1):

$$\sigma_{xx}(x, z) = \frac{1}{2\pi} \int_{-\infty}^{\infty} [-I_1^2 \sum_{j=1}^6 A_{ij} (\hat{C}_{11} + \hat{C}_{33} m_j - \hat{C}_{13} k_j n_j) e^{\eta_j z}] e^{-I_1 \xi} d\xi \tag{6a}$$

$$\sigma_{yy}(x, z) = \frac{1}{2\pi} \int_{-\infty}^{\infty} [-I_1^2 \sum_{j=1}^6 A_{ij} (\hat{C}_{12} + \hat{C}_{26} m_j - \hat{C}_{23} k_j n_j) e^{\eta_j z}] e^{-I_1 \xi} d\xi \tag{6b}$$

$$\sigma_{zz}(x, z) = \frac{1}{2\pi} \int_{-\infty}^{\infty} [-I_1^2 \sum_{j=1}^6 A_{ij} (\hat{C}_{13} + \hat{C}_{36} m_j - \hat{C}_{33} k_j n_j) e^{\eta_j z}] e^{-I_1 \xi} d\xi \tag{6c}$$

$$\tau_{xz}(x, z) = \frac{1}{2\pi} \int_{-\infty}^{\infty} [I_1 \sum_{j=1}^6 A_{ij} (\hat{C}_{44} m_j n_j + \hat{C}_{45} (k_j + n_j)) e^{\eta_j z}] e^{-I_1 \xi} d\xi \tag{6d}$$

$$\tau_{yz}(x, z) = \frac{1}{2\pi} \int_{-\infty}^{\infty} [I_1 \sum_{j=1}^6 A_{ij} (\hat{C}_{45} m_j n_j + \hat{C}_{55} (k_j + n_j)) e^{\eta_j z}] e^{-I_1 \xi} d\xi \tag{6e}$$

$$\tau_{zx}(x, z) = \frac{1}{2\pi} \int_{-\infty}^{\infty} [-I_1^2 \sum_{j=1}^6 A_{ij} (\hat{C}_{16} + \hat{C}_{66} m_j - \hat{C}_{63} k_j n_j) e^{\eta_j z}] e^{-I_1 \xi} d\xi \tag{6f}$$

The displacements and stresses for the isotropic substrate can be written as (Yilmaz et al., 2019),

$$u_2(x, z) = \frac{1}{2\pi} \int_{-\infty}^{\infty} [(A_{21} + A_{22} z) e^{I_2 \xi}] e^{-I_2 z} d\xi \tag{7a}$$

$$v_2(x, z) = \frac{1}{2\pi} \int_{-\infty}^{\infty} [A_{23} e^{I_2 \xi}] e^{-I_2 z} d\xi \tag{7b}$$

$$w_2(x, y) = \frac{1}{2\pi} \int_{-\infty}^{\infty} \left[ \text{Sign}(\xi) \left[ A_{21} + \left( \frac{\kappa_2}{|\xi|} + z \right) A_{22} \right] e^{I_2 \xi} \right] e^{-I_2 z} d\xi \tag{7c}$$

$$\sigma_{xx2}(x, y) = \frac{1}{\pi} \int_{-\infty}^{\infty} \mu_2 \left[ -\xi A_{21} + \left( -\xi z + \text{Sign}(\xi) \frac{\kappa_2 - 3}{2} \right) A_{22} \right] e^{I_2 \xi} e^{-I_2 z} d\xi \tag{7d}$$

$$\sigma_{yy2}(x, y) = \frac{1}{2\pi} \int_{-\infty}^{\infty} \mu_2 \text{Sign}(\xi) A_{22} (-3 + \kappa_2) e^{I_2 \xi} e^{-I_2 z} d\xi \tag{7e}$$

$$\sigma_{zz2}(x, y) = \frac{1}{\pi} \int_{-\infty}^{\infty} \mu_2 \left[ \xi A_{21} + \left( \xi z - \text{Sign}(\xi) \frac{\kappa_2 + 1}{2} \right) A_{22} \right] e^{I_2 \xi} e^{-I_2 z} d\xi \tag{7f}$$

$$\tau_{xz2}(x, y) = \frac{1}{2\pi} \int_{-\infty}^{\infty} \mu_2 I_2 A_{23} e^{I_2 \xi} e^{-I_2 z} d\xi \tag{7g}$$

$$\tau_{yz2}(x, y) = \frac{1}{\pi} \int_{-\infty}^{\infty} \mu_2 \left[ A_{21} |\xi| + \left( |\xi| z - \frac{\kappa_2 - 1}{2} \right) A_{22} \right] e^{I_2 \xi} e^{-I_2 z} d\xi \tag{7h}$$

$$\tau_{zx2}(x, y) = -\frac{1}{2\pi} \int_{-\infty}^{\infty} \mu_2 I_2 A_{23} e^{I_2 \xi} e^{-I_2 z} d\xi \tag{7i}$$

where  $\mu_2$ ,  $E_2$ , and  $\nu_2$  are the stiffness constants of the isotropic substrate. Kolosov's constant  $\kappa_2 = 3 - 4\nu_2$  is used to describe the plane strain conditions.

### 3. The boundary conditions and the singular integral equation

The unknown coefficients  $A_{1j}$  ( $j = 1, 2, \dots, 6$ ) and  $A_{2l}$  ( $l = 1, 2, 3$ ) shown in Eqs. (5) and (7) can be obtained using the following boundary conditions (BCs):

$$\sigma_{xx1}(x, 0) = \begin{cases} -p(x) & -a < x < b \\ 0 & x \leq a, x \geq b \end{cases} \tag{8a}$$

$$\tau_{xz1}(x, 0) = \begin{cases} q(x) = -\eta p(x) & -a < x < b \\ 0 & x \leq a, x \geq b \end{cases} \tag{8b}$$

$$\tau_{yz1}(x, 0) = 0 \tag{8c}$$

$$u_1(x, -h) = u_2(x, -h) \tag{8d}$$

$$v_1(x, -h) = v_2(x, -h) \tag{8e}$$

$$w_1(x, -h) = w_2(x, -h) \tag{8f}$$

$$\sigma_{xx1}(x, -h) = \sigma_{xx2}(x, -h) \tag{8g}$$

$$\tau_{xz1}(x, -h) = \tau_{xz2}(x, -h) \tag{8h}$$

$$\tau_{yz1}(x, -h) = \tau_{yz2}(x, -h) \tag{8i}$$

where  $p(x)$  is the surface contact stress and  $\eta$  is the coefficient of friction. The coefficients  $A_{1j}$  and  $A_{2l}$  can be obtained from the BCs given in Eq. (8):

$$A_{1j} = \int_{-\infty}^b p(\lambda) e^{I_1 \lambda} (A_{1j}^p + \eta A_{1j}^q) d\lambda \quad j = 1, 2, \dots, 6 \tag{9a}$$

$$A_{2l} = \int_{-\infty}^b p(\lambda) e^{I_2 \lambda} (A_{2l}^p + \eta A_{2l}^q) d\lambda \quad l = 1, 2, 3 \tag{9b}$$

For  $q(x) = 0$ ,  $A_{1j}^p$  and  $A_{1j}^q$  take place and for  $p(x) = 0$ ,  $A_{2l}^p$  and  $A_{2l}^q$  take place. Note that, the expressions for  $A_{1j}^p$ ,  $A_{1j}^q$ ,  $A_{2l}^p$ , and  $A_{2l}^q$  are quite long, therefore they are not presented here. Furthermore, as the punch profile is rigid, the deformed shape of the monoclinic coating on the contact area should be identical to the punch profile. Therefore,

$$w_1(x, 0) = -\delta + f(x) \tag{10a}$$

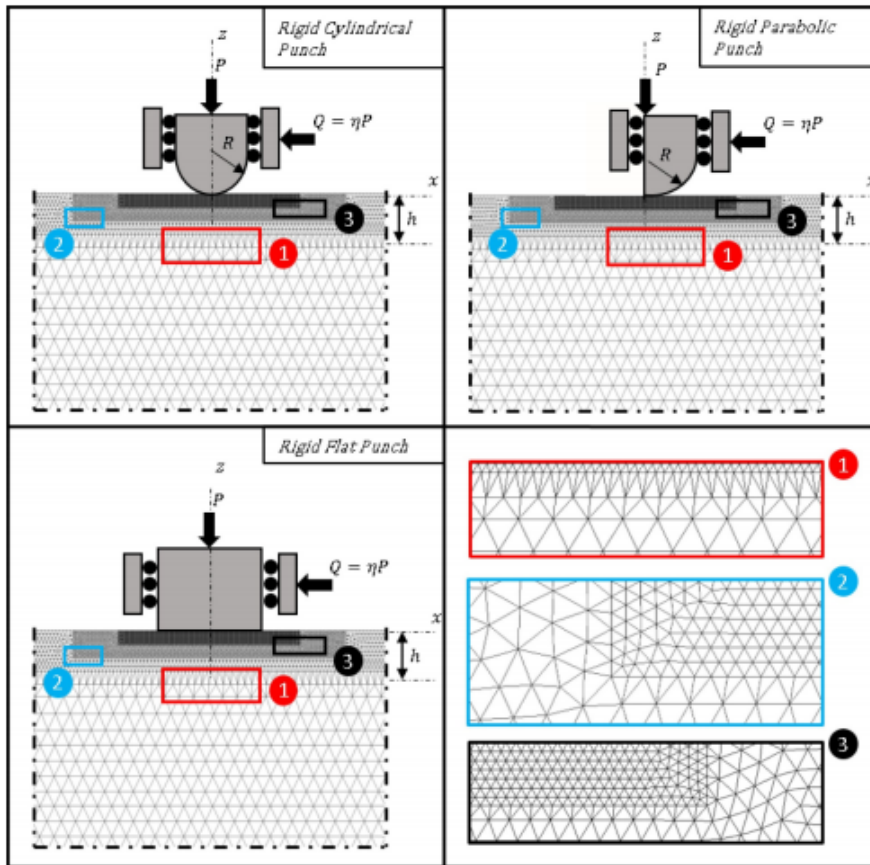


Fig. 2. Finite element model of the sliding frictional contact problem for the monoclinic coating/isotropic substrate system.

$$\frac{\partial w_3(x, 0)}{\partial x} = f'(x) \tag{10b}$$

where  $\delta$  is the indentation depth and  $f(x)$  is the punch profile function. Substituting the unknowns given in Eq. (9) into Eq. (10) yields the following SIE:

$$\eta \frac{\varphi_2}{\varphi_1} p(x) + \frac{1}{\pi} \int_{-a}^b p(\lambda) d\lambda \left[ \frac{1}{\lambda - x} + K_1(x, \lambda) + \eta K_2(x, \lambda) \right] = \frac{C_{66}}{\varphi_1} f'(x), \tag{11}$$

$(-a < x < b)$

where

$$K_1(x, \lambda) = \frac{1}{\varphi_1} \int_0^\infty (M_1(\xi) - \varphi_1) \sin \xi(\lambda - x) d\xi \tag{12a}$$

$$K_2(x, \lambda) = \frac{1}{\varphi_1} \int_0^\infty (M_2(\xi) - \varphi_2) \cos \xi(\lambda - x) d\xi \tag{12b}$$

$$M_1(\xi) = \xi^2 \sum_{j=1}^6 A_j^0 k_j \tag{12c}$$

$$M_2(\xi) = \xi \sum_{j=1}^6 A_j^1 k_j \tag{12d}$$

$$\varphi_1 = \lim_{\xi \rightarrow \infty} M_1(\xi) \tag{12e}$$

$$\varphi_2 = \lim_{\xi \rightarrow \infty} M_2(\xi) \tag{12f}$$

Note that, the following equilibrium equation should be satisfied for the contact problem under consideration

$$\int_{-a}^b p(\lambda) d\lambda = P \tag{13}$$

After introducing the following normalization conditions,

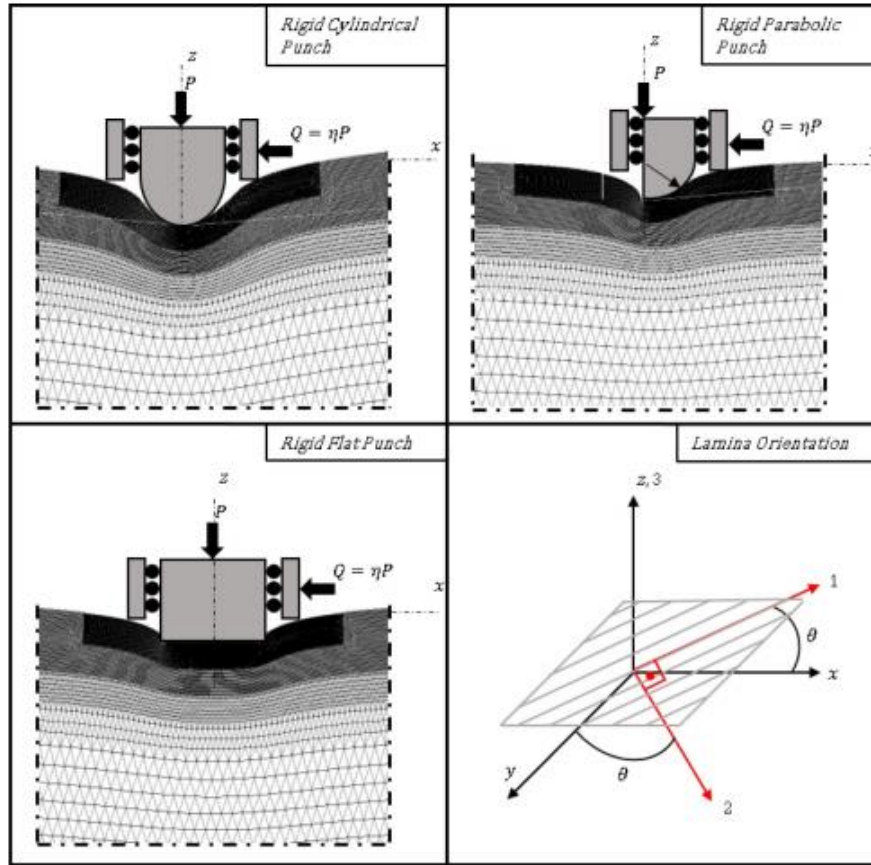


Fig. 3. Deformed geometry of the sliding frictional contact problem for the monoclinic coating/isotropic substrate system.

$$\omega = (\lambda - \frac{b-a}{2}) / (\frac{a+b}{2}), \quad x = (s - \frac{b-a}{2}) / (\frac{a+b}{2}), \quad (14)$$

the SIE in Eq. (11) and the equilibrium condition in Eq. (13) become,

$$\eta \frac{\varphi_2}{\varphi_1} p(x) + \frac{1}{\pi} \int_{-1}^1 p(\omega) d\omega \left[ \frac{1}{\omega - s} + K_1^*(s, \omega) + \eta K_2^*(s, \omega) \right] = \frac{1}{\varphi_1} f'(x) \quad (15a)$$

$$\int_{-1}^1 p(\omega) d\omega = \frac{2P}{a+b} \quad (15b)$$

where

$$K_1^*(s, \omega) = \frac{a+b}{2} K_1(x, \lambda), \quad K_2^*(s, \omega) = \frac{a+b}{2} K_2(x, \lambda) \quad (16)$$

#### 4. Solution of the singular integral equations

The fundamental solution of the SIE shown in Eq. (15a) can be

defined as follows:

$$p(\omega) = g(\omega)(1 - \omega)^\alpha(1 + \omega)^\beta \quad (17)$$

where

$$\alpha = \frac{1}{2\pi I} \text{Log} \left[ \frac{\eta \varphi_2 / \varphi_1 - I}{\eta \varphi_2 / \varphi_1 + I} \right] + N_0 \quad (18a)$$

$$\beta = -\frac{1}{2\pi I} \text{Log} \left[ \frac{\eta \varphi_2 / \varphi_1 - I}{\eta \varphi_2 / \varphi_1 + I} \right] + M_0 \quad (18b)$$

$N_0$  and  $M_0$  in Eq. (18) are arbitrary integers and must be established using,  $-1 < \text{Re}[\alpha, \beta] < 1$ . The SIE can be solved depending on its index  $\chi = -(\alpha + \beta)$ , where  $\chi$  can be  $\pm 1$  or 0. Applying the Gauss-Jacobi formulation presented in Erdogan (1978), the SIE in Eq. (15a) can be converted to the following form:

$$\sum_{i=1}^N W_i^\chi g(\tau_i) \left[ \frac{1}{\omega_i - s_k} + K_1^*(s_k, \omega_i) + \eta K_2^*(s_k, \omega_i) \right] = \frac{1}{\varphi_1} f'(s_k), \quad k = 1, 2, \dots, N - \chi \quad (19)$$

**Table 1**  
Properties of the materials used in this study (Binienda and Pindera, 1994).

Material types for monoclinic coating					
Parameter name	Material name				
	A (Ge/Ep P75/934)	B (Ge/Ep T300/934)	C (GL/Ep)	D (Ge/Al)	E (B/Al)
$E_{11}$ (GPa)	243.0	144.8	42.7	402.6	227.5
$E_{22}$ (GPa)	7.2	10.3	11.7	24.1	137.9
$E_{33}$ (GPa)	7.2	10.3	11.7	24.1	137.9
$\mu_{xy}$ (GPa)	3.9	5.5	8.2	16.8	55.1
$\mu_{yz}$ (GPa)	3.9	5.5	8.2	16.8	55.1
$\mu_{zx}$ (GPa)	2.4	3.4	3.8	8.3	49.2
$\nu_{xy}$	0.33	0.30	0.27	0.29	0.24
$\nu_{yz}$	0.33	0.30	0.27	0.29	0.24
$\nu_{zx}$	0.49	0.50	0.55	0.45	0.40
Material properties for isotropic substrate					
$E_s$ (GPa)	$\mu_s$ (GPa)		$\nu_s$		
12.5	5.0		0.25		
25.0	10.0		0.25		
50.0	20.0		0.25		
–	–		0.25		

Similarly, the equilibrium condition shown in Eq. (15b) becomes

$$\sum_{i=1}^N W_i^N g(r_i) = \frac{2P}{\pi(a+b)} \quad (20)$$

where  $r_i$  and  $s_k$  are the roots of related Jacobi polynomials and  $W_i^N$  is a weighting constant.

$$P_N^{(\alpha,\beta)}(r_i) = 0, \quad i = 1, 2, \dots, N \quad (21a)$$

$$P_N^{(\alpha,\beta)}(s_k) = 0, \quad k = 1, 2, \dots, N - \chi \quad (21b)$$

$$W_i^N = \frac{1}{\pi} \frac{(2N + \alpha + \beta) \Gamma(N + \alpha + 1) \Gamma(N + \beta + 1)}{(N + 1)! \Gamma(N + \alpha + \beta + 2)} \frac{2^{(\alpha+\beta)}}{P_N^{(\alpha,\beta)}(r_i) P_{N+1}^{(\alpha,\beta)}(r_i)} \quad (21c)$$

**4.1. Cylindrical punch profile**

By considering Fig. 1, the following relation may be written for the parabolic punch:

$$f(x) = \frac{x^2}{2R}, \quad f'(x) = \frac{x}{R} \quad (22)$$

where  $R$  is the radius of the punch. As there is no contact stress at  $-a$  and  $b$  the index of the SIE is  $-1$  ( $\chi = -1$ ) (Erdogan, 1978). Therefore, Eqs. (19) and (20) become

$$\sum_{i=1}^N W_i^N g(r_i) \left[ \frac{1}{\omega_i - s_k} + K_1^*(s_k, \omega_i) + \eta K_2^*(s_k, \omega_i) \right] = \frac{1}{\varphi_1 R} \left( \frac{a+b}{2} s_k + \frac{b-a}{2} \right), \quad k = 1, 2, \dots, N + 1 \quad (23a)$$

$$\sum_{i=1}^N W_i^N g(r_i) = \frac{2P}{\pi(a+b)} \quad (23b)$$

To determine exact values for  $-a$  and  $b$ , one requires an extra equation, which can be acquired from Eq. (23a):

**4.2. Parabolic punch profile**

By considering Fig. 1, the following relation may be written for the parabolic punch:

$$f(x) = \frac{x^2}{2R}, \quad f'(x) = \frac{x}{R}, \quad x \geq 0 \quad (24)$$

Note that  $a = 0$  for the parabolic punch, and  $\phi_b$  is bounded at the right end of the contact ( $x = +1$ ) and has an integrable singularity at the left end ( $x = -1$ ). Thus, the index of the SIE is 0 ( $\chi = 0$ ). Eqs. (19) and (20) become

$$\sum_{i=1}^N W_i^N g(r_i) \left[ \frac{1}{\omega_i - s_k} + K_1^*(s_k, \omega_i) + \eta K_2^*(s_k, \omega_i) \right] = \frac{1}{\varphi_1 R^2} (s_k + 1), \quad k = 1, 2, \dots, N \quad (25a)$$

$$\sum_{i=1}^N W_i^N g(r_i) = \frac{2P}{\pi b} \quad (25b)$$

Eqs. (25a) and (25b) contain  $N + 1$  unknowns, which are  $g(r_i)$ , and  $b$  can be obtained.

**4.3. Flat punch profile**

By considering Fig. 1, the following relation may be written for the flat punch:

$$f(x) = \text{constant}, \quad f'(x) = 0 \quad (26)$$

The contact boundaries for the flat punch are  $a = b$ . As there are sharp edges at the contact boundaries, the index of the SIE is  $+1$  ( $\chi = 1$ ). Therefore, Eqs. (19) and (20) become

$$\sum_{i=1}^N W_i^N g(r_i) \left[ \frac{1}{\omega_i - s_k} + K_1^*(s_k, \omega_i) + \eta K_2^*(s_k, \omega_i) \right] = 0, \quad k = 1, 2, \dots, N \quad (27a)$$

$$\sum_{i=1}^N W_i^N g(r_i) = \frac{P}{\pi b} \quad (27b)$$

Eqs. (27a) and (27b), contain  $N$  unknowns, which are  $g(r_i)$ .

**5. The in-plane stresses**

The in-plane stresses at the surface of the monoclinic coating are

$$\sigma_{11}(x, 0) = \begin{cases} \varphi_2 p(x) + H(x), & -a < x < b \\ H(x), & x \leq -a, \quad x \geq b \end{cases} \quad (28)$$

where

$$H(x) = \frac{1}{\pi} \int_{-a}^b p(t) \left[ \varphi_3 \frac{\eta}{\lambda - x} + K_3(x, \lambda) + \eta K_4(x, \lambda) \right] d\lambda \quad (29a)$$

$$K_3(x, \lambda) = \int_0^\infty (M_3(\xi) - \varphi_3) \cos \xi (\lambda - x) d\xi \quad (29b)$$

$$K_4(x, t) = \int_0^\infty (M_4(\xi) - \varphi_4) \sin \xi (t - x) d\xi \quad (29c)$$

$$M_3(\xi) = I \left[ -I_\xi^2 \sum_{j=1}^6 A_{ij} (C_{11} + C_{13} m_j - C_{13} k_j n_j) \right] \quad (29d)$$

$$M_4(\xi) = -I_\xi^2 \sum_{j=1}^6 A_{ij} (\tilde{C}_{11} + \tilde{C}_{13} m_j - \tilde{C}_{13} k_j n_j) \quad (29e)$$

$$\phi_3 = \lim_{\xi \rightarrow \infty} M_3(\xi), \quad \phi_4 = \lim_{\xi \rightarrow \infty} M_4(\xi) \quad (29f)$$

**6. Stress intensity factors**

A stress intensity factor (SIF) characterizes the stress state at sharp edges and provides a failure criterion for fracture mechanics. The method for determining the SIFs for parabolic and flat punch profiles is described in the following subsections.



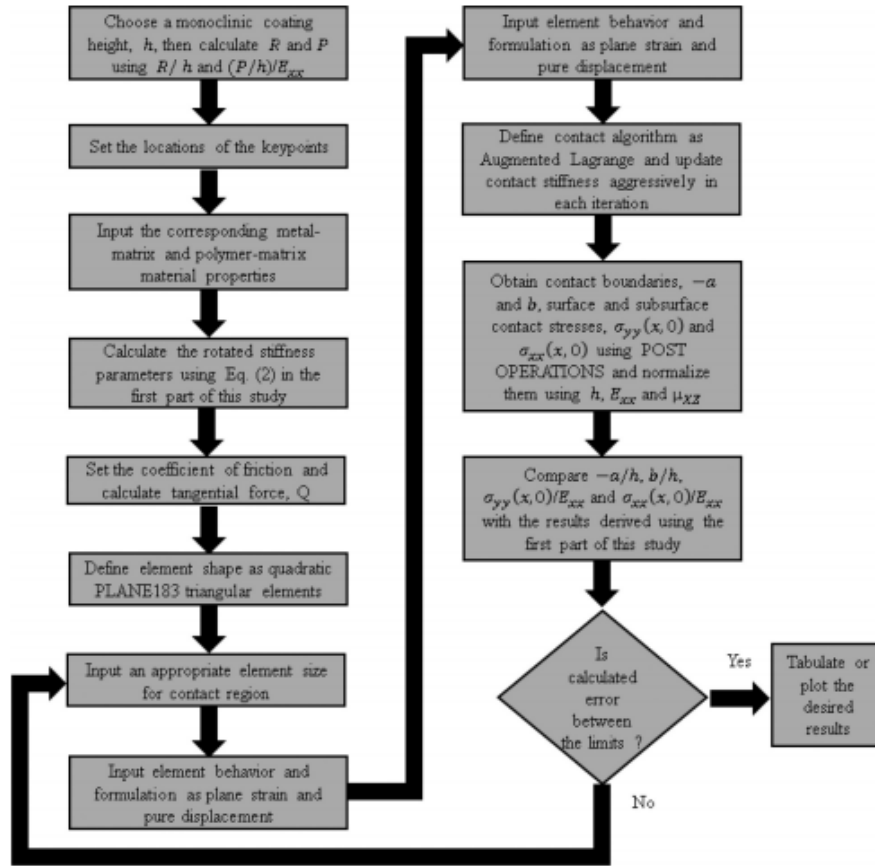


Fig. 4. Flow chart of the iterative scheme.

**Table 2**  
Sensitivity of the developed finite element code (GI/Ep material (Material C) is utilized, rigid cylindrical punch profile is used, where  $E_{xx} = 42.7$  GPa).

$R/h = 100$ ,  $\eta = 0.4$ ,  $\beta = 45^\circ$ ,  $(P/h)/E_{xx} = 0.0024$ ,  $E_2/E_{xx} = 0.585$

# of Elements	# of Nodes	Analytical		FEM		$ r_1 $ (%)	$ r_2 $ (%)
		$-a/h$	$b/h$	$-a/h$	$b/h$		
703	1496	-0.8205	0.8961	-1.1253	1.3867	37.14	54.74
1297	2725	-0.8205	0.8961	-1.0810	1.2400	31.74	38.37
3620	7455	-0.8205	0.8961	-0.9970	1.1520	21.51	28.55
44288	89297	-0.8205	0.8961	-0.9110	0.9654	11.02	7.73
102414	194671	-0.8205	0.8961	-0.8456	0.9220	3.05	2.89
223682	449155	-0.8205	0.8961	-0.8100	0.9000	1.27	0.43
310456	502799	-0.8205	0.8961	-0.8096	0.8984	1.32	0.25

6.1. Parabolic punch profile

$$k(x=0) = \lim_{x \rightarrow 0} \frac{p(x)}{x^2} = b^2 g(x=0) \tag{30}$$

or

$$k(r=-1) = b^2 g(r=-1) \tag{31}$$

6.2. Flat punch profile

$$k(x=-b) = \lim_{x \rightarrow -b} \frac{p(x)}{2^2(b+x)^2} = \frac{b^2}{2^2} g(x=-b) \tag{32a}$$

$$k(x=b) = \lim_{x \rightarrow b} \frac{p(x)}{2^2(b-x)^2} = \frac{b^2}{2^2} g(x=b) \tag{32b}$$

or

$$k(\omega=-1) = \frac{b^2}{2^2} g(\omega=-1) \tag{33a}$$

**Table 3**  
Normalized contact boundaries –  $a/h$  and  $b/h$  for the rigid cylindrical and parabolic punch profiles, where  $E_{zz} = 42.7$  GPa.

$R/h = 100.0, \eta = 0.4, (P/h)/E_{zz} = 0.0024, E_2/E_{zz} = 0.585, \text{Gl/Ep material (Material C)}$									
$\theta$	Cylindrical punch						Parabolic punch		
	Analytical		FEM		$ \epsilon_1 $ (%)		Analytical	FEM	$ \epsilon_1 $ (%)
	$-a/h$	$b/h$	$-a/h$	$b/h$	$-a/h$	$b/h$	$b/h$	$b/h$	$b/h$
$0.0^\circ$	-0.7438	0.8382	-0.7400	0.8520	0.51	1.64	0.9568	0.9600	0.33
$45.0^\circ$	-0.8205	0.8961	-0.8100	0.9000	1.27	0.43	1.0375	1.0120	2.45
$90.0^\circ$	-0.9288	1.0407	-0.9110	1.0140	1.91	2.56	1.2216	1.2440	1.83
$R/h = 100.0, \theta = 30.0^\circ, (P/h)/E_{zz} = 0.0024, E_2/E_{zz} = 0.585, \text{Gl/Ep material (Material C)}$									
$\eta$	Cylindrical punch						Parabolic punch		
	Analytical		FEM		$ \epsilon_1 $ (%)		Analytical	FEM	$ \epsilon_1 $ (%)
	$-a/h$	$b/h$	$-a/h$	$b/h$	$-a/h$	$b/h$	$b/h$	$b/h$	$b/h$
0.0	-0.8231	0.8231	-0.8267	0.8267	0.43	0.43	0.9633	0.9620	0.13
0.4	-0.7822	0.8665	-0.7714	0.8600	1.38	0.75	0.9961	0.9912	0.49
0.8	-0.7440	0.9121	-0.7164	0.9210	2.05	0.97	1.0317	1.0114	1.96
$R/h = 100.0, \eta = 0.4, \theta = 30.0^\circ, E_2/E_{zz} = 0.585, \text{Gl/Ep material (Material C)}$									
$(P/h)/E_{zz}$	Cylindrical punch						Parabolic punch		
	Analytical		FEM		$ \epsilon_1 $ (%)		Analytical	FEM	$ \epsilon_1 $ (%)
	$-a/h$	$b/h$	$-a/h$	$b/h$	$-a/h$	$b/h$	$b/h$	$b/h$	$b/h$
0.0012	-0.5816	0.6220	-0.5560	0.6160	0.99	0.96	0.7127	0.7100	0.37
0.0024	-0.7822	0.8665	-0.7714	0.8600	1.38	0.75	0.9961	0.9912	0.49
0.0048	-1.0825	1.2025	-1.0520	1.2200	2.81	1.45	1.3853	1.3640	1.53
$R/h = 100.0, \eta = 0.4, \theta = 30.0^\circ, (P/h)/E_{zz} = 0.0024, \text{Gl/Ep material (Material C)}$									
$E_2/E_{zz}$	Cylindrical punch						Parabolic punch		
	Analytical		FEM		$ \epsilon_1 $ (%)		Analytical	FEM	$ \epsilon_1 $ (%)
	$-a/h$	$b/h$	$-a/h$	$b/h$	$-a/h$	$b/h$	$b/h$	$b/h$	$b/h$
0.292	-0.8214	0.9430	-0.8060	0.9600	1.87	1.80	1.0576	1.0584	0.07
0.585	-0.7822	0.8665	-0.7640	0.8760	1.38	0.75	0.9961	0.9912	0.49
1.170	-0.7637	0.8227	-0.7360	0.8280	1.00	0.64	0.9617	0.9670	0.55
∞	-0.7472	0.7713	-0.7400	0.7720	0.96	0.69	0.9223	0.9260	0.40
$R/h = 100.0, \eta = 0.4, \theta = 30.0^\circ, (P/h)/E_{zz} = 0.0024, E_2/E_{zz} = 0.585$									
Material	Cylindrical punch						Parabolic punch		
	Analytical		FEM		$ \epsilon_1 $ (%)		Analytical	FEM	$ \epsilon_1 $ (%)
	$-a/h$	$b/h$	$-a/h$	$b/h$	$-a/h$	$b/h$	$b/h$	$b/h$	$b/h$
A	-0.9930	1.0410	-0.9728	1.0496	2.03	0.82	1.2238	1.2210	0.22
B	-0.8613	0.9223	-0.8453	0.9307	1.85	0.91	1.0719	1.0584	1.25
C	-0.7822	0.8665	-0.7714	0.8600	1.38	0.75	0.9961	0.9912	0.49
D	-0.5735	0.6351	-0.5600	0.6480	2.35	2.03	0.7182	0.7014	2.33
E	-0.2671	0.3449	-0.2603	0.3616	2.54	4.84	0.3748	0.3680	1.76

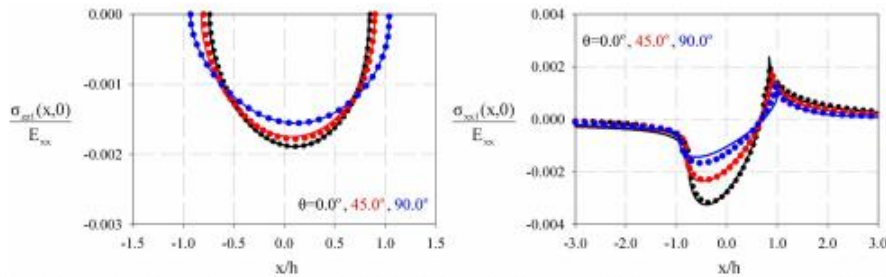


Fig. 5. Effect of lamina orientation angle  $\theta$  on surface stress for  $R/h = 100.0, \eta = 0.4, (P/h)/E_{zz} = 0.0024, E_2/E_{zz} = 0.585, \text{Gl/Ep material (Material C)}$ , and  $E_{zz} = 42.7$  GPa. Solid  $\rightarrow$  Analytical, Dotted  $\rightarrow$  FEM.

$$k(\omega = +1) = \frac{h^\beta}{2^\beta} g(\omega = +1) \tag{33b}$$

$$d_m = \frac{1}{h_m} \pi \sum_{n=1}^N W_n^N P_n^{(\alpha, \beta)}(n) g(n) \tag{35a}$$

where  $g(-1.0)$  and  $g(+1.0)$  can be calculated as follows (Krenk, 1975):

$$g(-1) = \sum_{m=0}^{N-1} d_m P_m^{(\alpha, \beta)}(-1) \tag{34a}$$

$$h_m = 2^{2+\alpha+\beta} \frac{2N+2+\alpha+\beta}{(2m+\alpha+\beta+1)m!} \frac{\Gamma(m+\alpha+1)\Gamma(m+\beta+1)}{\Gamma(m+\alpha+\beta+1)} \tag{35b}$$

$$g(+1) = \sum_{m=0}^{N-1} d_m P_m^{(\alpha, \beta)}(+1) \tag{34b}$$

where

**7. Finite element method**

A computational method is used to compare the analytical results and the results obtained with FEM in order to study the sliding frictional

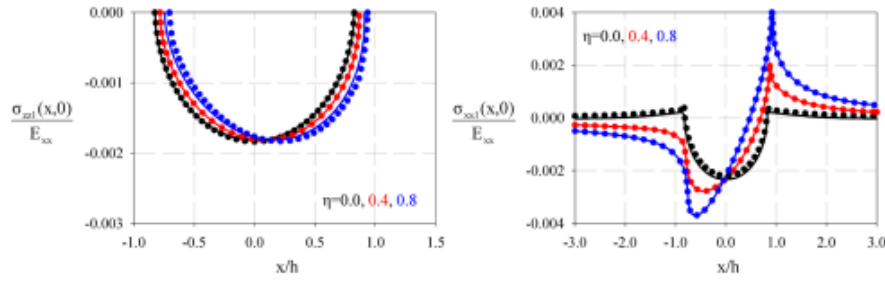


Fig. 6. Effect of coefficient of friction  $\eta$  on the normalized surface stress for  $R/h = 100.0$ ,  $\theta = 30.0^\circ$ ,  $(P/h)/E_{xx} = 0.0024$ ,  $E_2/E_{xx} = 0.585$ , Gl/Ep material (Material C), and  $E_{xx} = 42.7$  GPa. Solid  $\rightarrow$  Analytical, Dotted  $\rightarrow$  FEM.

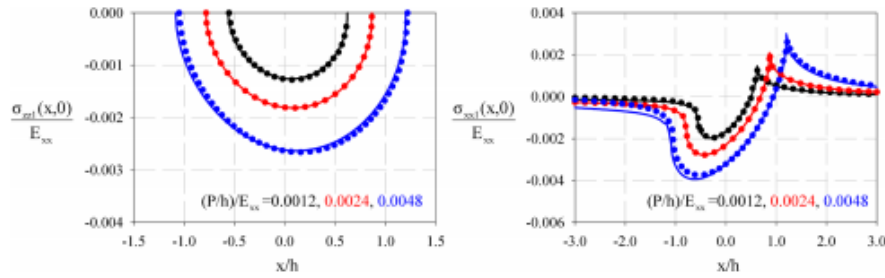


Fig. 7. Effect of dimensionless press force  $(P/h)/E_{xx}$  on the normalized surface stress for  $R/h = 100.0$ ,  $\eta = 0.4$ ,  $\theta = 30.0^\circ$ ,  $E_2/E_{xx} = 0.585$ , Gl/Ep material (Material C), and  $E_{xx} = 42.7$  GPa. Solid  $\rightarrow$  Analytical, Dotted  $\rightarrow$  FEM.

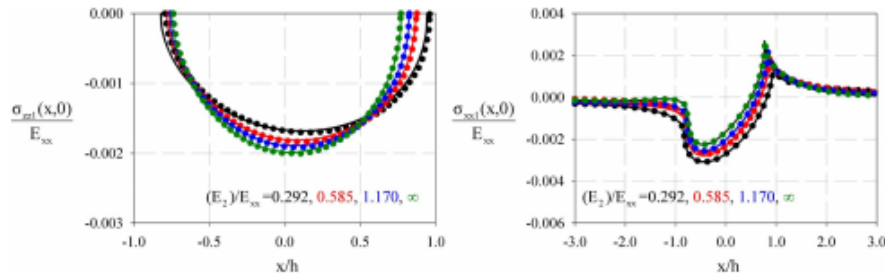


Fig. 8. Effect of dimensionless elastic modulus of the isotropic substrate  $E_2/E_{xx}$  on the normalized surface stress for  $R/h = 100.0$ ,  $\eta = 0.4$ ,  $\theta = 30.0^\circ$ ,  $(P/h)/E_{xx} = 0.0024$ , Gl/Ep material (Material C), and  $E_{xx} = 42.7$  GPa. Solid  $\rightarrow$  Analytical, Dotted  $\rightarrow$  FEM.

contact behavior of a monoclinic coating bonded to an isotropic substrate. Parametric FEM simulations were prepared and solved using ANSYS Parametric Design Language (APDL) 2019. To obviate the unnecessary computing effort, an FE model was prepared in 2-D space using plane strain conditions. The FE model of the considered problem is shown in Fig. 2, wherein three different frictional sliding rigid punch profiles are presented.  $P$ ,  $Q$ ,  $h$  and  $\eta$  represent the applied normal loading, tangential loading, height of the monoclinic coating, and coefficient of friction respectively. To further illustrate the deformation mechanisms in the problem and to aid the readers' understanding, the deformed geometry in the FE model around the contact region is given in Fig. 3.

To simulate the frictional sliding contact condition, TARGE169 target segment elements were utilized to model the different types of rigid punch profiles, as they are quite capable of defining forces and

moments. The contact surface of the monoclinic coating was modeled using CONTA172 contact line elements and the system was meshed using 6-node higher order PLANE183 triangular finite elements. Regardless of the punch profile, 223682 PLANE183 triangular finite elements were utilized in the model while assuming an adaptive mesh size that progressively grows in size out of the contact region. Regarding the punch profile, 1030, 234, and 1210 contact line elements were used for the rigid cylindrical, parabolic, and flat punch profiles, respectively. Calculating the rotated stiffness parameters and imposing them on the developed FE code is very difficult for monoclinic material as this type of material behaves like a rotated lamina over a specified principal axis ( $-z$  axis). Therefore, the complexity in the calculation for the rotated stiffness matrix is primarily due to the calculation of the rotation cosines and stiffness constants in Eq. (2). To define the rotated stiffness matrix, the rotated stiffness parameters were calculated at the

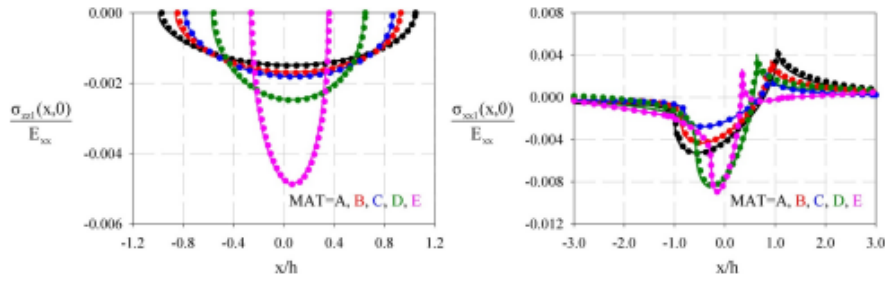


Fig. 9. Effect of coating material type on the normalized surface stress for  $R/h = 100.0$ ,  $\eta = 0.4$ ,  $\theta = 30.0^\circ$ ,  $(P/h)/E_{xx} = 0.0024$ ,  $E_y/E_{xx} = 0.585$ , and  $E_{zz} = 42.7$  GPa. Solid  $\rightarrow$  Analytical, Dotted  $\rightarrow$  FEM.

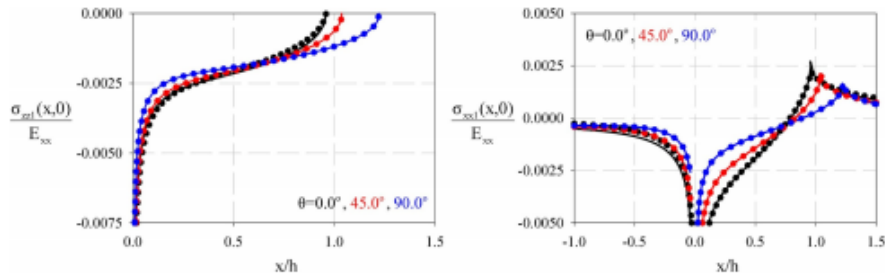


Fig. 10. Effect of lamina orientation angle  $\theta$  on the normalized surface stress for  $R/h = 100.0$ ,  $\eta = 0.4$ ,  $(P/h)/E_{xx} = 0.0024$ ,  $E_y/E_{xx} = 0.585$ , Gl/Ep material (Material C), and  $E_{zz} = 42.7$  GPa. Solid  $\rightarrow$  Analytical, Dotted  $\rightarrow$  FEM.

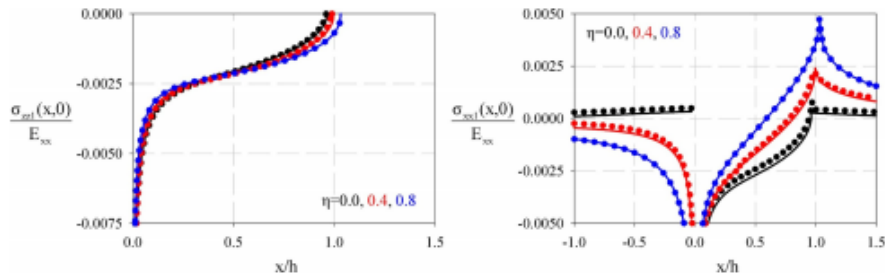


Fig. 11. Effect of coefficient of friction  $\eta$  on the normalized surface stress for  $R/h = 100.0$ ,  $\theta = 30.0^\circ$ ,  $(P/h)/E_{xx} = 0.0024$ ,  $E_y/E_{xx} = 0.585$ , Gl/Ep material (Material C), and  $E_{zz} = 42.7$  GPa. Solid  $\rightarrow$  Analytical, Dotted  $\rightarrow$  FEM.

centroids of each finite element using the material properties presented in Table 1. To improve the numerical efficiency of the developed FE code, only line elements that were in contact were associated with the target segment elements.

8. Pseudo code

In this section, the pseudo code in the considered problem is presented, where an iterative scheme is illustrated in Fig. 4 to further explain the mechanics of the developed FE code. To aid the readers' understanding, additional comments on Fig. 4 are presented below.

- The user can define an arbitrary monoclinic coating height  $h$ .  $R$  and  $P$  also change as  $h$  changes according to  $R/h$  and  $(P/h)/E_{xx}$ .
- Defining an appropriate height for the isotropic substrate in FEM is

crucial. Regarding lower heights, an isotropic substrate may behave like a finite thick substrate rather than a half-plane, which may change the results.

- Choosing a very small element size may reduce the error between the analytical and the FEM results, but it can greatly increase the computational time and reduce the efficiency of the FE code.

9. Calculation of stress intensity factors (SIFs) with FEM

As SIFs characterize the stress state at sharp edges of the punch, appropriately determining them is very important for successfully determining a failure criterion in contact mechanics problems. Data obtained from Eq. (30) was used to calculate the SIFs for a parabolic punch profile with FEM. SIFs are obtained by fitting a line to the data using linear regression and letting  $x$  values tend to zero. The SIFs for the

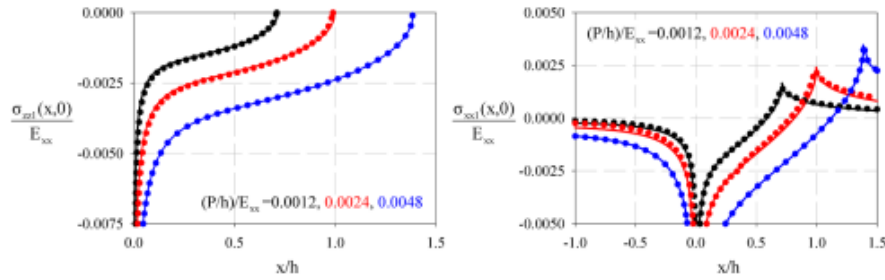


Fig. 12. Effect of dimensionless press force  $(P/h)/E_{xx}$  on the normalized surface stress for  $R/h = 100.0$ ,  $\eta = 0.4$ ,  $\theta = 30.0^\circ$ ,  $E_2/E_{xx} = 0.585$ , Gl/Ep material (Material C), and  $E_{xx} = 42.7$  GPa. Solid  $\rightarrow$  Analytical, Dotted  $\rightarrow$  FEM.

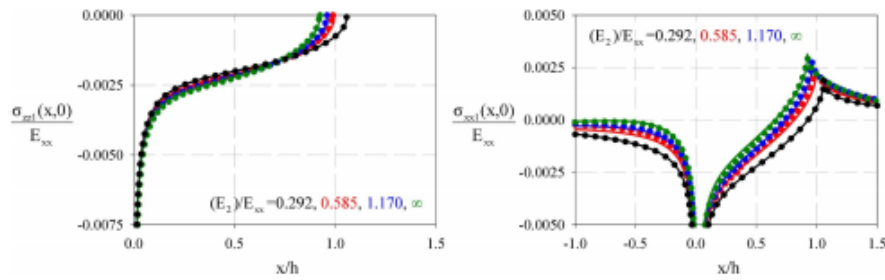


Fig. 13. Effect of dimensionless elastic modulus of the isotropic substrate  $E_2/E_{xx}$  on the normalized surface stress for  $R/h = 100.0$ ,  $\eta = 0.4$ ,  $\theta = 30.0^\circ$ ,  $(P/h)/E_{xx} = 0.0024$ , Gl/Ep material (Material C), and  $E_{xx} = 42.7$  GPa. Solid  $\rightarrow$  Analytical, Dotted  $\rightarrow$  FEM.

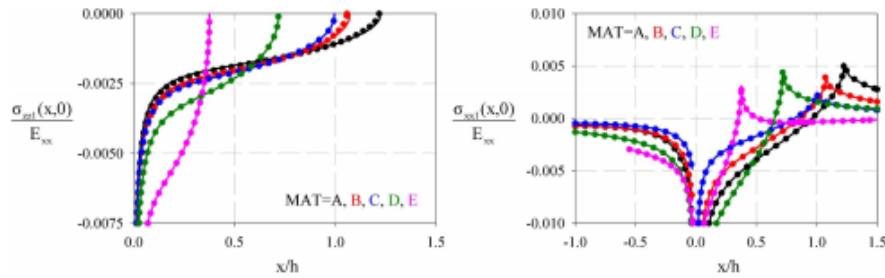


Fig. 14. Effect of coating material type on the normalized surface stress for  $R/h = 100.0$ ,  $\eta = 0.4$ ,  $\theta = 30.0^\circ$ ,  $(P/h)/E_{xx} = 0.0024$ ,  $E_2/E_{xx} = 0.585$ , and  $E_{xx} = 42.7$  GPa. Solid  $\rightarrow$  Analytical, Dotted  $\rightarrow$  FEM.

flat punch profile were calculated using Eq. (32). Again, SIFs are calculated by fitting the data obtained from Eq. (32) to a linear model using linear regression and setting  $x$  equal to  $\pm b$ .

## 10. Results

In this section, the normalized surface contact stress distributions  $\sigma_{xx}(x, 0)/E_{xx}$ , normalized surface in-plane stress distributions  $\sigma_{xx}(x, 0)/E_{xx}$ , normalized contact boundaries  $-a/h$  and  $b/h$ , and SIFs of the analytical formulation are compared with those of FEM for three different rigid punch profiles. The effect of the coating type and lamina orientation on the normalized subsurface in-plane stress contours around the contact region  $\sigma_{xx}(x, y)/\mu_{xx}$  are shown using FEM and are presented in this section. In order to present the results, the following limits are used for the dimensionless geometric and material

parameters:  $0.0^\circ \leq \theta \leq 90.0^\circ$ ,  $0.0 \leq \eta \leq 0.8$ ,  $0.0012 \leq (P/h)/E_{xx} \leq 0.0048$ ,  $0.292 \leq E_2/E_{xx} \leq \infty$ ,  $0.5 \leq a/h \leq 1.0$  and  $R/h = 100$ . for the rigid cylindrical and parabolic punch profiles. Before presenting a comparison of the results for the analytical formulation and FEM, a prior mesh sensitivity analysis of the developed FE code was conducted, and the findings are presented in Table 2.

### 10.1. Effect of geometric and material parameters on stress

Table 3 shows a comparison of the normalized contact boundaries  $-a/h$  and  $b/h$  for the rigid cylindrical and parabolic profiles using the analytical formulation and FEM. Note that, the generated results from the analytical formulation and FEM are consistent, and the maximum true percentage error  $|\epsilon_t|$  (%) between the two methods is 4.84. It is difficult to obtain  $-a/h$  and  $b/h$  without finite element mesh

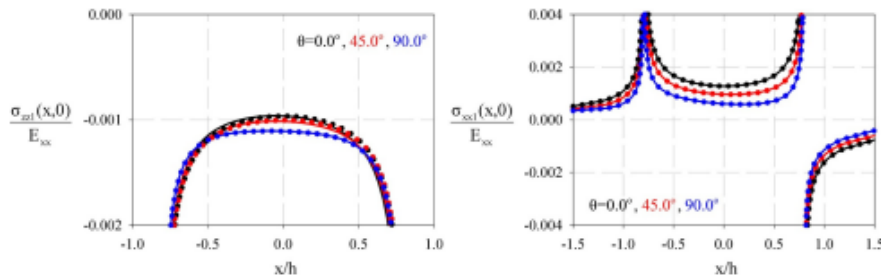


Fig. 15. Effect of lamina orientation angle  $\theta$  on the surface stress for  $a/h = 0.8$ ,  $\eta = 0.4$ ,  $(P/h)/E_{xx} = 0.0024$ ,  $E_2/E_{xx} = 0.585$ , Gl/Ep material (Material C), and  $E_{xx} = 42.7$  GPa. Solid  $\rightarrow$  Analytical, Dotted  $\rightarrow$  FEM.

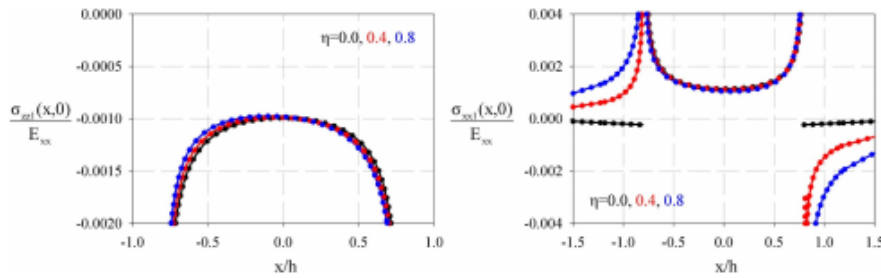


Fig. 16. Effect of coefficient of friction  $\eta$  on the surface stress for  $a/h = 0.8$ ,  $\theta = 30.0^\circ$ ,  $(P/h)/E_{xx} = 0.0024$ ,  $E_2/E_{xx} = 0.585$ , Gl/Ep material (Material C), and  $E_{xx} = 42.7$  GPa. Solid  $\rightarrow$  Analytical, Dotted  $\rightarrow$  FEM.

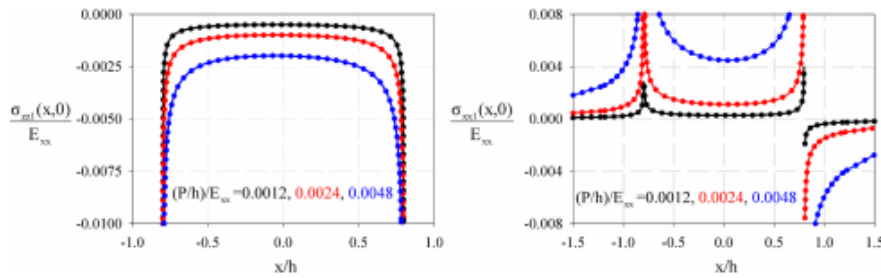


Fig. 17. Effect of dimensionless press force  $(P/h)/E_{xx}$  on the normalized surface stress for  $a/h = 0.8$ ,  $\eta = 0.4$ ,  $\theta = 30.0^\circ$ ,  $E_2/E_{xx} = 0.585$ , Gl/Ep material (Material C), and  $E_{xx} = 42.7$  GPa. Solid  $\rightarrow$  Analytical, Dotted  $\rightarrow$  FEM.

refinement at the contact zone for the metal-matrix material B/Al (Material E) because it has the highest stiffness along the  $-z$  direction, and the punch does not significantly penetrate the surface.

10.1.1. Cylindrical punch profile

The effect of the lamina orientation angle  $\theta$  on the normalized surface stress distribution is shown in Fig. 5, where the polymer-matrix Gl/Ep material (Material C) is used as the monoclinic coating. One can see from the "Lamina Orientation" box in Fig. 3 that increasing  $\theta$  changes the stiffness of the monoclinic coating. As an example, the stiffness along the  $-x$  direction is 42.7 GPa when  $\theta = 0.0^\circ$  and the stiffness is 11.7 GPa when  $\theta = 90.0^\circ$ . As  $\theta$  increases, the absolute peaks for the normalized surface stresses decrease and tensile spikes for the normalized surface in-plane stress at the near boundary  $b/h$  of the contact also decrease because of the reduced total stiffness of the

monoclinic coating. Note that, as the total stiffness decreases, the net surface penetration increases and the resulting stress is distributed more evenly on the contact surface. One can may further conclude that the monoclinic coating behaves like a soft coating as  $\theta$  increases and it behaves like a hard coating as  $\theta$  decreases. Furthermore, the effect of the coefficient of friction  $\eta$  is shown in Fig. 6, where  $R/h = 100.0$ . One should note that  $\eta$  barely affects the normalized surface contact stress distribution as  $P$  is an independent parameter. However,  $Q = \eta P$  depend on  $\eta$ . Therefore,  $\eta$  greatly affects the normalized surface in-plane stress distribution. As  $\eta$  increases, tensile spikes in the normalized surface in-plane stresses greatly increase and the contact shifts to the near boundary  $b/h$ . The effects of the dimensionless press force  $(P/h)/E_{xx}$  and dimensionless elastic modulus of the isotropic substrate  $E_2/E_{xx}$  on the normalized surface stresses are shown in Figs. 7 and 8, respectively. Once again, the polymer-matrix Gl/Ep material (Material C) is

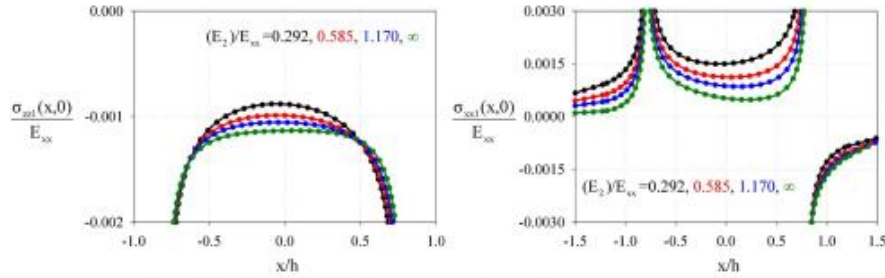


Fig. 18. Effect of dimensionless elastic modulus of the isotropic substrate  $E_2/E_{1z}$  on the normalized surface stress for  $a/h = 0.8$ ,  $\eta = 0.4$ ,  $\beta = 30.0^\circ$ ,  $(P/h)/E_{1z} = 0.0024$ , Gl/Ep material (Material C), and  $E_{1z} = 42.7$  GPa. Solid  $\rightarrow$  Analytical, Dotted  $\rightarrow$  FEM.

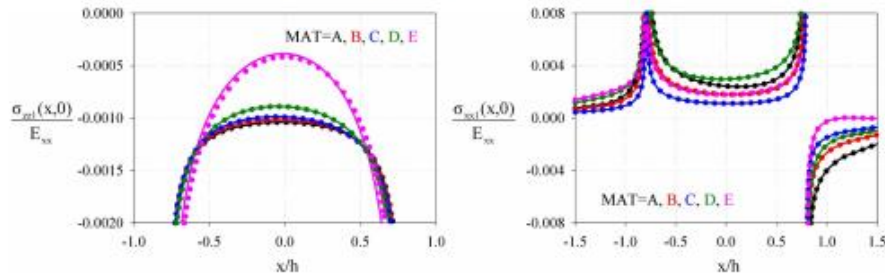


Fig. 19. Effect of coating material type on the normalized surface stress for  $a/h = 0.8$ ,  $\eta = 0.4$ ,  $\beta = 30.0^\circ$ ,  $(P/h)/E_{1z} = 0.0024$ ,  $E_2/E_{1z} = 0.585$ , and  $E_{1z} = 42.7$  GPa. Solid  $\rightarrow$  Analytical, Dotted  $\rightarrow$  FEM.

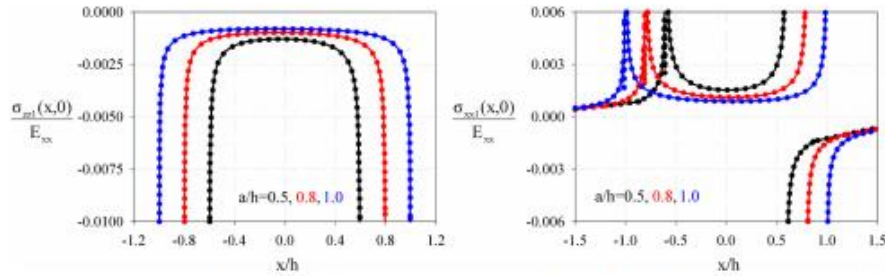


Fig. 20. Effect of dimensionless punch length  $a/h$  on the normalized surface stress for  $\eta = 0.4$ ,  $\beta = 30.0^\circ$ ,  $(P/h)/E_{1z} = 0.0024$ ,  $E_2/E_{1z} = 0.585$ , Gl/Ep material (Material C), and  $E_{1z} = 42.7$  GPa. Solid  $\rightarrow$  Analytical, Dotted  $\rightarrow$  FEM.

used for the monoclinic coating. It is clear that increasing the applied loading causes the rigid cylindrical punch to penetrate deeper into the surface, thus increasing resulting absolute peaks for the normalized surface stresses. Increasing  $(P/h)/E_{1z}$  causes the normalized contact stress distribution to slant to the near boundary of the contact  $b/h$  due to the sliding motion of the punch. Furthermore, increasing  $E_2/E_{1z}$  increases the stiffness of the isotropic substrate, which increases the total rigidity of the system. Therefore, increasing  $E_2/E_{1z}$  produces higher absolute normalized surface stress peaks as the net surface penetration decreases. To investigate the effect of material type, five different polymer-matrix and metal-matrix materials were used for the monoclinic coating and Fig. 9 shows the effect of material type on the normalized surface stresses. As the normalized contact stresses are primarily dependent on the stiffness along the  $-z$  direction, polymer-matrix Gr/Ep P975/934 material (Material A) exhibits the lowest peaks

because the stiffness along that direction is the lowest among all of the materials' (see Table 1). Moreover, the highest absolute peaks were observed for the metal-matrix B/Al material (Material E). However, no correlation between the normalized surface in-plane stresses and stiffness was found along the  $-x$  direction or along the other principle directions.

#### 10.1.2. Parabolic punch profile

The normalized surface stress distributions for the rigid parabolic punch profile are shown in Figs. 10–14. One of the most interesting results that observed is that the tensile spikes in normalized surface in-plane stress distributions have a higher magnitude than those shown in Figs. 5–9 for the cylindrical punch. Due to the singularity at the tip of the punch, the normalized surface in-plane stress approaches infinity at  $x/h = 0.0$ ; thus it is quite difficult to determine the behavior of the

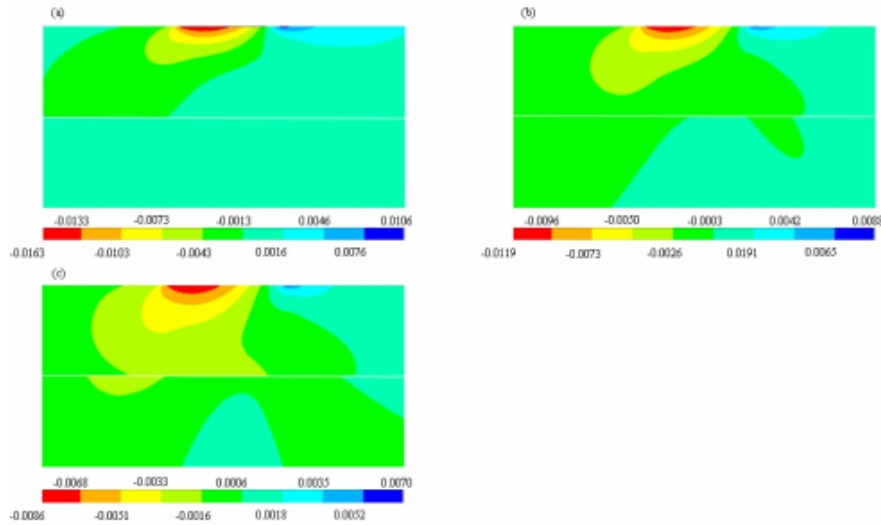


Fig. 21. Effect of lamina orientation angle  $\theta$  on the normalized subsurface in-plane stress for  $\eta = 0.4$ ,  $(P/h)/E_{xx} = 0.0024$ ,  $E_2/E_{xx} = 0.585$ , Gl/Ep material (Material C), and  $\mu_{xx} = 8.238$  GPa (a)  $\theta = 0.0^\circ$ , (b)  $\theta = 45.0^\circ$ , and (c)  $\theta = 90.0^\circ$ .

stress curves for different parameter sets inside this region. However, one can conclude that the findings shown in Figs. 10–14 are quite similar to those shown in the aforementioned paragraph. Furthermore, to prevent the growth of surface cracks during fluctuating or repeated loading, the tensile spikes and stress peaks produced by the parabolic punch profile should be monitored.

### 10.1.3. Flat punch profile

Figs. 15–19 show the normalized surface stress distributions, where the rigid flat punch profile was used. Note that, the shape of the punch defines the contact area, and it appears that stresses become singular at the normalized boundaries of the contact  $-a/h$  and  $b/h$  as the punch profile has sharp edges. The effects of the lamina orientation angle  $\theta$  and coefficient of friction  $\eta$  on the normalized surface contact stresses are quite small, yet one can conclude that some differences can be observed at higher values of these parameters, e.g., when  $\theta = 90.0^\circ$  and  $\eta = 0.8$ . Furthermore, the normalized surface in-plane stresses are greatly affected by the variation in the aforementioned parameters, especially outside the contact area, where variations are fairly significant (see Fig. 15). In addition, the dimensionless press force  $(P/h)/E_{xx}$  and dimensionless elastic modulus of the isotropic substrate  $E_2/E_{xx}$  considerably affect the stresses. As  $(P/h)/E_{xx}$  and  $E_2/E_{xx}$  increase, the absolute peaks in the normalized surface stresses greatly increase (see Figs. 16 and 17). Note that, as  $E_2/E_{xx}$  approaches  $\infty$ , the isotropic substrate behaves like a rigid foundation (see Fig. 18). In contrast to Figs. 9 and 14, as the contact area is known for its flat punch in Fig. 19, only the magnitudes of the stress distributions vary for different types of polymer-matrix and metal-matrix materials. It is quite interesting that, the metal-matrix B/Al material (Material E) has the highest stiffness along the  $-z$  direction but the lowest absolute peak is observed along the same direction in the normalized surface in-plane stresses. Lastly, the effect of dimensionless punch length  $a/h$  is shown in Fig. 20, where three distinct values for  $a/h$  were used. It appears that increasing  $a/h$  slightly reduces the normalized surface stress peaks due to more uniform distribution of stress on the contact surface.

### 10.2. Effects of lamina orientation and coating type on the stresses

Fig. 21 shows the subsurface in-plane stress contours,  $\sigma_{xx}(x, y)$ , which are normalized using  $\mu_{xx}$  for the polymer-matrix Gl/Ep material Material C. The stress in Fig. 21(a), is higher than the stresses observed Fig. 21(b) due to the stiffness along the  $-x$  direction for  $\theta = 0.0^\circ$ . It appears that, for  $\theta = 0.0^\circ$ , the normalized subsurface in-plane stress distribution gathers on the surface of the monoclinic coating due to the shallow penetration of the rigid cylindrical punch. This may initiate growth of surface cracks under repetitive loading conditions and may increase surface wear. However, as  $\theta$  increases, the total stiffness of the system decreases due to the reduction in the stiffness along the  $-x$  direction and the normalized subsurface in-plane stresses distribute more evenly at the subsurface of the system. One can conclude that, using  $\theta = 0.0$  reduces the resulting stresses in the substrate but it also reduces the performance of the coating due to the stress peaks growing at the surface.

To investigate the effect of coating type for different lamina orientations, normalized subsurface in-plane stress contours around the contact region  $\sigma_{xx}(x, y)/\mu_{xx}$  are obtained using FEM in Figs. 22–24. In Fig. 22,  $\theta = 0.0^\circ$  and the rigid cylindrical punch profile is utilized. It is easy to see from Fig. 22(a)–(c) that, using polymer-matrix materials for the monoclinic coating helps distribute the stress evenly at the subsurface of the system as the stiffness along the  $-x$  direction is lower than the stiffness of the metal-matrix materials. Conversely, using metal-matrix materials causes stress to gather near one point at the surface of the monoclinic coating (see Fig. 22(d) and (e)). In addition, the highest normalized subsurface in-plane stresses are observed in Fig. 22(d) for the metal-matrix Gr/Al material (Material D), and lowest stresses are observed in Fig. 22(c) for the polymer-matrix material Gl/Ep (Material C). Furthermore, as the maximum compressive stresses gather around one point at the surface of the monoclinic coating for the metal-matrix materials, the maximum tensile stresses forms at the interface between the layers. One can conclude that, a monoclinic coating made from polymer-matrix materials behaves like a cushion, while that made from metal-matrix materials behaves like a hard surface.



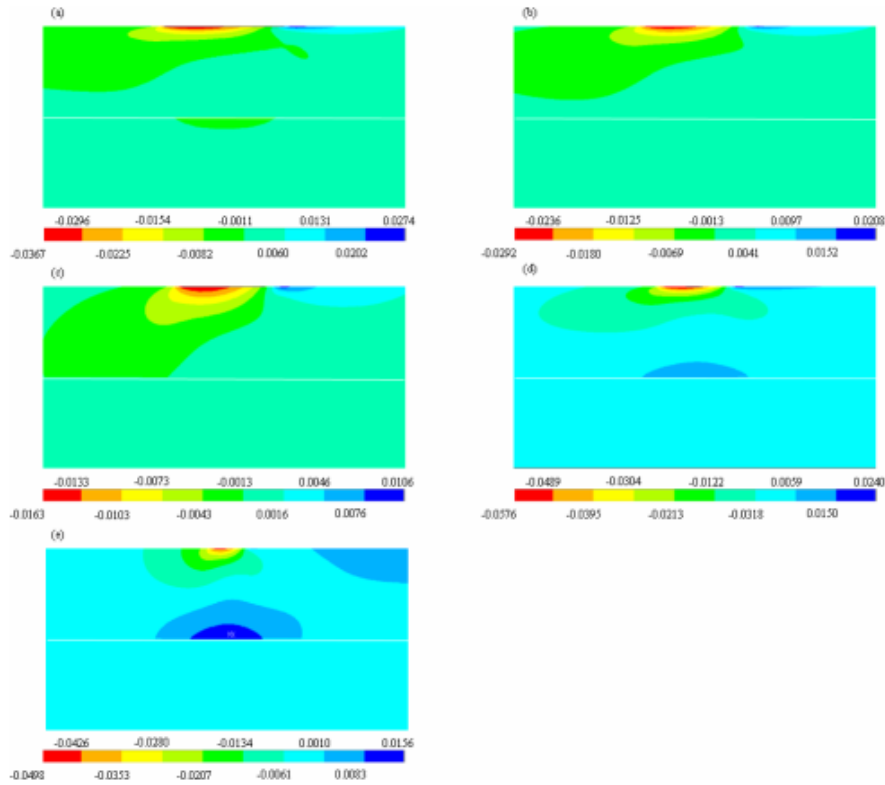


Fig. 22. Effect of coating material type on the normalized subsurface in-plane stress for  $\eta = 0.4$ ,  $\theta = 0.0^\circ$ ,  $(P/h)/E_m = 0.0024$ ,  $E_f/E_m = 0.585$ , and  $\mu_m = 8.238$  GPa (a) Gr/Ep material F75/934 (Material A), (b) Gr/Ep material T300/934 (Material B), (c) Gl/Ep material (Material C), (d) Gr/Al material (Material D), and (e) B/Al material (Material E).

Identical geometric and material parameters were used to generate the contours shown in Figs. 23 and 24, except  $\theta$  was fixed at  $45.0^\circ$  and  $90.0^\circ$ , respectively. Changing the lamina orientation angle from  $0.0^\circ$  to  $45.0^\circ$  greatly increases the torsional stiffness of the monoclinic coating and the global resistance of the system to shearing loads. However, increasing  $\theta$  decreases the total stiffness of the system. Thus, lower absolute values for the normalized subsurface in-plane stresses  $\sigma_{xx}(x, y)/\mu_m$  were observed (see Fig. 23) as the normalized subsurface in-plane stress is distributed more evenly at the subsurface. Moreover, as  $\theta$  increases from  $45.0^\circ$  to  $90.0^\circ$ , the total stiffness of the system reduces decreases again and  $\sigma_{xx}(x, y)/\mu_m$  distributes at the subsurface of the system much more evenly (see Fig. 24). Furthermore, maximum tensile stresses are observed at the subsurface of the isotropic substrate as  $\theta$  increases.

### 10.3. Comparison of SIFs

A comparison of the analytical and FEM SIF results is shown in Tables 4 and 5 for different values of lamina orientation angle  $\theta$ . It is clear from these tables that there is no correlation between  $\theta$  and the powers of stress singularities  $\alpha$  and  $\beta$ . However, one can see that the resulting SIFs for the parabolic and flat punch profiles decreases as  $\theta$

increases, and this tendency arises as the stiffness of the system along the  $-x$  direction decreases. Finally, Tables 4 and 5, one can observe that increasing  $\theta$  decreases crack initiation on the surface of the monoclinic coating because the SIFs decrease.

## 11. Conclusions

A sliding frictional contact mechanics problem for a monoclinic coating bonded to an isotropic substrate was studied under plane strain conditions. The analytical formulation based on the SIE approach is presented for three different cases of the index of the problem, where  $\chi = -1, 0$  and  $1$  corresponds to cylindrical, parabolic, and flat punch profiles, respectively. Highly important benchmark results were obtained from this comprehensive, novel parametric study, which may be useful to the tribology community in designing wear resistant coated surfaces. This study may be further expanded to investigate the contact behavior of different types of polymer-matrix and metal-matrix materials or fiber-reinforced composites to be used in coated surfaces. Important conclusions are outlined below.

- As  $\theta$  increases, the monoclinic coating behaves like a soft coating, while it behaves like a hard coating as  $\theta$  decreases. Regardless of the

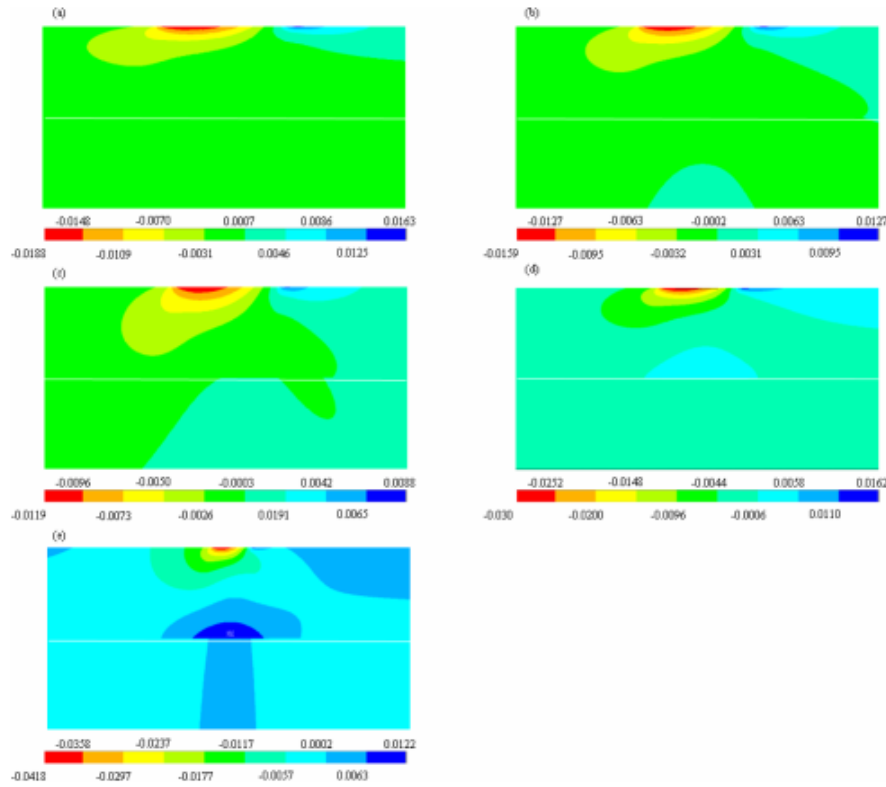


Fig. 23. Effect of coating material type on the normalized subsurface in-plane stress for  $\eta = 0.4$ ,  $\theta = 45^\circ$ ,  $(P/h)/E_{xx} = 0.0024$ ,  $E_y/E_{xx} = 0.585$ , and  $\mu_{zz} = 8.238$  GPa (a) Gr/Ep material P75/934 (Material A), (b) Gr/Ep material T300/934 (Material B), (c) Gl/Ep material (Material C), (d) Gr/Al material (Material D), and (e) B/Al material (Material E).

punch profile, the absolute peaks for  $\sigma_{xx}(x, 0)/E_{xx}$  and tensile spikes for  $\sigma_{xx}(x, 0)/E_{xx}$  decrease for higher values of  $\theta$  as stress evenly distributes on the surface of the monoclinic coating.

- Increasing  $\eta$  slightly affects the  $\sigma_{xx}(x, 0)/E_{xx}$  distributions as  $P$  is an independent parameter. Conversely,  $\eta$  has an immense effect on the  $\sigma_{xx}(x, 0)/E_{xx}$  distribution for rigid cylindrical, parabolic, and flat punch profiles because of the dependency of  $Q = \eta P$  on  $\eta$ . The magnitude of the resulting tensile spikes greatly increases as  $\eta$  increases. It is essential to monitor these tensile spikes to prevent the growth of surface cracks in benchmark stages.
- Regardless of the punch profile, geometric, and material parameters, increasing  $(P/h)/E_{xx}$  increases the net surface pressure, leading to deeper surface penetration and higher absolute peaks for  $\sigma_{xx}(x, 0)/E_{xx}$  and  $\sigma_{xx}(x, 0)/E_{xx}$ .
- Increasing  $E_z/E_{xx}$  increases the stiffness of the isotropic substrate, which increases the total rigidity of the system. Therefore, the net surface penetration decreases and one observes higher absolute peaks in stress distributions. However, it is quite difficult to distinguish the behavior of stress curves for the parabolic punch as the stress distribution approaches infinity at  $x/h = 0.0$ .
- Proper material utilization is crucial in designing coated systems. Therefore, for rigid cylindrical and parabolic punch profiles, one

should use the polymer-matrix Gr/Ep material (Material A) for a monoclinic coating if low absolute peaks are desired, or metal-matrix B/Al (Material E) if shallow surface penetration is desired. Furthermore, similar explanations could not be formulated for a rigid flat punch profile as the metal-matrix B/Al material (Material E) has the highest stiffness along the  $-z$  direction, but the lowest absolute peak was observed for metal-matrix B/Al material (Material E) in the  $\sigma_{xx}(x, 0)/E_{xx}$  distribution.

- It appears that the resulting  $\sigma_{xx}(x, y)$  gathers on the surface of the monoclinic coating for  $\theta = 0^\circ$ , which may increase surface wear or lead to initiation of cracks. As  $\theta$  increases, the monoclinic coating softens and produces an even stress distribution at the subsurface of the system.
- Using polymer-matrix monoclinic coatings helps distribute stress contours equally at the subsurface of the system as the coating stiffness in  $-x$  direction is considerably lower than that for metal-matrix coatings. Conversely, using metal-matrix monoclinic coatings causes stress to concentrate around one point at the surface. One can conclude that, polymer-matrix materials may prevent coating from unnecessary wear and early crack propagation under repetitive loading as seen from the distribution of the stress at the subsurface.
- The relationship between  $\theta$  and the monoclinic material property is

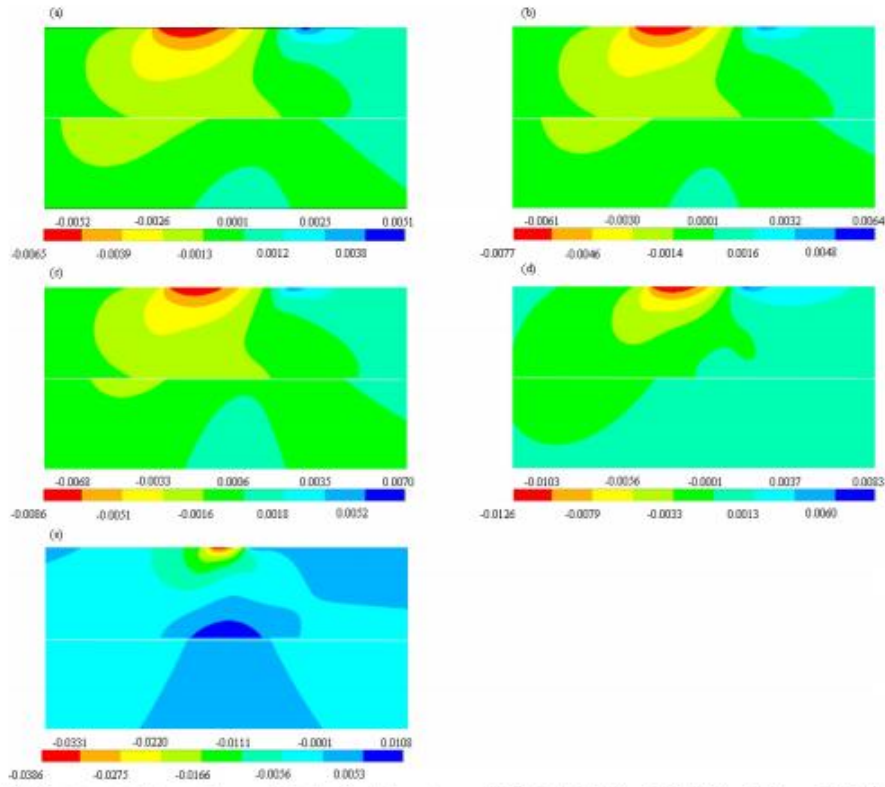


Fig. 24. Effect of coating material type on the normalized subsurface in-plane stress  $\eta = 0.4$ ,  $\theta = 90.0^\circ$ ,  $(P/h)/E_{oz} = 0.0024$ ,  $E_2/E_{oz} = 0.585$ ,  $\mu_z = 8.238$  GPa (a) Gr/Ep material P75/934 (Material A), (b) Gr/Ep material T300/934 (Material B), (c) Gl/Ep material (Material C), (d) Gr/Al material (Material D), and (e) B/Al material (Material E).

Table 4  
SIFs for the parabolic punch,  $SIF \rightarrow k(-1) = b^{\alpha}g(-1)$ , where  $E_{oz} = 42.7$  GPa.

$(P/h)/E_{oz} = 0.0024$ ,  $E_2/E_{oz} = 0.585$

$\eta = 0.4$ , Gl/Ep material (Material C)

$\theta$	$\alpha$	$R/h = 100.0$ SIF(k-1)		$ \epsilon_1 $ (%)
		Analytical	FEM	
0.0	0.4663	43.980	44.110	0.29
30.0	0.4711	42.556	43.850	3.04
45.0	0.4739	41.223	41.780	1.55
60.0	0.4747	39.970	40.160	0.47
90.0	0.4465	37.130	37.950	2.20

intriguing. As  $\theta$  increases from  $0.0^\circ$  to  $90.0^\circ$  the stiffnesses along the  $-x$  and  $-y$  directions start to switch. For instance, assuming that the monoclinic coating is engineered using a polymer-matrix Gr/Ep material (Material A),  $E_{xx} = 243.0$  GPa and  $E_{yy} = 7.2$  GPa for  $\theta = 0.0^\circ$ ,  $E_{xx} = 7.2$  GPa and  $E_{yy} = 243.0$  GPa for  $\theta = 90.0^\circ$ . Therefore, increasing  $\theta$  reduces the overall stiffness of the system and more evenly distributes and reduces stress contours along the subsurface. Additionally, maximum tensile stresses distributes along the subsurface of the isotropic substrate for higher values of lamina orientation angle  $\theta$ .

- No relationship was found between  $\theta$  and the powers of stress singularities  $\alpha$  and  $\beta$ . Nevertheless, one can conclude that the SIF values decrease for the parabolic and flat punch profiles as  $\theta$  increases.

**Table 5**  
SIFs for the flat punch,  $SIF \rightarrow k(-) = a^2g(-)$ , and  $SIF \rightarrow k(+1) = a^2g(+1)$ , where  $E_m = 42.7$  GPa.

( $P/h$ )/ $E_m = 0.0024$ ,  $E_j/E_m = 0.585$ ,  $\gamma = 0.4$ , GI/Ep material (Material C)

$\theta$	$\alpha$	$\beta$	$a/h = b/h = 0.8$				SIF(k+1)	$v_1$   (%)	$v_2$   (%)
			SIF(k-1)	Analytical	SIF(k+1)	SIF(k-1)			
0.0	-0.5337	-0.4663	43.538		41.818	44.810	43.790	2.92	4.71
30.0	-0.5288	-0.4711	42.308		41.049	43.510	42.810	2.84	1.18
45.0	-0.5260	-0.4739	41.295		39.941	42.140	41.250	2.04	3.27
60.0	-0.5253	-0.4747	40.430		38.470	41.730	39.460	3.21	2.57
90.0	-0.5534	-0.4465	39.870		33.080	40.880	34.410	2.28	4.02

**Appendix A. Appendix**

Expression of  $n_j$ ,  $k_j$  and  $m_j$ , ( $j = 1, 2...13$ ) appearing in Eq. (5)

$$n_1 = \sqrt{\frac{(2T_1)^{2/3} - 2T_1^{2/3}L_3 + 2^{4/3}(L_3^2 - 3L_2L_4)}{6T_1^{2/3}L_4}} \tag{36a}$$

$$n_2 = \sqrt{\frac{(2T_2)^{2/3}(-1 - I\sqrt{3}) - 4T_2^{2/3}L_3 + 2^{4/3}(-1 + I\sqrt{3})(L_3^2 - 3L_2L_4)}{12T_2^{2/3}L_4}} \tag{36b}$$

$$n_3 = \sqrt{\frac{(2T_2)^{2/3}(-1 + I\sqrt{3}) - 4T_2^{2/3}L_3 + 2^{4/3}(-1 - I\sqrt{3})(L_3^2 - 3L_2L_4)}{12T_2^{2/3}L_4}} \tag{36c}$$

$$n_4 = -\sqrt{\frac{(2T_1)^{2/3} - 2T_1^{2/3}L_3 + 2^{4/3}(L_3^2 - 3L_2L_4)}{6T_1^{2/3}L_4}} \tag{36d}$$

$$n_5 = -\sqrt{\frac{(2T_2)^{2/3}(-1 - I\sqrt{3}) - 4T_2^{2/3}L_3 + 2^{4/3}(-1 + I\sqrt{3})(L_3^2 - 3L_2L_4)}{12T_2^{2/3}L_4}} \tag{36e}$$

$$n_6 = -\sqrt{\frac{(2T_2)^{2/3}(-1 + I\sqrt{3}) - 4T_2^{2/3}L_3 + 2^{4/3}(-1 - I\sqrt{3})(L_3^2 - 3L_2L_4)}{12T_2^{2/3}L_4}} \tag{36f}$$

$$m_j = \frac{(Z_1^2Z_5 + Z_1(Z_{10}(Z_2 - n_j^2Z_4) - Z_4Z_6) + n_j^2(Z_{10}Z_2Z_3 + Z_4^2Z_7 - Z_2Z_4Z_6) + n_j^4Z_4(-Z_{10}Z_3 + Z_4Z_8))}{Z_{10}Z_2^2 + Z_4(Z_4Z_6 - Z_2Z_8)} \tag{36g}$$

$$k_j = \frac{n_j(Z_{12} + m_j(n_j^2Z_{10} + Z_{13}) + n_j^2Z_6}{Z_{11}} \tag{36h}$$

where

$$L_1 = (\tilde{C}_{36} + \tilde{C}_{45})\tilde{C}_{55}(\tilde{C}_{16}^2 - \tilde{C}_{11}\tilde{C}_{66}) \tag{37a}$$

$$L_2 = -(C_{36} + C_{45})(C_{16}^2C_{33} - 2C_{36}(C_{13}(C_{36} + C_{45}) + C_{36}C_{55}) + C_{13}(C_{13} + 2C_{33})C_{66} + \tilde{C}_{11}((\tilde{C}_{36} + \tilde{C}_{45})^2 - \tilde{C}_{44}\tilde{C}_{55} - \tilde{C}_{33}\tilde{C}_{66})) \tag{37b}$$

$$\dots \tag{37c}$$

$$L_3 = (\tilde{C}_{36} + \tilde{C}_{45})(\tilde{C}_{13}^2\tilde{C}_{44} - 2\tilde{C}_{13}\tilde{C}_{45}(\tilde{C}_{36} + \tilde{C}_{45}) + \tilde{C}_{36}^2\tilde{C}_{55} + 2\tilde{C}_{13}\tilde{C}_{44}\tilde{C}_{55} - \tilde{C}_{33}(\tilde{C}_{11}\tilde{C}_{44} - 2\tilde{C}_{36}\tilde{C}_{45} + \tilde{C}_{55}\tilde{C}_{66})) \tag{37e}$$

$$\dots \tag{37f}$$

$$L_4 = -\tilde{C}_{13}(\tilde{C}_{36} + \tilde{C}_{45})(\tilde{C}_{45}^2 - \tilde{C}_{44}\tilde{C}_{55}) \tag{37h}$$

$$T_1 = -2L_3^3 + 9L_2L_3L_4 - 27L_1L_4^2 + \sqrt{-4(L_2^2 - 3L_2L_4)^3 + (2L_3^3 - 9L_2L_3L_4 + 27L_1L_4^2)^2} \tag{37i}$$

$$T_2 = -2L_3^3 + 9L_2L_3L_4 - 27L_1L_4^2 + 3\sqrt{3}\sqrt{L_2^2(-L_2^2L_3^2 + 4L_1L_3^3 + 4L_4L_2^3 - 18L_1L_2L_3L_4 + 27L_1^2L_4^2)} \tag{37j}$$

**References**

Alinia, Y., Hosseini-nasab, M., Güler, M., 2018. The sliding contact problem for an orthotropic coating bonded to an isotropic substrate. *Eur. J. Mech.* 70, 156–171.  
 Batra, R., Jiang, W., 2008. Analytical solution of the contact problem of a rigid indenter and an anisotropic linear elastic layer. *Int. J. Solids Struct.* 45 (22), 5814–5830.  
 Baumli, P., Al-Azzawi, A., 2015. Methods of composite coating: a review. *Mater. Sci. Eng.* 40, 26–32.  
 Bisienda, W.K., Pindera, M.-J., 1994. Frictionless contact of layered metal-matrix and polymer-matrix composite half planes. *Compos. Sci. Technol.* 50 (1), 119–128.  
 Brezusa, L.C., 2014. Contact stresses: analysis by finite element method (FEM). *Procedia Technology, The 7th International Conference Interdisciplinarity in Engineering (INTER-ENG 2013)*. 12 pp. 401–410.

- Cacerescu, L., Jiménez-Figueroa, E., Pex, T., Anglada, M., 2008. Contact strength of ceramic laminates. *Compos. Sci. Technol.* 68 (1), 209–214.
- Chen, P., Chen, S., Peng, J., 2015. Frictional contact of a rigid punch on an arbitrarily oriented gradient half-plane. *Acta Mech.* 226 (12), 4207–4221.
- Corbett, C.J., Sauer, R.A., 2015. Three-dimensional isogeometrically enriched finite elements for frictional contact and mixed-mode debonding. *Comput. Methods Appl. Mech. Eng.* 284, 781–806.
- Das, S., Güler, M.A., Yildirim, B., Özatag, A.C., 2009. Sliding frictional contact between a rigid punch and a laterally graded elastic medium. *Int. J. Solids Struct.* 46, 4038–4053.
- Diao, D., 1999. Finite element analysis on local yield map and critical maximum contact pressure for yielding in hard coating with an interlayer under sliding contact. *Tribol. Int.* 32 (1), 25–32.
- Erba, B., Yusufoglu, E., Kaplanov, J., 2011. A plane contact problem for an elastic orthotropic strip. *J. Eng. Math.* 70 (4), 399–409.
- Erdogan, F., 1978. *Mixed Boundary Value Problems in Mechanics*. 44 Pergamon Press.
- Farah, P., Popp, A., Wall, W.A., 2015. Segment-based vs. element-based integration for mortar methods in computational contact mechanics. *Comput. Mech.* 55 (1), 209–228.
- Goldsberg, R., Ertas, L., 2016. Contact area and maximum equivalent stress in elastic spherical contact with thin hard coating. *Tribol. Int.* 93, 289–296.
- Guinovart-Sanjuán, D., Riccioni, R., Rodríguez-Ramos, R., Guinovart-Díaz, R., Bravo-Castillero, J., Alfonso-Rodríguez, R., Lebon, F., Dumont, S., Sevostianov, I., Sabina, F.J., 2017. Behavior of laminated shell composite with imperfect contact between the layers. *Compos. Struct.* 176, 539–546.
- Hansen, M.T., 1992. The elastic field for spherical hertzian contact including sliding friction for transverse isotropy. *J. Tribol.* 114 (3), 605.
- He, J., Wang, M., 2016. Ballistic performance of laminated functionally graded composites of tlb2-based ceramic and ti-6al-4v alloy against 14.5 mm heavy machine gun up of impact velocity 990 m/s-1. 2015 4th International Conference on Sustainable Energy and Environmental Engineering.
- Haang, X., Pelegrí, A.A., 2007. Finite element analysis on nanoindentation with friction contact at the film/substrate interface. *Compos. Sci. Technol.* 67 (7), 1311–1319.
- Hwu, C., Fan, C., 1998. Solving the punch problems by analogy with the interface crack problems. *Int. J. Solids Struct.* 35 (30), 3945–3960.
- Keer, L., Mowry, D., 1979. The stress field created by a circular sliding contact on transversely isotropic spheres. *Int. J. Solids Struct.* 15 (1), 33–39.
- Kim, J.-H., Paulino, G., 2002. Isoparametric graded finite elements for nonhomogeneous isotropic and orthotropic materials. *J. Appl. Mech.* 69 (1), 502–514.
- Krenk, S., 1975. On the use of the interpolation polynomial for solutions of singular integral equations. *Quart. Appl. Math.* 33 (3), 479–484.
- Kuo, C.H., Keer, L.M., 1992. Contact stress analysis of a layered transversely isotropic half-space. *J. Tribol.* 114 (2), 253.
- Liu, H., Pan, E., 2018. Indentation of a flat-ended cylinder over a transversely isotropic and layered half-space with imperfect interfaces. *Mech. Mater.* 118, 62–73.
- Mahajan, P., 1998. Contact behavior of an orthotropic laminated beam indented by a rigid cylinder. *Compos. Sci. Technol.* 58 (3), 505–513.
- McDevitt, T., Laursen, T., 2000. A mortar-finite element formulation for frictional contact problems. *Int. J. Numer. Methods Eng.* 48 (1), 1525–1547.
- Mokhtari, M., Schipper, D., Vlietjens, N., Noordermeer, J., 2016. Transversely isotropic viscoelastic materials: contact mechanics and friction. *Tribol. Int.* 97, 116–123.
- Ning, X., Lovell, M., Slaughter, W.S., 2006. Asymptotic solutions for axisymmetric contact of a thin, transversely isotropic elastic layer. *Wear* 260 (7), 693–696.
- Shi, D., Lin, Y., Ovaert, T.C., 2003. Indentation of an orthotropic half-space by a rigid ellipsoidal indenter. *J. Tribol.* 125 (2), 223.
- Srinivas, S., Ravi, A., 1979. Bending, vibration and buckling of simply supported thick orthotropic rectangular plates and laminates. *Int. J. Solids Struct.* 6 (11), 1463–1481.
- Swanson, S.R., 2004. Hertzian contact of orthotropic materials. *Int. J. Solids Struct.* 41 (7), 1945–1958.
- Tar, M., Giner, E., Fammayer, F., Wriggers, P., 2012. 2d contact smooth formulation based on the mortar method. *Comput. Methods Appl. Mech. Eng.* 247–248, 1–14.
- Váradai, K., Néder, Z., Friedrich, K., Flöck, J., 2001. The real contact area between composite and steel surfaces in sliding contact. *Compos. Sci. Technol.* 61 (13), 1853–1862.
- Willis, J., 1966. Hertzian contact of anisotropic bodies. *J. Mech. Phys. Solids* 14 (3), 163–176.
- Yılmaz, K.B., Çiğmez, Güler, M.A., Yildirim, B., 2019. Analytical and finite element solution of the sliding frictional contact problem for a homogeneous orthotropic coating-isotropic substrate system. *ZAMM e201800117*.
- Zhou, Y.-T., Kim, T.-W., 2014. Closed-form solutions for the contact problem of anisotropic materials indented by two collinear punches. *Int. J. Mech. Sci.* 89, 332–343.
- Zhou, Y.-T., Lee, K.Y., 2014. Investigation of frictional sliding contact problems of triangular and cylindrical punches on monoclinic piezoelectric materials. *Mech. Mater.* 69 (1), 237–250.

**APPENDIX 3 – Thesis originality report**

## CURRICULUM VITAE

### Credentials

Name Surname :Korhan Babacan Yilmaz  
Place of Birth :Ankara  
Date of Birth :16/03/1992  
Marital Status :Single  
e – mail Address: :korhanbabacanyilmaz@gmail.com  
korhanb.yilmaz@hacettepe.edu.tr  
Foreign Languages :English (Fluent), German (Intermediate)  
Spanish (Intermediate)

### Education

H. S. :2006 – 2010, Umitkoy Anatolian High School, Ankara  
B. Sc. :2010 – 2014, TOBB University of Economics and  
Technology, Department of Mechanical Engineering,  
Ankara  
M. Sc. :2014 – 2016, Hacettepe University, Department of  
Mechanical Engineering, Ankara  
Ph. D. :2016 – 2021, Hacettepe University, Department of  
Mechanical Engineering, Ankara

### Work Experience

2017 – 2021, Research and Teaching Assistant, Hacettepe University,  
Department of Mechanical Engineering, Ankara

2021 – Mechanical Design Engineer, ASELSAN, Ankara

### Skills and Expertise

- Structural analysis
- Finite element method
- Tribology
- Structural design

- Contact mechanics
- Composite materials

### Projects

- Temas Mekanik ve Optimizasyon Teknikleri Kullanılarak Yeni ve Enerji Etkin Silindirik Makaralı Rulman Tasarımı ve Optimizasyonu, 5180049, TUBITAK 1505 – Ortadogu Rulman Sanayi ve Tic. A. Ş.

### Articles

- Yilmaz, K. B., Sabuncuoglu, B., Yildirim, B., Acta Mechanica, XX (2021) X – X. *under-review*
- Yilmaz, K. B., Sabuncuoglu, B., Yildirim, B., Silberschmidt, V., Journal of Engineered Fibers and Fabrics, 15 (2020) 1 – 9.
- Gortan, M. O., Turkbaz, O. S., Yilmaz, K. B., Yildirim, B., Journal of the Faculty of Engineering and Architecture of Gazi University, 35 (2020) 323 – 335.
- Comez, I., Yilmaz, K. B., ZAMM – Journal of Applied Mathematics and Mechanics, 99 (2019) 201800084.
- Yilmaz, K. B., Comez, I., Guler, M. A., Yildirim, B., Mechanics of Materials, 137 (2019) 103132.
- Yilmaz, K. B., Comez, I., Guler, M. A., Yildirim, B., ZAMM – Journal of Applied Mathematics and Mechanics, 99 (2019) 201800117.
- Yilmaz, K. B., Comez, I., Guler, M. A., Yildirim, B., The Journal of Strain Analysis for Engineering Design, 54 (2019) 254 – 275.
- Comez, I., Yilmaz, K. B., Guler, M. A., Yildirim, B., Archive of Applied Mechanics, 89 (2019) 1403 – 1419.
- Yildirim, B., Yilmaz, K. B., Comez, I., Guler, M. A., Meccanica, 54 (2019) 2183 – 2206.
- Comez, I., Yilmaz, K. B., Guler, M. A., Yildirim, B., Journal of Structural Engineering, Applied Mechanics, 2 (2019) 75 – 87, 2019
- Cakici, U. G., Solmaz, S., Yilmaz, K. B., Yildirim, B., Mühendis ve Makina, 60 (2019) 132 – 146.
- Yilmaz, K. B., Comez, I., Yildirim, B., Guler, M.A., El – Borgi, S., International Journal of Mechanical Sciences, 141 (2018) 127 – 142.



- Guler, M.A., Kucuksucu, A., Yilmaz, K. B., Yildirim, B., International Journal of Mechanical Sciences, 120 (2017) 12 – 29.
- Yilmaz, K. B., Guler, M. A., Yildirim, B., Key Engineering Materials, 774 (2018) 179 – 184.

### Oral and Poster Presentations

- Yilmaz, K. B., Comez, I., Guler, M. A., Yildirim, B., International Civil Engineering and Architecture Conference, 17 – 20 April 2019, Golden Light Publishing, Trabzon, 2019, p. 1013.
- Yilmaz, K. B., Comez, I., Guler, M. A., Yildirim, B., International Civil Engineering and Architecture Conference, 17 – 20 April 2019, Golden Light Publishing, Trabzon, 2019, p. 1022.
- Yilmaz, K. B., Comez, I., Guler, M. A., Yildirim, B., 21. Ulusal Mekanik Kongresi, 02 – 06 September 2019, Ahiler Kalkınma Ajansı, Niğde, 2019, p. 687.
- Dogruer, C. U., Yilmaz, K. B., Yildirim, B., 23rd International Conference on System Theory, Control and Computing, 09 – 11 October 2019, IEEE Publishing, Sinaia, 2019, p. 373.
- Himmetoglu, S., Yilmaz, K. B., Yildirim, B., 22. International Scientific Conference, Transport Means, 03 – 05 October 2018, KTU Publishing, Trakai, 2018, p. 49.
- Yilmaz, K. B., Guler, M. A., Yildirim, B., International Conference on Fracture and Damage Mechanics, 04 – 06 September 2018, Trans Tech Publications, Seville 2018, p.179.

### Conferences

- **October 2019:** 23. International Conference on System Theory, Control and Computing, Sinaia
- **September 2019:** 21. Ulusal Mekanik Kongresi, Niğde
- **April 2019:** International Civil Engineering and Architecture Conference, Trabzon
- **September 2018:** 17. International Conference on Fracture and Damage Mechanics, Seville
- **July 2018:** UMTIK Conference, Eskişehir

- **March 2014:** Energy and Environment Conference, Ankara
- **February 2014:** Solar Energy Panel, Ankara
- **May 2013:** ISO 9001 Quality Management Conference, Ankara
- **March 2011:** 5S – Lean Manufacturing Conference, Ankara
- **February 2011:** 6 Sigma Conference, Ankara

